USAFA-TR-79-1
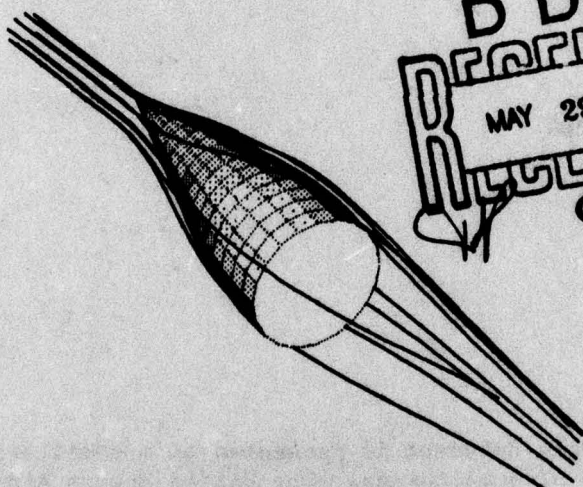
AD A069044

AIR FORCE ACADEMY

AERONAUTICS DIGEST - FALL 1978

FEBRUARY 1979

FINAL REPORT

APPROVED FOR PUBLIC RELEASE: DISTRIBUTION UNLIMITED

DEPARTMENT OF AERONAUTICS

DEAN OF THE FACULTY

UNITED STATES AIR FORCE ACADEMY
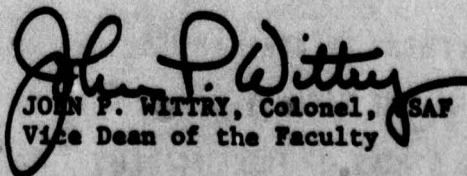
COLORADO 80840

79 05 23 015

COVER:
The figure on the cover is a computer generated plot of the flow
around a 30° included-angle conical probe with the probe at a 7°
angle of attack and a 7° side-slip angle. The plot was generated
on a DEC 11/70 computer and Versatec 1200 dot matrix printer/
plotter. The plotting algorithm was developed by Jeff Clendenon,
a research assistant at Purdue University and the Indianapolis
Center for Advanced Research.

This document is presented as a compilation of monographs
worthy of publication. The United States Air Force Academy
vouches for the quality of research, without necessarily endors-
ing the opinions and conclusions of the authors.

This digest has been cleared for open publication and/or
public release by the appropriate Office of Information in
accordance with AFR 190-17 and DODD 5230.9. There is no objec-
tion to unlimited distribution of this digest to the public at
large, or by DDC to the National Technical Information Service.

This digest has been reviewed and is approved for publica-
tion.

JOHN P. WITTRY, Colonel, USAF
Vice Dean of the Faculty

REPORT DOCUMENTATION PAGE		READ INSTRUCTIONS BEFORE COMPLETING FORM
1. REPORT NUMBER USAFA-TR-79-1	2. GOVT ACCESSION NO.	3. RECIPIENT'S CATALOG NUMBER
4. TITLE (and Subtitle) Air Force Academy Aeronautics Digest, Fall 1978		5. TYPE OF REPORT & PERIOD COVERED Final Report 6. PERFORMING ORG. REPORT NUMBER
7. AUTHOR(s)		8. CONTRACT OR GRANT NUMBER(s) 157 p.
9. PERFORMING ORGANIZATION NAME AND ADDRESS Department of Aeronautics United States Air Force Academy, CO 80840		10. PROGRAM ELEMENT, PROJECT, TASK AREA & WORK UNIT NUMBERS
11. CONTROLLING OFFICE NAME AND ADDRESS 011 550		12. REPORT DATE February 1979 13. NUMBER OF PAGES 152
14. MONITORING AGENCY NAME & ADDRESS(if different from Controlling Office)		15. SECURITY CLASS. (of this report)
		15a. DECLASSIFICATION/DOWNGRADING SCHEDULE

16. DISTRIBUTION STATEMENT (of this Report)

Approved for Public Release; Distribution Unlimited

17. DISTRIBUTION STATEMENT (of the abstract entered in Block 20, if different from Report)

E. J. /Jumper, M. M. /Tower
John P. /Eaton

18. SUPPLEMENTARY NOTES

19. KEY WORDS (Continue on reverse side if necessary and identify by block number)

Aerodynamics, Fluid Mechanics, Thermodynamics, Education, Wind Tunnel

20. ABSTRACT (Continue on reverse side if necessary and identify by block number)

This digest covers unclassified research in aeronautics performed at the United States Air Force Academy during the six months ending 1 January 1979. This report includes individual technical papers in the specific areas of aerodynamics, fluid mechanics, experimental instrumentation, engineering education and thermodynamics and heat transfer.

011 550

79 05 23 015

PREFACE

This report is the second issue of the Air Force Academy Aeronautics Digest. The

first issue, Spring 1978, can be ordered from the Defense Documentation Center (DDC)

using the AD Number: ADA060207. The DDC address is Cameron Station, Alexandria, VA 22314.

Contributions for this digest represent recent scholarly work by students and faculty

of the Department of Aeronautics, members of other departments of the Academy and

The F. J. Seiler Research Laboratory, researchers directly or indirectly involved with

USAFA-sponsored projects and authors in fields of interest to the USAFA. In addition

to complete papers, the Digest also includes, when appropriate, abstracts of lengthier

reports and articles published in other formats. The editors will consider for publi-

cation contributions in the general field of Aeronautics, including:

-Aeronautical Engineering
--Flight Mechanics
--Propulsion
--Structures
-Fluid Mechanics
-Thermodynamics and Heat Transfer
-Engineering Education

Papers on other topics will be considered on an individual basis. Contributions should

be sent to:

Editor, Aeronautics Digest
DFAN
US Air Force Academy, CO 80840

The Aeronautics Digest is presently edited by Capt E. J. Jumper, PhD, and Capt M. M.

Tower, PhD, with the cooperation of the Department of English. In particular, the Digest

would like to thank Maj J. P. Eaton who served as liaison officer from DFENG, gave many

helpful suggestions and provided the final editorial review.

CONTENTS

SECTION I

AERODYNAMICS

A SMOKE TUNNEL INVESTIGATION OF DYNAMIC SEPARATION

Arthur C. Deekens[*] and
William R. Kuebler Jr.[*]

Abstract

An NACA 0015 wing section was tested in a smoke tunnel at the United States Air Force Academy Aeronautics Laboratory. These tests revealed that rotating the wing section through the static stall angle of attack at high rates caused separation to be delayed until an incidence of as much as 48 degrees. Since separation is associated with lift, the aerodynamic performance of a wing could, thus, be momentarily increased. By plotting separation incidence vs. non-dimensionalized constant angular rate, a predictable relationship between these parameters resulted. This report furnishes the analysis and data base for this result.

I. Introduction

Aerodynamicists have continuously studied ways to increase the performance of an airfoil at high angles of attack. Although not completely understood, dynamic stall seems to hold some promise of increasing performance for short periods of time. This stall phenomenon is ultimately connected with a difference in the separation angle of attack between a fixed angle stall (static separation) and the angle of stall when the angle of attack is changing (dynamic separation).

II. Theory

Separation effects can be studied by placing a wing section in a smoke tunnel and observing the changing streamline patterns as this wing section's angle of attack changes. When the airfoil is level, at an angle of attack of zero, the streamlines flow smoothly around the airfoil. As the angle of attack increases, the streamlines constrict along the upper surface indicating that a pressure differential, which gives rise to lift, has occurred. At low angles, the flow remains attached to the wing. At some critical angle of attack, however, the streamlines separate from the upper surface of the wing, giving rise to a region of reverse and turbulent flow. The angle of attack at which separation occurs, α_s , is of interest to the experiment described here.

---

[*]Cadet, USAFA

As previously mentioned, there are two types of separation, static and dynamic, associated with static stall and dynamic stall respectively. The static separation angle of attack is the lowest angle of attack at which the airfoil, when maintained at this angle for an indefinite period of time, will experience separation. This angle is essentially fixed for a fixed airfoil geometry.

The dynamic separation angle of attack, at least as defined for this experiment, is the angle at which the airfoil first experiences separation from some given portion of the upper surface when the airfoil is rotated at a constant angular rate. Unlike the static separation angle, this angle of attack is not constant but is affected by factors such as angular pitching rate, velocity, and airfoil shape.

One measure of the performance of an airfoil can be represented by its lift curve, which shows lift coefficient vs. angle of attack, or C_L vs. α. As shown in Figure 1, the lift coefficient increases up to a certain maximum value and then drops as the stall occurs.
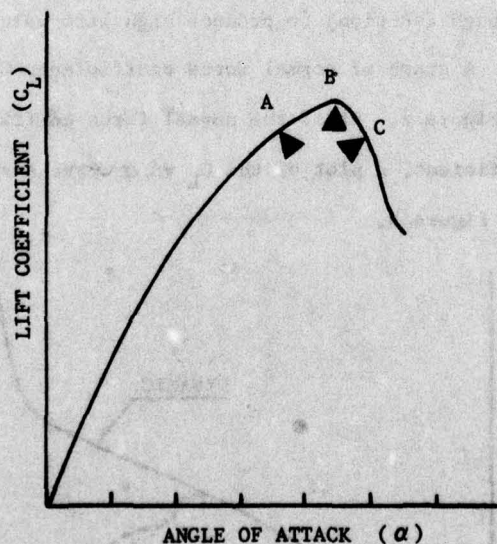

FIGURE 1. Lift Curve for NACA 0015

There is an inherent problem in studying the effects of separation because the flow does not separate at a single point; instead, the flow begins separating from the trailing edge of the wing and progresses forward along the upper surface as angle of attack is increased. Point A in Figure 1 is the approximate angle of attack at which separation begins near the trailing edge. Point B represents the maximum lift angle of attack (the stalling angle) after which the lift coefficient decreases with an increase in α. Point C closely represents separation across the entire wing section.

Research has shown that the $C_{L_{max}}$ for a wing can be increased by exploiting dynamic stall (Ref 1). This has been done by oscillating the airfoil through a range of angles of attack that includes the static stall angle. Although the reasons for the increase in lift are still unclear, aerodynamicists have developed several theories that account for the increased performance. They claim that no observable change occurs in the lift curve slope as the wing section initially rotates past the static stall angle of attack. The lift curve simply extends to higher angles of attack. If conditions are correct, at a certain angle of attack a separation bubble, followed by a strong vortex, appears near the leading edge. As this vortex moves rearward it alters the upper surface pressure distribution enough (suction) to produce high lift values and a rapid nose-down pitching moment (Ref 1). A graph of normal force coefficient, C_N, vs. α taken from Reference 1 is shown in Figure 2. Since the normal force coefficient corresponds roughly to the lift coefficient, a plot of the C_L vs. α curve associated with dynamic stall might appear as in Figure 3.
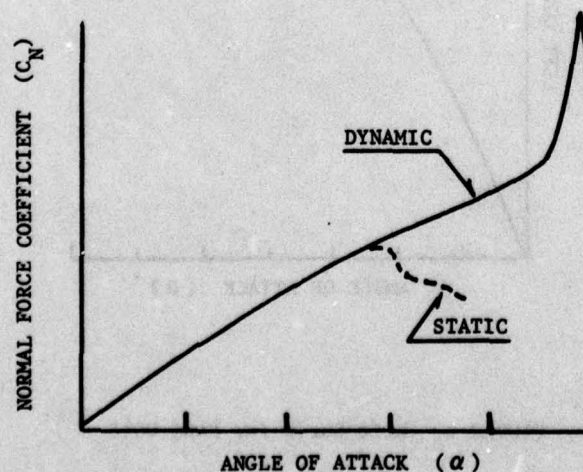
FIGURE 2. Normal Force Coefficient vs. Angle of Attack
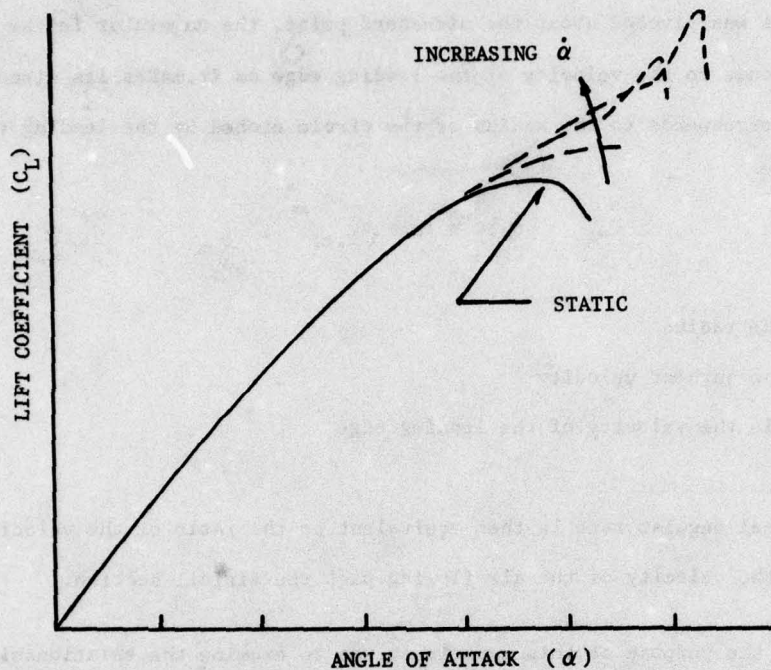
FIGURE 3. Effect of Sinusoidal Oscillation on C_L

Notice that $C_{L_{max}}$ increases with an increase in the sinusoidal variation in angular rate. The shape of the C_L vs. α curve effectively changes from the normal static stall shape. Since the maximum lift coefficient is roughly proportional to the separation angle of attack, this experiment involved analyzing the changes in separation angle of attack. It has been speculated that the dynamic stall can best be studied by using a fixed angular rate instead of a sinusoidal variation in angular rate.

To study the results of various fixed angular rates, one can plot a graph of the *separation angle of attack* vs. the angular rotation rate of the airfoil section. The angular rate was non-dimensionalized using Eqn (1) in an attempt to collapse data.

$$\alpha_{n.d.} = \frac{\dot{\alpha} \, \frac{1}{2}c}{U_\infty} \qquad (1)$$

where $\dot{\alpha}_{n.d.}$ is the non-dimensional angular rate

$\dot{\alpha}$ is the angular rate in rad/sec

$\frac{1}{2}c$ is the distance from the pivot point to the leading edge

U_∞ is the free stream velocity

5

Since the airfoil was pivoted about the mid-chord point, the numerator in the above equation corresponds to the velocity of the leading edge as it makes its circular path. The half-chord corresponds to the radius of the circle etched by the leading edge. Then

$$\dot{\alpha}\, \tfrac{1}{2}c = r\omega = V_{1.e.} \tag{2}$$

where   r is the radius

         ω is the angular velocity

         $V_{1.e.}$ is the velocity of the leading edge

The non-dimensional angular rate is then equivalent to the ratio of the velocity of the leading edge to the velocity of the air flowing past the airfoil section.

Accordingly, the purpose of this experiment was to examine the relationship between the separation angle of attack and the non-dimensional angular rate determined by varying the wing section angle of attack at a constant rate as opposed to a sinusoidal variation in angular rate. This was accomplished by studying films of smoke tunnel tests of this phenomenon and plotting data in an attempt to discover the relationship between the separation angle of attack and angular rate.

III. Experimental Approach

To analyze the relationship between separation and $\dot{\alpha}$, an NACA 0015 airfoil section was placed in a low Reynolds number Kenny Engineering smoke tunnel at the United States Air Force Academy Aeronautics Laboratory. During a series of experiments, the rate of increase in angle of attack was varied parametrically, and motion pictures were taken of the flow about the airfoil section.

The tunnel was run for three airspeeds over a range of $\dot{\alpha}$'s . Figure 4 shows a schematic of the smoke tunnel arrangement and the placement of the airfoil. The airspeed was varied by turning a knob on the front of the smoke tunnel, and the three airspeeds were later determined by film analysis.
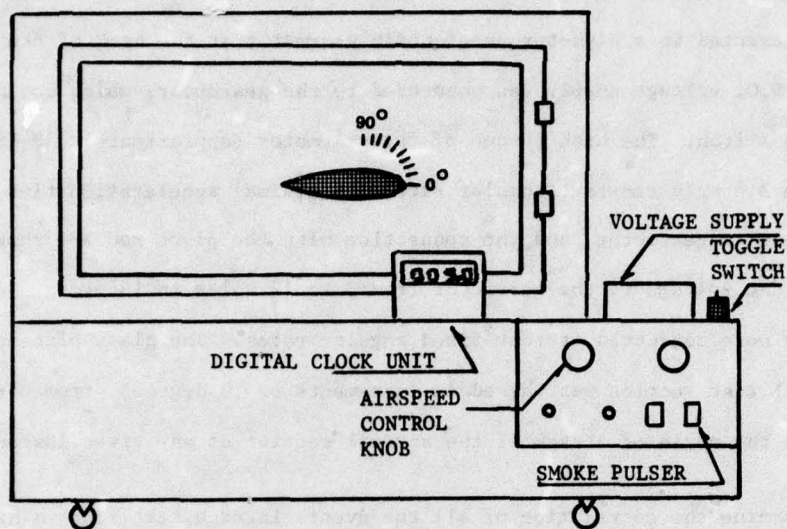
6

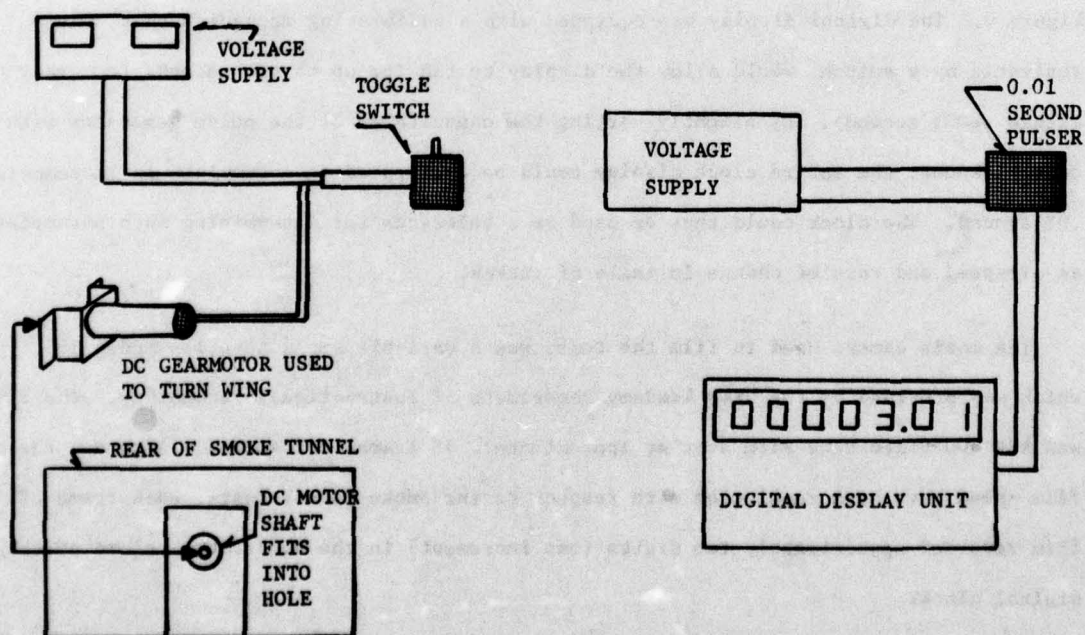**Figure 4. Schematic of Smoke Tunnel as Modified for Experiment**

Figure 5. Method Used to Rotate Wing Section

Figure 6. Digital Clock Mechanism

The airfoil section was mounted on a pivot rod at the mid-chord. The pivot rod, in turn, was connected to a high-torque electric gearmotor at the back of the smoke tunnel. A variable D.C. voltage supply was connected to the gearmotor, which could be actuated by a toggle switch. The high torque of the gearmotor (approximately 30 foot-pounds) resulted in a nearly constant angular rate with minimal acceleration time. The voltage supply, electric gearmotor, and the connection with the pivot rod are shown in Figure 5. By varying the voltage to the gearmotor from 3 to 12 volts in increments of 3 volts, the experiments were conducted at four fixed angular rates. The glass plate covering the smoke tunnel test section was marked in increments of 10 degrees, from 0 to 90 degrees, to indicate the angle of attack of the airfoil section at any given instant.

To determine the correlation of all the events in each test run, a high-speed, digital display clock was constructed and placed adjacent to the smoke tunnel test section. A movie camera simultaneously recorded the behavior of the smoke traces and the clock display. The clock was made up of a 5-volt voltage supply connected to a pulse generator, which, in turn, was connected to a cumulative digital display as shown in Figure 6. The digital display was equipped with a calibrating mechanism that, when activated by a switch, would allow the display to run for up to ten seconds (accuracy to within .0001 second). By slightly varying the capacitance of the pulse generator with control knobs, the entire clock display could be calibrated to accumulate in increments of .01 second. The clock could thus be used as a reference for determining such parameters as airspeed and rate of change in angle of attack.

The movie camera used to film the tests was a variable speed Aeroflex Model 16S, which was provided by the USAF Academy Department of Instructional Technology. The film was ASA 400 Video News Film shot at approximately 48 frames per second. Although the film speed gave high resolution with respect to the smoke tunnel tests, each frame of film recorded approximately two digits (one increment) in the hundredths column of the digital clock.

At the beginning of each experiment, the static separation angle of attack was visually determined, and an airspeed calibration run was made by filming a puff of smoke traversing a given distance across the test section with the airfoil at zero angle of

attack. The first voltage setting was selected and the airfoil was rotated from $\alpha = 0^o$ to a given angle of attack. This process was repeated for each of several higher angles of attack until some angle well past the dynamic separation angle was reached. Each rotation was filmed with the digital clock running to determine the angular rate. Similar rotations were made with the electric gearmotor set at the successively higher voltage settings previously mentioned. This entire process was repeated at each of the three airspeeds.

At the completion of the experiments, the film was developed by the Photographics Division of the Department of Instructional Technology. The film was then reviewed using a photo-optical data analyzer (L-W Photo, model 224-A-1) which could operate over a range of 0 to 24 frames per second.

IV. Observations and Discussion

Using the digital clock as a reference, the three airspeeds which varied slightly over the experiment were determined to be approximately 2.71, 3.38, and 6.07 feet per second. These yielded Reynolds numbers based on the chord length of 14,520, 18,110 and 32,520, indicating laminar flow.

The first test runs were made with the electric gearmotor set at 3 volts. The airspeed for this run was the lowest possible value, 2.71 feet per second. The 3-volt setting gave an angular rate of 25.38 degrees per second. At this airspeed the static separation angle (separation at approximately quarter chord) was observed to be 12.7 degrees; however, the dynamic separation at this angular rate was delayed until an angle of 18 degrees. Due to possible error in determining the point of separation, we judge that these angles were accurate to within 3 degrees. The flow remained completely attached until this angle was achieved. However, if the airfoil was rotated at this rate and stopped at any angle between static and dynamic separation, the flow separated within 0.2 seconds after the airfoil motion was stopped. The film also revealed that once the airfoil rotated beyond the dynamic stall angle, separation occurred in the same fashion as in the static case, whether the airfoil continued to rotate or not. Excerpts from the film of this run are shown in Figure 7.

$\alpha = 5°$
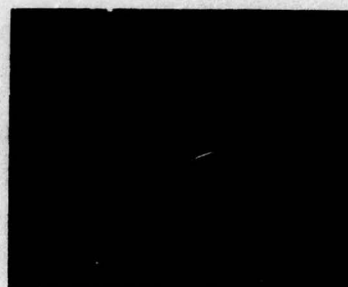
$\alpha = 10°$
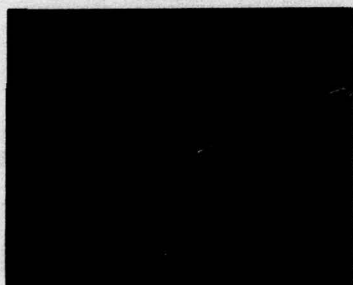
$\alpha = 20°$

$\alpha = 26°$
DYNAMIC SEPARATION

$\alpha = 30°$

$\alpha = 40°$
TOTAL SEPARATION

Figure 7.   Film Excerpts at Low Airspeed with $\dot{\alpha} = 25.38$ Deg sec

The next case examined was at the same airspeed but at 6 volts, yielding a pitching rate of 44.18 degrees per second. The dynamic separation angle of attack was observed at 28 degrees. When the airfoil section was rotated to 30 degrees, a small vortex formed just behind the leading edge (approximately $\frac{x}{c} = .10$) as soon as rotation was stopped. The vortex induced some reverse flow along the surface and shed within .5 seconds after formation. At angles of attack above 40 degrees, there was some leakage between the airfoil section and the glass plate covering the test section; however, this appeared to have negligible effect on the airflow about the airfoil. When the airfoil was rotated to higher angles of attack, another small vortex formed behind the leading edge at an angle of 41 degrees and shed at 48 degrees. A large vortex formed near the trailing edge on the bottom surface whenever the airfoil section rotated to an angle of 50 degrees or more. The fluid rotated in a clockwise sense, as opposed to the counterclockwise rotation of the upper surface vortices; however, since it shed immediately upon formation, there was no noticeable reverse flow on the airfoil itself.

The angular rate at the 9 volt setting was 68.07 degrees per second, and dynamic separation occurred at an angle of 36 degrees. A small vortex formed just behind the leading edge when the airfoil section rotated to 40 degrees at this rate. The vortex induced reverse flow, but shed immediately after the pitching motion stopped. When the airfoil rotated to higher angles of attack, a similar vortex formed at 50 degrees and was shed at 58 degrees. At still higher angles of attack, a large vortex formed over the entire upper surface and shed at an angle of 75 degrees.

At a rotation rate of 65.88 degrees per second (12 volts), the dynamic separation angle of attack was observed at 48 degrees. Whenever the wing section was rotated beyond 48 degrees, either a small vortex, or a separation bubble formed near the leading edge. At an angle of 90 degrees, a large vortex formed similar to the one at the 9 volt setting; this vortex induced considerable reverse flow along the entire upper surface. Excerpts from the film of this experimental condition are shown in Figure 8. (Note the significant increase in the dynamic separation angle of attack compared to Figure 7.) The effect of angular rate on separation may also be seen in a plot in Figure 9.

When the airspeed was increased to 3.38 feet per second, the wing section was tested

α = 20°   α = 40°

α = 60°
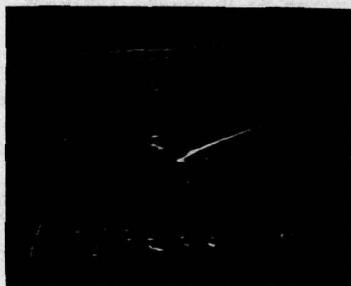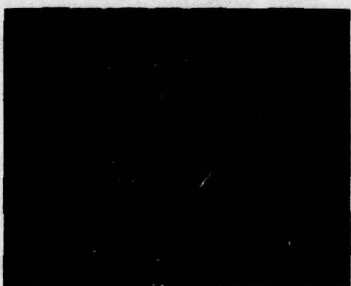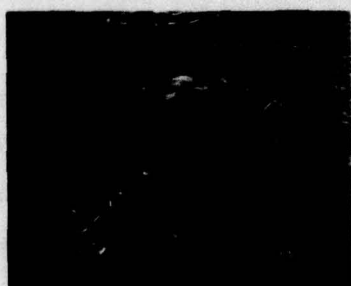
α = 60°   α = 60°

FORMATION OF LARGE VORTEX   SHEDDING OF LARGE VORTEX
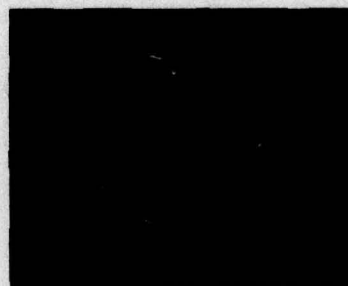
Figure 8.   Film Excerpts at Low Airspeed with $\dot{\alpha}$ = 85.66 Deg sec

Figure 11. NACA 0015 Airfoil Smoke Tunnel Data for V = 6.07 FPS

SEPARATION ANGLE OF ATTACK, α_s (DEGREES)

NON-DIMENSIONAL ANGULAR RATE $\left(\dfrac{\dot{\alpha} \cdot c}{U_\infty}\right)$

Figure 10. NACA 0015 Airfoil Smoke Tunnel Data for V = 3.38 FPS

SEPARATION ANGLE OF ATTACK, α_s (DEGREES)

NON-DIMENSIONAL ANGULAR RATE $\left(\dfrac{\dot{\alpha} \cdot c}{U_\infty}\right)$

Figure 9. NACA 0015 Airfoil Smoke Tunnel Data for V = 2.71 FPS

SEPARATION ANGLE OF ATTACK, α_s (DEGREES)

NON-DIMENSIONAL ANGULAR RATE $\left(\dfrac{\dot{\alpha} \cdot c}{U_\infty}\right)$

at the same four angular rates as during the low speed tests. At these angular rates, dynamic separation occurred at angles of 21, 32, 38, and 42 degrees respectively. Static separation angle of attack at this airspeed was measured at 12 degrees. Large and small vortices were observed to form in a manner identical to that found at the low airspeed; however, the large vortex separated immediately after formation if the airfoil was rotated to 80 degrees or more. If the pitching motion was stopped below this angle of attack, the large vortex remained attached for up to one second. A plot of the results obtained at this airspeed is shown in Figure 10.

Finally, the airspeed was increased to 6.07 feet per second. The four dynamic separation angles were 18, 27, 31 and 39 degrees, indicating a decrease in separation incidence with an increase in airspeed. Vortices formed in identical fashion as at the lower airspeeds, but they appeared to shed sooner after formation. The plot for these results are shown in Figure 11.

There were a few common phenomena in all the test runs. The higher the angular rate, the further beyond the static stall angle the airfoil section rotated before separation occurred. The high airspeed reduced the dynamic separation angle of attack only 5 to 10 degrees from the angles at the low airspeed. A separation bubble formed over the upper surface whenever the airfoil section rotated well beyond the static separation angle of attack.

One possible explanation for dynamic separation occurring at high angles of attack is the downward relative velocity component of the free stream (relative to the airfoil section) near the leading edge. This explanation, along with the suction induced near the trailing edge could have caused the flow to remain attached as the wing section rotated. The large vortex which appeared over the upper surface probably did not affect the dynamic stall angle of attack (as defined in this paper), since dynamic separation began well before this vortex formed in tests where the airfoil rotated to high angles of attack.

Although many of these phenomena are not yet fully understood, there appears to be a predictable relationship (as shown by Figure 12) between a constant angular rate (non-dimensionalized) and dynamic separation.
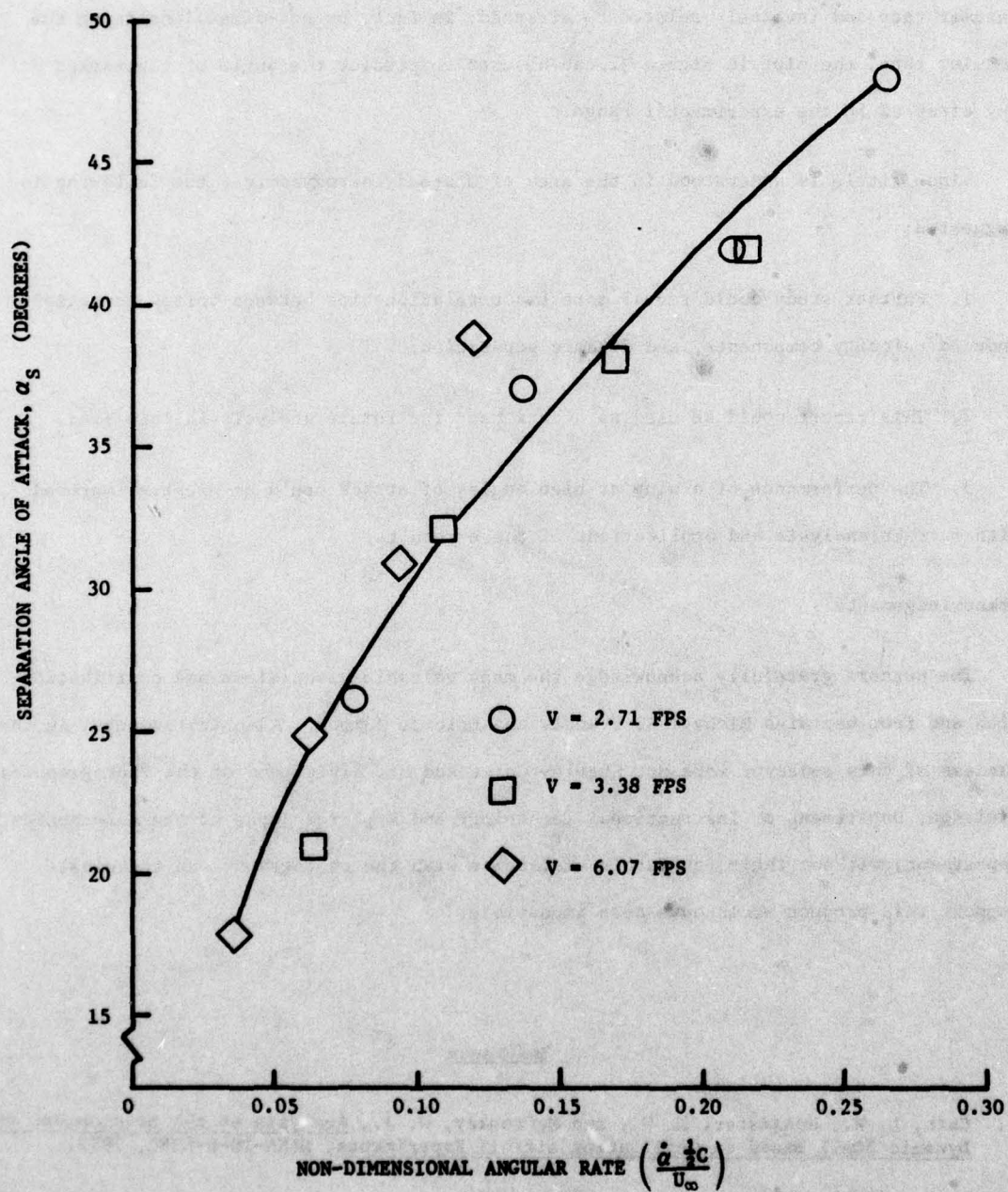
Figure 12. NACA 0015 Airfoil Smoke Tunnel Data

V. Conclusions and Recommendations

Rotating an airfoil section through the static separation angle of attack at high rates delays separation. The dynamic separation angle appears to be directly related to angular rate and inversely related to airspeed; in fact, by non-dimensionalizing the angular rate, the plot in Figure 12 can be used to predict the angle of separation at any airspeed in the experimental range.

Since little is understood in the area of unsteady aerodynamics, the following is suggested:

1. Further study could reveal more exact relationships between vortex formation, induced velocity components, and dynamic separation.

2. This report could be used as a data base for future analysis in this area.

3. The performance of a wing at high angles of attack could be greatly improved with further analysis and applications of these results.

Acknowledgements

The authors gratefully acknowledge the many valuable discussions and contributions with and from Captains Michael S. Francis and Eric J. Jumper. Also instrumental in the success of this endeavor were Mr. Stanley Geist and Mr. Alvin Lamz of the Photographics Division, Department of Instructional Technology and Mr. Fred Jayne of the Aeronautics Department; without their invaluable assistance with the photography and technical support, this project would have been impossible.

Reference

1. Carr, L. W., McAlister, K. W., and McCroskey, W. J., Analysis of the Development of Dynamic Stall Based on Oscillating Airfoil Experiments, NASA-TN-D-8382, 1977.

EXPERIMENTAL MEASUREMENT OF SAILPLANE TOWROPE LOADS
J. P. Retelle, Jr.[*] and F. H. Zeitz[**]

Abstract

Sailplane towrope loads were measured in flight using an instrumented towplane tow hook and two trainer sailplanes. The measured loads reflect both the good and bad performance of student pilots on calm soaring days, but do not include the effects of strong turbulence or rotor activity. Additional data on the influence of towrope age, as well as current practices of placing knots in ropes, should be of interest to soaring clubs and other flight instruction activities. It was found that, even for the most violent maneuvers tested, the towrope loads were less than 15 percent of the measured towrope breaking strength, and less than 34 percent of the gross weight of the Schweitzer 2-33 glider. The results are meant to provide a baseline of experimental data as background for possible alterations of the Federal Aviation Administration regulations on required towrope strengths.

I. Introduction

Current Federal Aviation Administration (FAA) regulations regarding sailplane towrope strengths are quite specific: The towrope must have a breaking strength no greater then 200 percent and no less than 80 percent of the maximum gross weight of the sailplane (F.A.R. 91.17(3))(Ref. 1). Both a literature search and contact with the FAA reveal that this regulation is based upon a very meager amount of experimental technical data. The current towline strength regulation appears to be based upon early experiments which measured towline loads from a single glider during a winch tow. The experiment described below measured towrope loads during aerotows in order to provide additional data to serve as background for possible updating of the current regulations.

The requirement on towrope loads is actually a reflection of concern for the structural loads sustained by the sailplane tow hook and towplane tow hook. The sailplane tow hook and surrounding structure, although designed for low weight, is one of the strongest parts of the aircraft and does not represent a structural load problem. The tail structure of the towplane, however, is usually designed to save weight and usually represents the principle structural constraint when towing gliders. To satisfy the requirements cheaply, and also to allow commercially available light aircraft to serve as towplanes, the FAA placed the requirements on the towrope. Weak links of smaller rope, which themselves satisfy the towrope strength requirements[†], are permitted to be used when sailplanes of widely different gross weights are towed by the same towplane and towrope. This experiment measured the towrope loads during aerotows of gliders during normal operations.

---

[*] Captain, USAF, Assistant Professor of Aeronautics, DFAN

[**] 2nd Lt, USAF, Instructor Cadet Soaring Program, CW

[†] a 25 percent greater strength link is allowed at the towplane end but not more than 200 percent of the glider gross weight

If the loads collected during aerotows were lower than those measured during winch tows, perhaps the requirements of the regulation could be relaxed somewhat, providing weight and cost savings for aerotow operators, while still providing adequate safety. An extension of this analysis could be that towplanes currently certified to tow only light-weight gliders could tow heavier gliders if appropriate weak links were used. Additional experiments described below provided some experimental data on the influence of towrope breaking strength due to rope age and the presence of knots in the rope.

II. Description of Experiment

The tests were conducted using Schweitzer 2-32 and 2-33 gliders at the United States Air Force Academy. These gliders, normally used for cadet flight instruction, were flown during the test by a certified flight instructor and towed by a Piper Super-Cub aircraft with a 180 horsepower engine. Weights and other data for all aircraft are shown in the Appendix.

Towing loads were measured in flight using a strain-gage glued to the towplane tow hook. The strain-gage calibration shown in Figure 1, was obtained on a tensile strength test stand in the Mechanical Engineering Laboratory at the Academy. The strain gage was wired as one leg of a Wheatstone bridge, and the bridge output, measured on a volt-meter, was calibrated directly in pounds. The voltmeter output was hand-recorded in flight by an observer in the rear seat of the towplane.

Flight profiles were planned to include the towline loads produced by both the typical performance, and the typical mistakes, of student pilots. A baseline flight generated data on standard loads with no perturbations. Later flights, described in Table 1, included normal training maneuvers, such as boxing the propwash and slack line recovery, as well as maneuvers involving poor tow position and coordination. Our test plan was developed by dividing the actual aerotow into four segments: the ground roll, the takeoff climbout, the main tow, and the release. Each segment of the tow was tested individually to determine what kind of loads would be encountered in that par-ticular portion.

The test for high loads on takeoff roll was made by starting the takeoff with a slight amount of slack in the rope rather than by starting with the rope taut. A second test for high loads on takeoff involved dragging the skid of the sailplane during the takeoff roll. The takeoff climbout was the portion of flight immediately after leaving the ground before normal towing conditions were established (somewhere before the first turn in the cadet soaring operation). The two sources of high loads which were unique to this segment of tow are sideslipping immediately after takeoff as in a cross-wind, and a rapid pitch-up of the sailplane to catch up to the towplane as it begins its climbout. The high loads during normal tow were caused mainly by being out
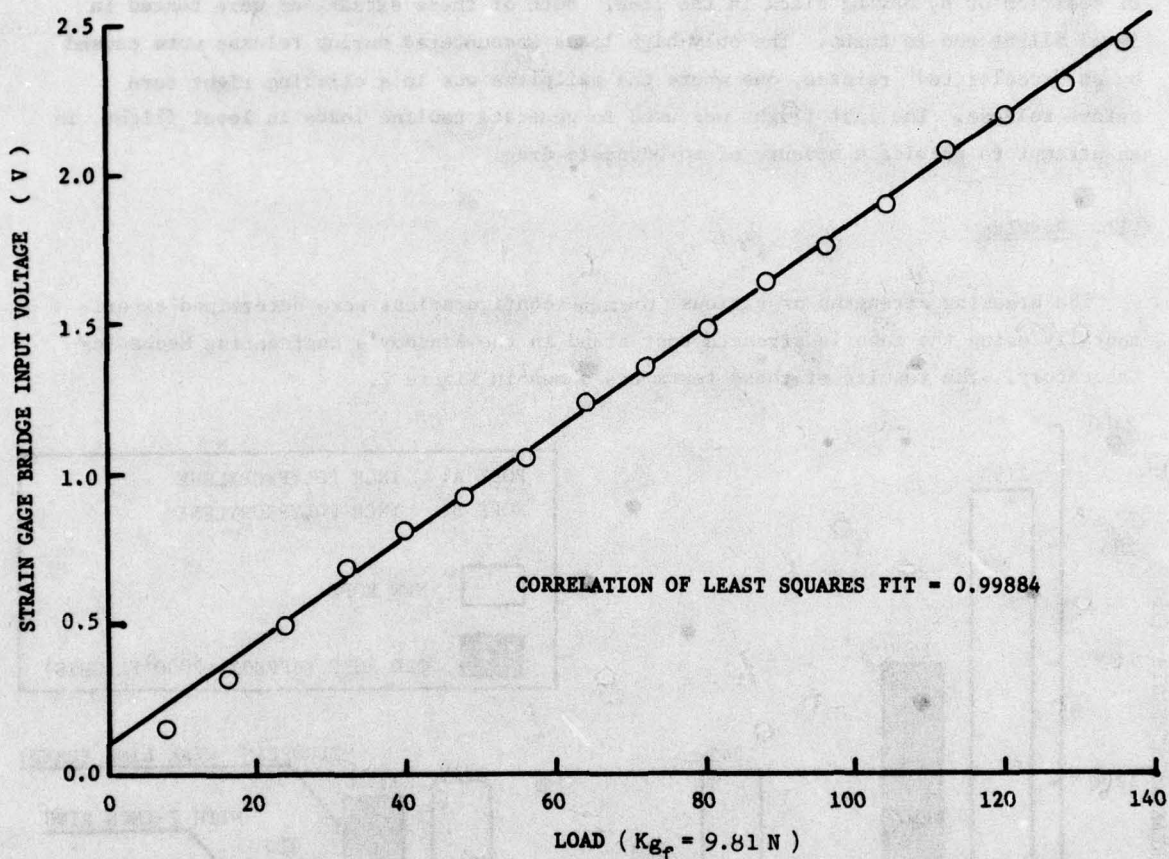
Figure 1. Calibration of Tow Hook Strain Gage Transducer

Table 1

FLIGHT PROFILES

Flight 1	Baseline Flight - Gather data on standard loads (no perturbations).
Flight 2	Slack Rope Takeoff Box the Wash (Improper Tow Position) Accelerated Release
Flight 3	Drag the skid on takeoff. Side slip after takeoff. Slack rope on tow (level flight). Accelerated release.
Flight 4	Zooming after takeoff. Out of position in turns. Slack line in turns.
Flight 5	Level flight loads Turbulence loads

of position or by having slack in the line. Both of these situations were tested in
level flight and in turns. The only high loads encountered during release were caused
by an "accelerated" release, one where the sailplane was in a climbing right turn
before release. The last flight was used to generate towline loads in level flight in
an attempt to provide a measure of aerodynamic drag.

III. Results

The breaking strengths of various towrope configurations were determined experi-
mentally using the tensile strength test stand in the Academy's Engineering Mechanics
Laboratory. The results of these tests are shown in Figure 2.
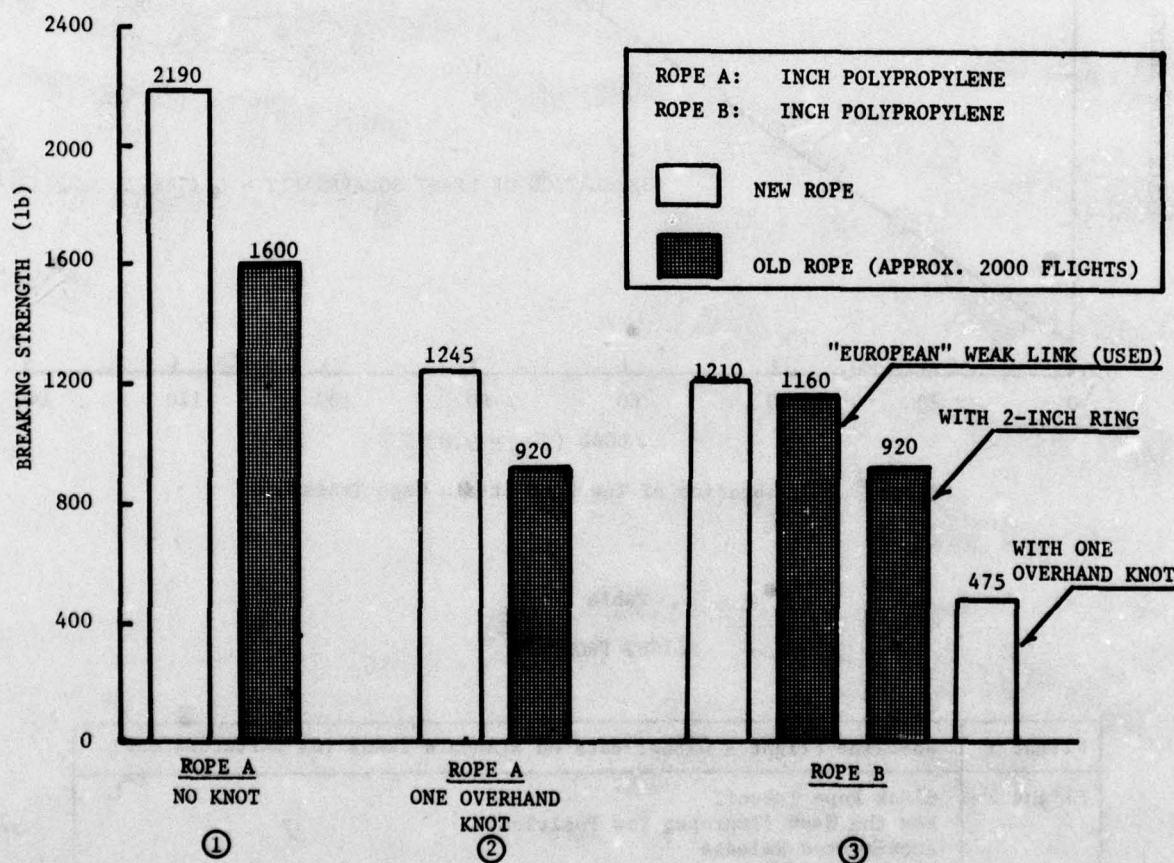
Figure 2. Breaking Strengths for Various Rope Configurations

The first set of data on rope A, the 3/8 inch polypropylene rope normally used for
Academy towing, shows a 27 percent decrease in breaking strength after the rope has been
used for approximately 2000 flights. (It should be noted that the measured breaking
strength was 40 pounds more than the manufacturer's indicated breaking strength of 2150
pounds.) The second set of data shows the effect of putting one overhand knot in the

line which was, until recently, a standard practice at the Academy, since the prescribed rope breaking strength was more than 200 percent of the glider gross weight. For a new rope, the breaking strength with one knot was reduced by 43 percent. After about 2000 flights, the knotted rope had a 42.5 percent decrease in breaking strength. The third set of data are for rope B, a ¼ inch polypropylene rope of 1100 pound (prescribed) breaking strength used for weak links. The figure shows the degradation of breaking strength using a three-inch ring (the standard configuration) and then an additional overhand knot. The addition of the knot in the weak link produced a 79.9 percent decrease in breaking strength.

Flight test data, presented in Figure 3 for the Schweitzer 2-33 glider, compare the two rope loads measured during each segment of the baseline flight to those measured for the unusual maneuvers performed during later flights. The numbers shown represent average values, except where the data indicated a peak or impulse force in which case the peak loads are presented. The baseline data show a fairly constant load of 128 pounds average. The snapping of the towrope on takeoff roll produced a peak of a 23 percent increased load, and the snapping of the line during an intentionally unskilled slack-rope recovery produced a peak of a 182 percent. Pull-up maneuvers during the climbout and release produced load increases of 47 percent and 78 percent respectively. The load changes produced by intentionally poor technique during the turns produced very small maximum load changes of 25 percent. Figure 4 presents the towrope loads during the "boxing-the-prop-wash" training maneuver. The strongest loads were noted when the sailplane was ascending outside the propwash, and were 50 percent higher than in straight flight. By ascending through the prop wash, the sailplane pilot increased the towrope loads to 80 percent above those measured in straight flight.

The towrope loads obtained while towing a heavier glider, the Schweitzer 2-32, are shown in Figure 5. The peak load during the takeoff roll is higher than for the 2-33, as might be expected. It is interesting to note that the loads experienced while maneuvering are a fairly constant 14 percent higher than the loads measured in straight flight. The high drag produced by the spoilers on this glider are also noted.

Data were collected for both gliders on tow to determine the glider drag in straight and level flight by towing at a constant altitude and airspeed for approximately three minutes. At a tow speed of 60 miles per hour and at 8500 feet altitude, the Schweitzer 2-33 produced an average rope load of 81 pounds. At a tow speed of 70 miles per hour at the same altitude, the Schweitzer 2-32 produced an average load of 110 pounds. These loads represent drag coefficients of $C_D = .051$ and $C_D = .062$ for the 2-33 and 2-32 gliders, respectively. While somewhat inaccurate, these numbers are not unreasonable. The rope alone was found to produce an average load of 15 pounds after sailplane release.
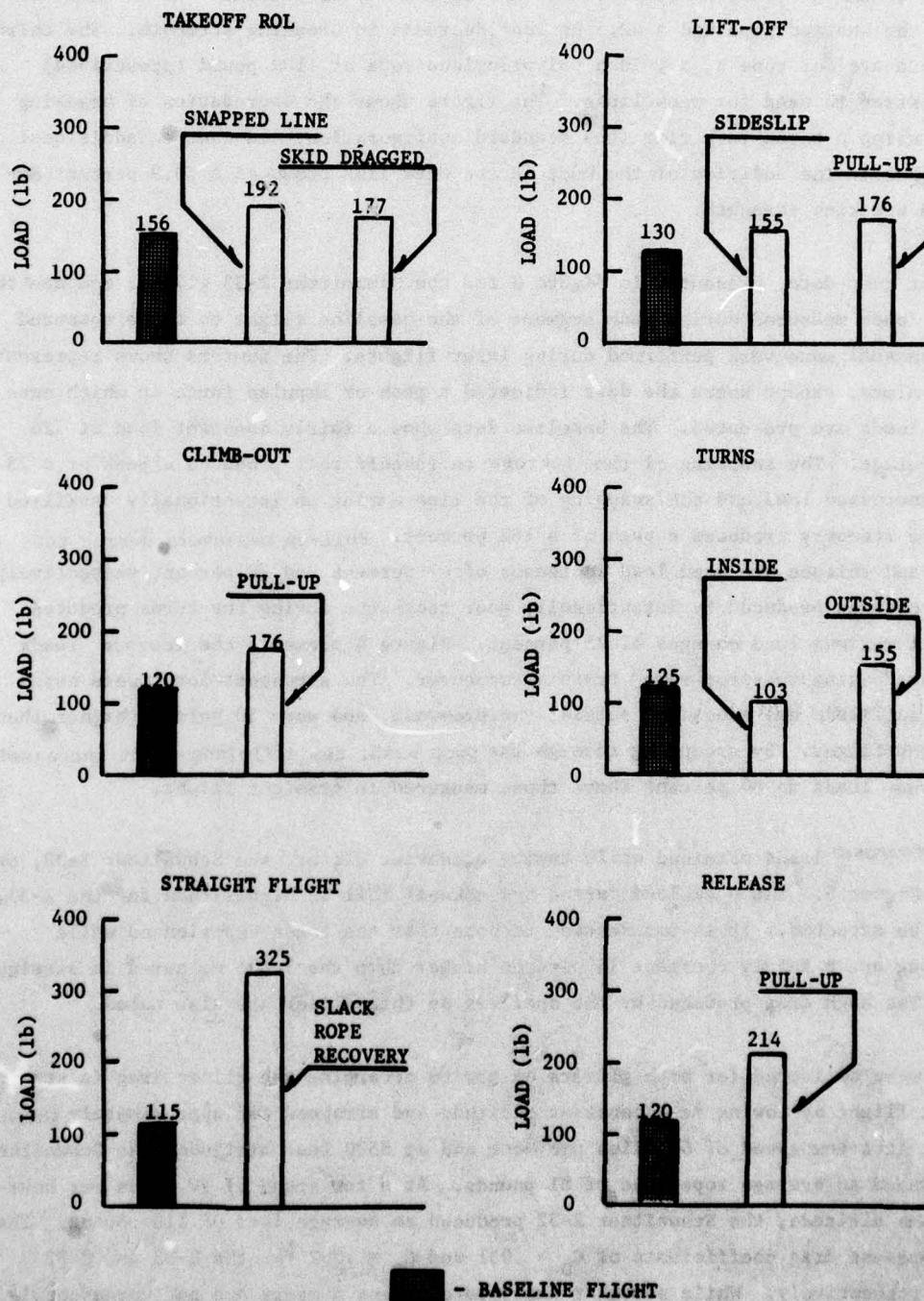
Figure 3. Measured Tow Loads for SGS 2-33
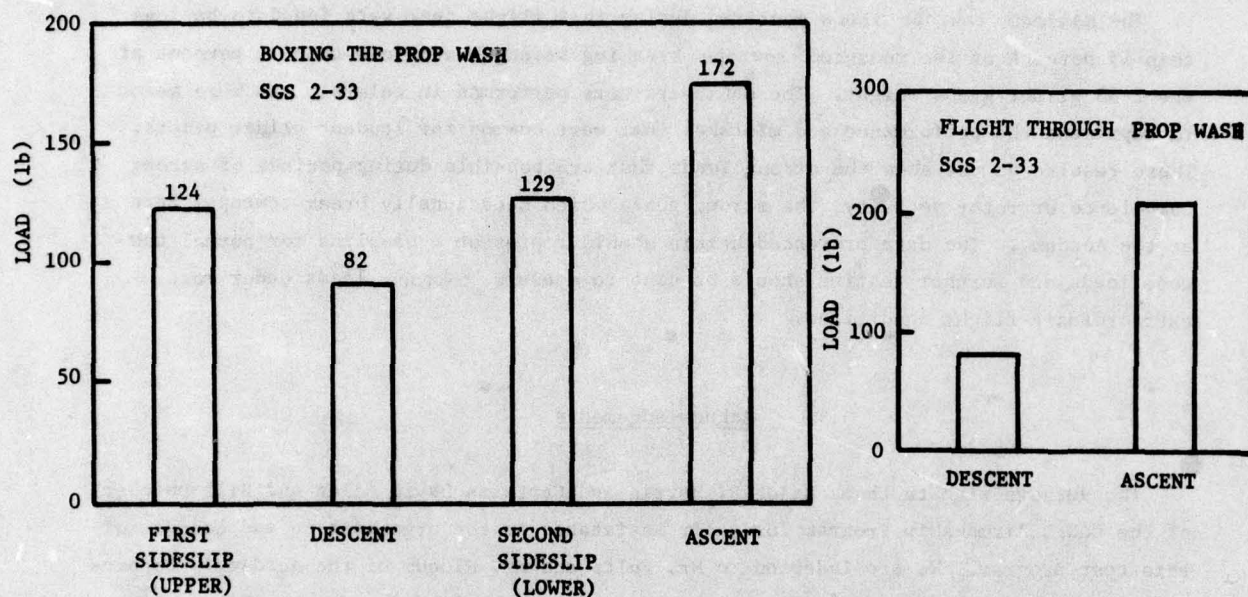
Figure 4. Measured Tow Loads for SGS 2-33
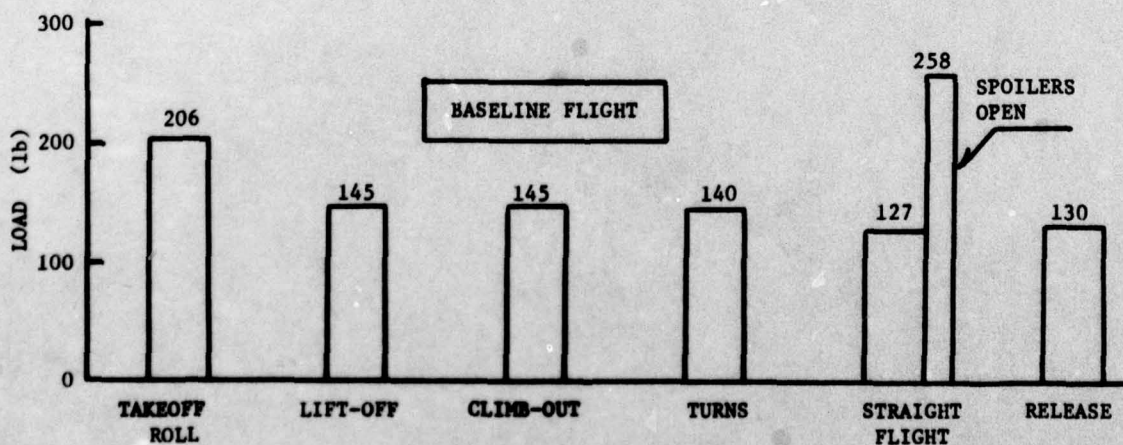
Figure 5. Measured Flight Loads for SGS 2-33

IV. Summary

The maximum towrope loads measured during this flight test were found to be less than 15 percent of the measured towrope breaking strength and less than 34 percent of the 2-33 glider gross weight. The maneuvers were performed in calm air and were meant to represent the performance and mistakes that were common for student glider pilots. These results do not show the strong loads that are possible during periods of strong turbulence or rotor activity, the strong gusts which occasionally break towropes here at the Academy. The data presented herein should represent a baseline for normal towrope loads, and further testing should be done to measure towrope loads under more extraordinary flight conditions.

Acknowledgements

The authors wish to thank Major R. Harris and Captains David Allen and Bill Dutcher of the Cadet Airmanship Program for their assistance in the organization and conduct of this test program. We are indebted to Mr. Fultz and Mr. Slocum of the Academy's Department of Engineering Mechanics for their assistance in the laboratory. Mr. Ed Sergeant served as the pilot of the towplane.

References

1. _Soaring Flight Manual_, Soaring Society of America, Denver, Jeppesen Sanderson, Inc., 1978, pp. 6-28 - 6-29.

APPENDIX

AIRCRAFT DATA

Schweitzer 2-33A, N 7760S

               gross weight (with crew) - W = 980 pounds (Max: 1040)

               cg position - 94.10 inch

               tow speed - 60 mph

               wing surface area - S = 219.5 ft^2

Schweitzer 2-32, N 2898H

               gross weight (with crew) - W = 1265 pounds (Max: 1430)

               cg position - 112.34 inch

               tow speed - 70 mph

               wing surface area - S = 180 ft^2

Piper PA 18-180   Super Cub, 180 HP

               N 3594P

               gross weight (with crew) - W = 1240 lb

TOWROPE Data   3/8 inch polypropylene, 2150 pound breaking strength

               ¼ inch polypropylene, 1100 pound breaking strength

SECTION II

FLUID MECHANICS

AN INTUITIVE LOOK AT VISCOUS FLOW
Eric J. Jumper[*]

Abstract

This paper discusses viscous flow based on some simple observations of a fictitious experiment. The experiment is a contrived apparatus which simulates impulsive start motion of a flat plate in an at-rest fluid bath. Based on the observations, predictions about the nature of boundary layer phenomena are made and compared to the Exact Blasius solution of a boundary layer on a flat plate.

I. Introduction

There are many who have derived the boundary layer equations and even solved and used the results to make predictions; but, there are surprisingly few who feel that they have a good intuitive feel for just what is happening in a boundary layer and, further, just what to expect if a given set of conditions for which the behavior is known are changed. In what follows I will describe a set of simple observations upon which I feel the entire understanding of boundary layer theory rests (or at least a large part of it).

In order to interpret the observations we will make, it will be necessary to first understand some preliminaries.

A. Backgound

If you want to limit the required understanding of preliminaries to a bare minimum, you would have to deal with the ideas of the no-slip boundary condition and of shear stress in a fluid. Of course, these two ideas open up an entire array of topics which are already documented far more completely than I could ever do here (for example, see references 1 and 2). Let us start by realizing that we will be treating a fluid as a continuum (and a Newtonian fluid). In doing so, we are able to refer to a rather complicated two-phase molecular interaction taking place on a solid/fluid interface as simply a no-slip condition. In the usual sense of a fluid moving past a flat plate, this would mean the portion of the fluid continuum right in contact with the surface is not moving with respect to the plate. Of course, since the fluid is, on the whole, moving with

---

[*]Captain, USAF, Associate Professor of Aeronautics, DFAN

respect to the plate, at some free stream velocity, there must be present a region where the fluid undergoes a velocity gradient from zero at the wall to free stream velocity at the edge of the region.

This region in which the effect of the no-slip boundary condition is contained is commonly referred to as the boundary layer. It is defined as the region next to a solid boundary where the fluid goes from zero velocity at the wall out to 99% of the freestream velocity. The distance from the wall to the 99% point is called the boundary layer thickness, δ.

Since the fluid is "losing" velocity as one scans from the boundary layer thickness toward the wall, one might think that the fluid has, in effect, a region which is experiencing a momentum defect, momentum being the mass times the velocity. Since there is a change in momentum throughout the boundary layer, it is not surprising to find the presense of forces and, in particular, the appearance of significant shear stresses (force per unit area). The shear stress, τ, in the fluid is defined as

$$\tau = \mu \frac{\partial u}{\partial y} \tag{1}$$

where μ is the coefficient of viscosity of the fluid, u the velocity and y the distance from the wall. It is indeed reassuring to find that because the shear stress is directly proportional to the velocity gradient, the equation would predict a shear stress in the boundary layer.

Since we have already assumed the fluid is a continuum, any shear stress in the bottom of a layer of fluid will be balanced by the top of the layer just below it. This must also hold right at the wall. The shear stress in the fluid right at the wall shows up as a tangential force. Thus, the shear stress at the wall

$$\tau_{wall} = \mu \frac{\partial u}{\partial y}\Big|_{y = 0} \tag{2}$$

makes its presense felt as a drag force per unit area, commonly referred to as skin
friction drag.** We move now to a description of our experiment.

II. The Experiment

The imaginary experiment which we will attempt to construct here is a physical picture
of an exact solution for the so-called suddenly accelerated plane wall in an initially at-
rest fluid bath (or impulsive start motion) (Ref 3).

A. Experimental Apparatus

Let's imagine, then, an experimental set-up as shown schematically in Figure 1.
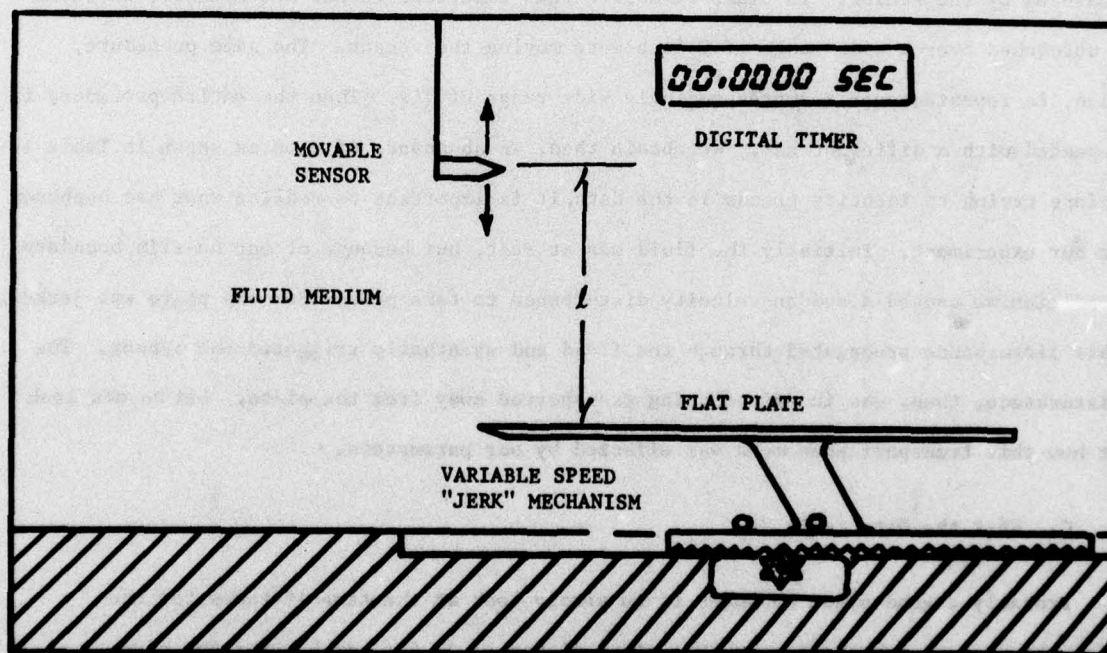
FIGURE 1. Schematic of Experimental Set-up

It consists of a flat plate movable in the horizontal plane. It is driven by a controll-
able variable speed (jerk) machine which can accelerate the plate instantaneously to a
pre-selected speed. The plate is enveloped in a changeable fluid medium. In this case,
the fluids we will select will be gases as opposed to liquids. A positionable sensor is

---

**The word friction is, in fact, a very poor choice of words. While it does infer re-
sistance to motion, friction in the normal sense requires relative motion; recall from our
discussion of the continuum, the fluid at the surface is not moving. From the discussion
in this paper it should become obvious that the drag phenomena we are dealing with in
viscous flow does not in the least resemble a friction-type phenomena.

hung over the plate so that it can be repositioned between experiments, but once positioned, remains fixed throughout a given run. The sensor is able to detect a velocity disturbance, and once detected, shut off a digital timer which is initially activated at the start of an experiment. An experiment begins when the plate is set into motion.

B. Taking the Data

We now begin to take the data. The procedure is to select a sensor distance, l, above the plate, the desired plate speed, V_p, assure the fluid is still and, finally, throw the start switch which jerks the plate and starts the timer. The timer shuts off when the velocity disturbance ratio, u'/V_p, reaches 0.01, where u' is the velocity measured by the sensor. In order to assure that important trends are noticed, we leave l untouched over a wide range of V_p's before moving the sensor. The same procedure, then, is repeated over a correspondingly wide range of l's. Then the entire procedure is repeated with a different gas. We obtain then, an abundance of data as shown in Table 1. Before trying to identify trends in the data, it is important to realize what has happened in our experiment. Initially the fluid was at rest, but because of our no-slip boundary condition, we caused a sudden velocity disturbance to take place when the plate was jerked. This disturbance propagated through the fluid and eventually triggered the sensor. The disturbance, then, was in effect being transported away from the plate. Let us now look at how this transport phenomena was effected by our parameters.

C. What the Data Tells Us

Probably a good place to start is to simply look at the time it takes for the disturbance to reach the sensor at a given distance, l_1 for gas A. For the purpose of discussion let's assume that l_1 is our closest sampling distance. First we look at the time t_{11} which is the time for the disturbance to travel to l_1 for a plate speed of V_{p_1}. Again let's assume V_{p_1} is our slowest speed. The time has little or no meaning to us at this point except as a reference. One thing we might wonder about is how this time might be affected by increasing the speed, V_p; after all, it does seem that if V_p were increased, a more "violent" disturbance might be formed and our logic might tell us that the time to travel a distance l_1 would be decreased. In examining t_{12}, however, we find this is not the case. In fact, we find that all the times connected with the distance l_1

TABLE 1

Results of Experiment

GAS 1			GAS 2	GAS 3
l	V_p	time		
l_1	V_{p_1}	t_{11}		
l_1	V_{p_2}	t_{12}		
.	.	.	etc.	etc.
.	.	.		
.	.	.		
l_1	V_{p_n}	t_{1_n}		
l_2	V_{p_1}	t_{21}		
l_2	V_{p_2}	t_{22}		
.	.			
.				
.				
l_2	V_{p_n}	t_{2_n}		
	etc			

for a given gas are exactly the same.

In order to assure ourselves that this is a rule, we examine the times for ℓ_2 , ℓ_3 , etc. and find that, indeed, the time doesn't depend on the speed V_p . We do find, however, that the time increases as ℓ increases; the relationship is a square, that is,

$$t \propto \ell^2 \tag{3}$$

We also find that at a given ℓ , t changes depending on the type gas we use. Thus, t is not only a property of the distance, ℓ , but also of the particular fluid medium we are using.

In examining the properties of the fluids and comparing the times, we find that the times for a given fluid as compared to another fluid differ by the ratio of kinematic viscosities , ν , (more often given as μ/ρ where ρ is the density) so that

$$\frac{t_A}{t_B} = \frac{\nu_B}{\nu_A} \tag{4}$$

where the subscripts compare gases A and B, for example, and the relationship holds as long as $\ell_A = \ell_B$. The time, then, to travel a distance ℓ now becomes

$$t \propto \frac{\ell^2}{\nu} \tag{5}$$

It is interesting to examine the meaning of the kinematic viscosity , ν , in light of the above. It appears that ν is, in effect, a transport property, transport in the sense that it relates to the transport efficiency of a velocity (or momentum) disturbance. The units of ν are $\frac{m^2}{s}$ in SI units. Comparing the units of the kinematic viscosity with other transport properties such as the diffusivity, $\mathcal{D}$, in mass transport and the thermal diffusivity, α , in heat transport, we see that they all have the same units, $\frac{m^2}{s}$.

Perhaps a better name for ν might be the momentum diffusivity.

Returning to the lesson our experiment tells us, the time for a velocity (or momentum) disturbance to travel a distance ℓ is given by

$$t = C \frac{\ell^2}{\nu} \tag{6}$$

where C is the constant of proportionality. We must now ask the question "how does this result tell us anything about boundary layers?"

III. What About Boundary Layers

It seems to me that we now have the essential key to describing what goes on in a boundary layer. In order to use it, however, we should first formulate a picture of what might be going on. Let's look at the formation of a boundary layer on a flat plate. A hypothetical picture of what might be going on is shown schematically in Figure 2. The key is that we are looking on the boundary layer as simply the manifestation of a sudden velocity (or momentum) disturbance (at B) being propagated out away from the plate into an otherwise undisturbed fluid (at A).
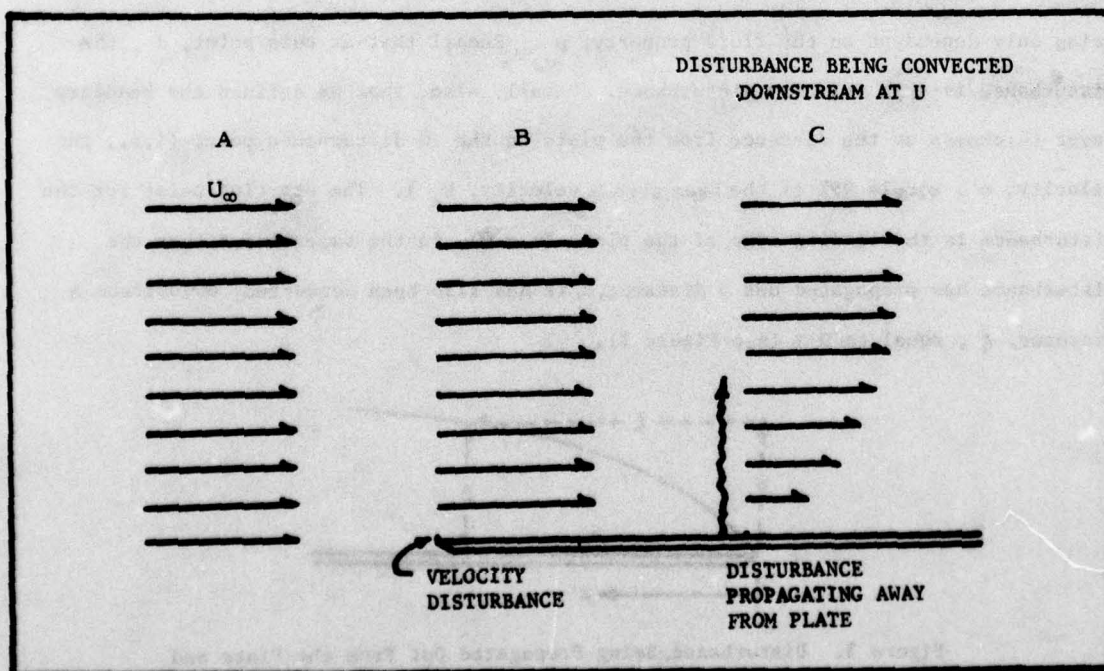
Figure 2. Boundary Layer Being Looked at as the Propagation of a
Disturbance

The only difference between what we see here and our earlier experiment is that the fluid is being convected along at a velocity U_∞. If this picture is correct, then 1) we must be able to make predictions and compare them favorably against the exact solution, and 2) if the predictions check we must accept the fact that boundary layers are not as complicated as they have been cracked up to be. First the predictions.

A. Predictions

If our model is correct, we should easily be able to predict the boundary layer thickness as a function of distance down the plate, x . From our experiment we already know that the rate at which the disturbance propagates away from the plate is independent of the plate velocity or in our new case (a change of reference frame) the fluid velocity, U_∞ . Therefore, we should be able to expect that the disturbance will arrive at a distance, d , above the plate in time

$$t = C \frac{d^2}{\nu} \qquad (7)$$

being only dependent on the fluid property, ν . Recall that at this point, d , the disturbance is a 1% velocity disturbance. Recall, also, that we defined the boundary layer thickness as the distance from the plate to the 1% disturbance point (i.e., the velocity, u , equals 99% of the free stream velocity, U_∞). The starting point for the disturbance is the leading edge of the plate (x = 0), in the same time, t, that the disturbance has propagated out a distance, d, it has also been convected downstream a distance, ξ , equal to $U_\infty t$ (see Figure 3).
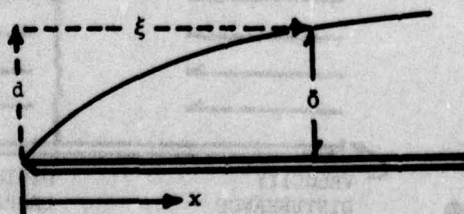
Figure 3. Disturbance Being Propagated Out From the Plate and Convected Downstream

By definition, this distance is equal to the boundary layer thickness, δ, corresponding to the d in Eqn (7). So that in general,

$$t = \frac{x}{U_\infty} \qquad (8)$$

and

$$\delta = \sqrt{\frac{t\nu}{C}} \qquad (9)$$

or

$$\delta = C' \sqrt{\frac{x\nu}{U_\infty}} \qquad (10)$$

making the substitution for the Reynolds number based on x, R_{e_x}, Eqn (10) can be written

$$\delta = C' \frac{x}{\sqrt{R_{e_x}}} \qquad (11)$$

This is our first prediction. Notice that we have predicted the functional form of the boundary layer thickness including free stream velocity, distance down the plate, and the appropriate fluid property; it would be more than coincidence if this prediction turned out to be correct.

Now that we have a formula for predicting the boundary layer thickness, we can make some predictions about what happens to the boundary layer as we change the free stream velocity. From Eqn (10) we can see that as the velocity increases, the boundary layer thickness at the same location decreases. Intuitively, then, the rate at which the disturbance propagates away from the plate is unchanged, but in the same time it has been convected farther downstream. The slower the freestream velocity, then, the thicker the boundary layer.

Even though we don't know the exact shape of the velocity profile in the boundary layer, we can also make predictions about the shear stress at the wall (drag per unit area) using the following argument. We know the shear stress at the wall is given by Eqn (2); we are, therefore, looking for the slope of the velocity profile right at the

wall. We also know that the velocity must go from zero to U_∞ over the distance δ. As a quick approximation, let's assume the change is linear, thus

$$\left.\frac{\partial u}{\partial y}\right|_{y=0} \sim \frac{U_\infty}{\delta} \tag{12}$$

at a minimum we know this will give us a ball park estimate. Thus, the gradient of the velocity is inversly proportional to the boundary layer thickness. As the velocity in the free stream is increased, the boundary layer thickness decreases and the gradient must increase. So, as the velocity increases, the shear stress (thus, the drag) increases. Our predictions are summarized in Table 2.

Table 2

Summary of Predictions Based on Intuitive Model

Change in U_∞	Effect on		functional form of δ
	δ	τ_ω	
increase	decrease	increase	$\delta = C \dfrac{x}{\sqrt{R_{e_x}}}$
decrease	increase	decrease	

B. Checking our Predictions

Fortunately, the exact solution for the boundary layer on a flat plate is well known. The first solution of this problem (incompressible) was obtained by H. Blasius in 1908 (Ref 4) and is thus known as the Blasius Solution. The governing equations are, of course, the continuity and momentum equations,

continuity:

$$\frac{\partial u}{\partial x} + \frac{\partial v}{\partial y} = 0 \tag{13}$$

momentum:

$$u \frac{\partial u}{\partial x} + v \frac{\partial u}{\partial y} = \nu \frac{\partial^2 u}{\partial y^2} \tag{14}$$

where u is the velocity in the x direction and v in the y. The solution is given in Figure 4 (Ref 5). We can see from Figure 4 that the 1% disturbance point ($U/U_\infty = .99$) occurs at $\eta = 5.0$. At this point y must equal δ. Thus,

$$5.0 = \delta \sqrt{U_\infty / \nu x} \tag{15}$$

or

$$\delta = 5.0 \sqrt{\frac{\nu x}{U_\infty}} = \frac{5.0\ x}{\sqrt{R_{e_x}}} \tag{16}$$
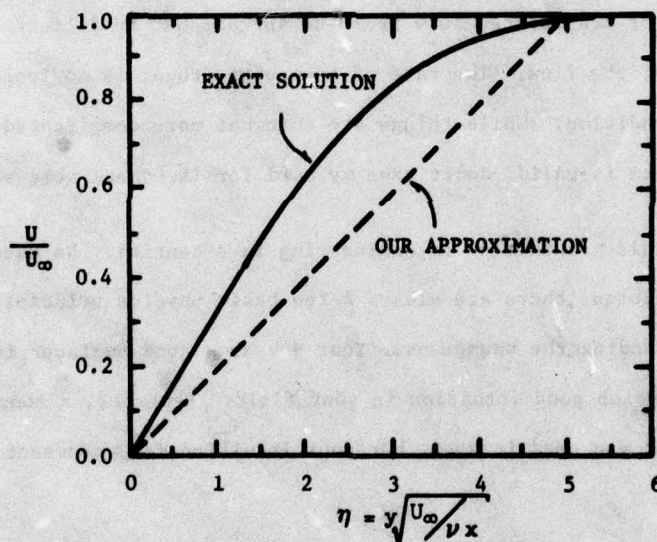
Figure 4. Blasius Solution of the Boundary Layer for Flow Over a Flat Plate

We see that our prediction of the functional form of δ as given by Eqn (10) and (11) is exactly correct. Since the equations are the same, our predictions of the effect of boundary layer thickness on velocity are also exactly correct. Note, also, that included in Figure 4 is our linear approximation to the velocity profile which does give a ball park feel for the shear stress. So, we find that all our predictions are exactly correct.

IV. Conclusions

We have, over the course of these few pages, built what I feel is a very good intuitive model of what is happening in a boundary layer. The important idea of disturbance transport is the foundation of this model and should be the key on which you continue to build your intuition.

I should also state that we have dealt here only with laminar boundary layers in which disturbances are propagated via molecular interactions. The ideas here, however, can be extended to turbulent boundary layers by simply realizing that our disturbance is still being propagated or transported away from the surface but by different mechanisms, i.e., the eddy motion of the flow. The rate of transport, then, is no longer simply a property of the flow condition. While things are somewhat more complicated, the same simple intuitive approach is valid; don't take my word for it, check some solutions.

My last remark is this : intuition in engineering is essential. No matter how complicated analysis becomes, there are always a few basic physics principles which hold the key to understanding the phenomena. Your job as a good engineer is to seek these principles and develop good intuition in your field. Remember, a computer will always let you down when you need it most, but your intuition is a constant reliable friend.

Acknowledgements

The author acknowledges the contributions from Dr. James Hitchcock, AFIT.

References

1. Vincenti, W. G., Kruger, C. H., Jr. Introduction to Physical Gas Dynamics. John Wiley and Sons, New York, 1967.

2. Tritton, D. J., Physical Fluid Dynamics, Van Nostrand Reinhold Company, New York, 1977.

3. Schlichting, J., Boundary Layer Theory, McGraw Hill, New York, 1960.

4. Blasius, H., Z. Math. Phys., Vol. 56, p. 1, 1908.

5. Holman, J. P., Heat Transfer, McGraw-Hill, New York, 1976.

FLOW FIELD CHARACTERIZATION OF FLOW DIRECTION AND MACH

NUMBER PROBES USING SLENDER BODY

THEORY

G. David Huffman[*]

Abstract

Slender body theory has been used to model the flow field past a flow direction and Mach number probe at an angle of attack and a sideslip angle. An expression has been derived for the body surface pressure coefficient. This has been converted into angular and static pressure coefficients which are evaluated for a specific sensor geometry. These expressions are employed in the quantification of misalignment effects. Finally, the velocity expressions are used to visualize the three-dimensional flow past a cone probe at an angle of attack and a sideslip angle.

I. Background

Flow fields encountered in engineering applications are often three-dimensional and, thus, have both a varying flow direction and velocity/Mach number. Turbomachine and aircraft environments are often harsh, necessitating a rugged, durable sensor. This requirement makes multi-ported pressure probes particularily attractive for these applications.

Pressure probes frequently consist of an aerodynamic body with a symmetrical arrangement of sensing holes. A number of different geometries have been investigated and some typical cases are reviewed in references 1 through 15. Probes are treated in more general terms in references 16 and 17.

Pressure probes are normally employed in either the stationary or nulling mode. In the nulling or equal pressure approach, the probe is oriented such that each of the side ports, see Figure 1, reads the same pressure. The probe position is noted and the flow direction determined. In the stationary mode, the probe is fixed and the top-to-bottom and side-to-side pressure differences measured. Calibration functions are then used to find the flow angles α and β. The static and total pressures and, thus, Mach number can be determined in a similar manner. Both these methods have merit; however, turbomachine and aircraft applications normally require an immovable sensor. As a consequence, only stationary probes will be considered.

Since the probes are to be used without rotation, the sensitivity to flow angularity is extremely important. While values of this parameter are available for a number of

---

[*]Distinguished Visiting Scientist, USAFA/DFAN; Professor, Purdue University, Indianapolis, IN
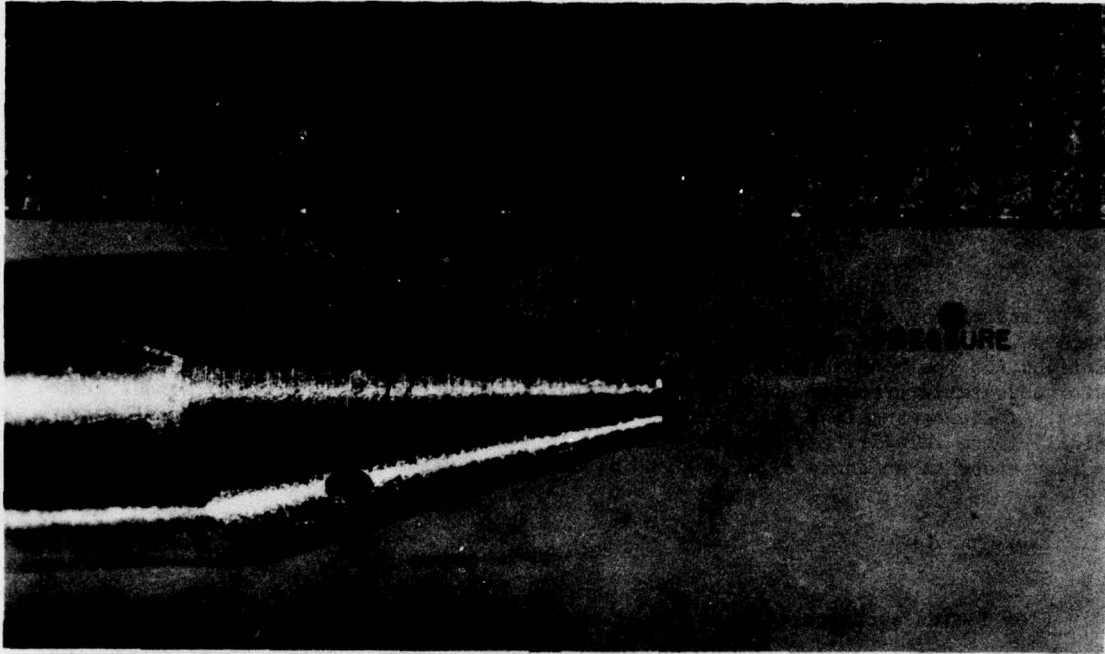
Figure 1.   Typical Flow-Direction Probe (Each Unit on Scale Represents 0.5 mm)

calibrated probes, this data is of limited value in synthesizing a sensor geometry for a specific application.   Therefore, a general analytic model has been developed using slender body theory and this is discussed in Section II.

In addition to the probe sensitivity which is largely dictated by aerodynamic considerations, alignment and manufacturing defects also influence the accuracy with which flow angles and static and total pressures can be determined.   Effects of this nature are discussed in Section III. The mathematical model is used to visualize the flow field in Section IV. The results of this investigation are summarized in Section V.

II. A Mathematical Model of Probe Aerodynamic Behavior

A. Introduction

The objective of an aerodynamic probe is to determine the magnitude and direction of the velocity vector. This translates into a measurement of pressures which—by means of calibration functions—are then converted into flow angles and total and static pressures. The flow field parameters should be accurately measured with the probe itself creating a minimal disturbance.

A typical flow-direction probe having an aerodynamic shape can be thought of as a slender body (the body radius is much less than the body length.) The use of slender body theory in the analysis of probes, thus, immediately comes to mind. There are, however, shortcomings associated with this approach, the major one being that the rate of change of body radius with respect to body length must be small. This feature precludes stagnation regions in a slender body approach.

Of course, a complete description of the flow field around an aerodynamic probe can be generated by numerically solving the three-dimensional potential flow equations, e.g., references 18 and 19. While this approach is more accurate than slender body theory under some conditions, it does not lend itself to synthesis of probe shapes. Furthermore, analytic calibration relations are not obtained, and considerable insight into the physical process is lost. Consequently, a slender body approach will be employed in the ensuing analysis.

B. Basic Formulation of Slender Body Theory

A slender body of revolution in a cross-flow is shown in Figure 2. The body itself can be described in terms of an axial, z, and radial, r, coordinate with r = R(z) on the body surface.
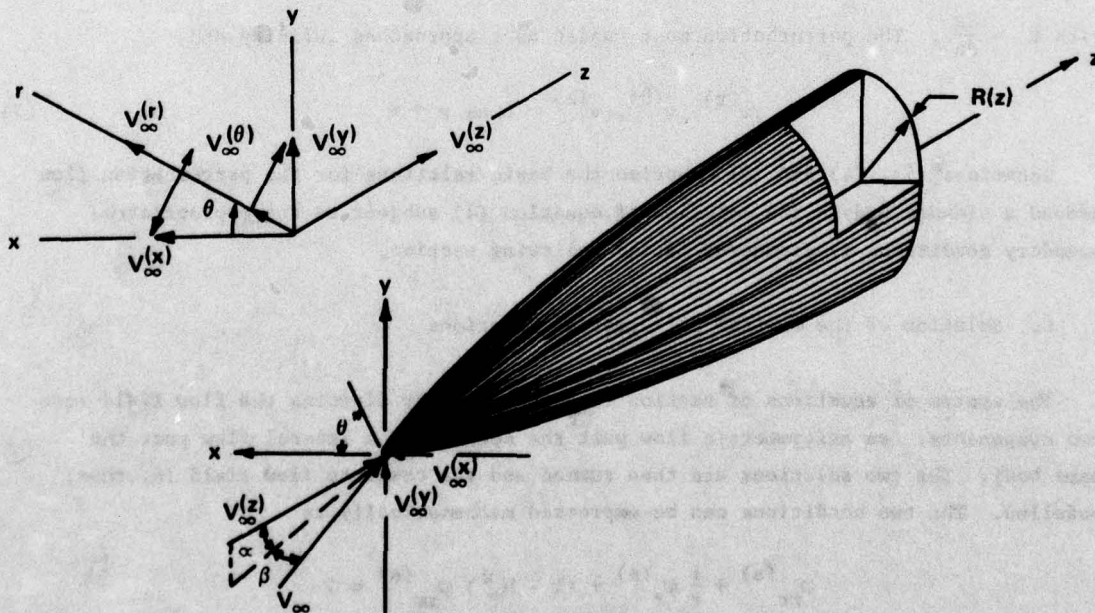

Figure 2. Slender Body of Revolution in a Cross-Flow

Following Shapiro, reference 20, and Liepmann and Roshko, reference 21, the perturbation
potential can be written as

$$\varphi_{rr} + \frac{1}{r} \varphi_r + \frac{1}{r^2} \varphi_{\theta\theta} + (1 - M_\infty^2) \varphi_{zz} = 0 \tag{1}$$

where the subscripts r, θ and z denote partial differentiation. Equation (1) is de-
rived by assuming that the potential function Φ can be written as the sum of the per-
turbation due to the body, φ, and the potential due to the external flow, V_∞. It is
further assumed that the perturbation velocities are much smaller than the free-stream
velocity. The perturbation velocities are related to the potentials via

$$\varphi_r = v^{(r)}, \quad \varphi_\theta = r\, v^{(\theta)}, \quad \varphi_z = v^{(z)} \tag{2}$$

The boundary condition on the body surface can be written as

$$\text{grad } \Phi \cdot \text{grad } F = 0 \text{ on } F(r, \theta, z) = 0 \tag{3}$$

where $F(r, \theta, z) = r - R(z)$ and $\text{grad } \Phi = \vec{V}_\infty + \text{grad } \varphi = \vec{V}_\infty + \vec{v}$.

Evaluation of equation (3) yields

$$\left[V_\infty^{(r)} + v^{(r)} \right] - \left[V_\infty^{(z)} + v^{(z)} \right] R' = 0 \text{ on } F(r, \theta, z) = 0 \tag{4}$$

with $R' = \dfrac{dR}{dz}$. The perturbation must vanish as r approaches infinity and

$$v^{(r)}, \; v^{(\theta)}, \; v^{(z)} \to 0 \text{ as } r \to \infty \tag{5}$$

Equations (1), (4) and (5) comprise the basic relations for the perturbation flow
around a slender body. The solution of equation (1), subject to the appropriate
boundary conditions, is discussed in the following section.

C. Solution of the Partial Differential Equations

The system of equations of Section II.B is solved by dividing the flow field into
two components: an axisymmetric flow past the sensor and a lateral flow past the
same body. The two solutions are then summed and the complete flow field is, thus,
modelled. The two conditions can be expressed mathematically as

$$\varphi_{rr}^{(a)} + \frac{1}{r} \varphi_r^{(a)} + (1 - M_\infty^2) \varphi_{zz}^{(a)} = 0$$

$$\varphi_r^{(a)} = V_\infty^{(z)} R' \text{ on } F(r, \theta, z) = 0 \tag{6}$$

$$\varphi_r^{(a)}, \; \varphi_z^{(a)} \to 0 \text{ as } r \to \infty$$

42

and

$$\varphi_{rr}^{(\ell)} + \frac{1}{r}\varphi_r^{(\ell)} + \frac{1}{r^2}\varphi_{\theta\theta}^{(\ell)} + (1 - M_\infty^2)\varphi_{zz}^{(\ell)} = 0$$

$$\varphi_r^{(\ell)} = -V_\infty^{(r)} \quad \text{on } F(r,\theta,z) = 0 \tag{7}$$

$$\varphi_r^{(\ell)}, \; r\,\varphi_\theta^{(\ell)}, \; \varphi_z^{(\ell)} \to 0 \quad r \to \infty$$

where the superscript a denotes the axisymmetric and ℓ the lateral component. It then follows that $\varphi = \varphi^{(a)} + \varphi^{(\ell)}$.

Equation (6) can be written in terms of a source distribution, $q(z)$, following Sears, reference 22, as

$$\varphi^{(a)} = -\tfrac{1}{4}\pi \int_0^\ell q\,(\zeta)\; \frac{d\zeta}{\sqrt{(z-\zeta)^2 + \delta^2\,r^2}} \tag{8}$$

where $\delta = \sqrt{1 - M_\infty^2}$. The velocity components are then given as

$$v^{(z)} = \varphi_z^{(a)} = -\frac{1}{4\pi\delta} \int_0^\ell \frac{(z-\zeta)\,q\,(\zeta)\,d\zeta}{[(z-\zeta)^2 + \delta^2\,r^2]^{3/2}} \tag{9}$$

and

$$v^{(r)} = \varphi_r^{(a)} = \frac{\delta r}{4\pi} \int_0^\ell \frac{q(\zeta)\,d\zeta}{[(z-\zeta)^2 + \delta^2\,r^2]^{3/2}} \tag{10}$$

At this point the source distribution function is unspecified. In essence, the specification of q produces an arbitrary body. Since the body is generally known, a direct determination of $q\,(\zeta)$ in terms of $R\,(z)$ is required. An approximate solution of this type can be obtained by writing

$$q(\zeta) = q(z + \delta\,r\,\eta) = \sum_{n=0}^\infty \frac{(\delta r\eta)^n}{n!}\,q^{(n)}\,(z) \tag{11}$$

where $q^{(n)}\,(z)$ denotes the n-th derivative with respect to z. Substitution of equation (11) into equations (9) and (10) and term-by-term integration yields

$$\varphi_z^{(a)} = -\frac{1}{4\pi\delta}\left\{ \frac{q(z)}{z}\left[\frac{1 - 2\frac{z}{\ell}}{1 - \frac{z}{\ell}}\right] + q^1(z)\left[\ell n\frac{4z(\ell - z)}{\delta\,r} - z\right] + \dots \right\} \tag{12}$$

$$\varphi_r^{(a)} = \frac{1}{4\pi} \left| \frac{2\, q(z)}{\delta\, r} \right|$$

for terms of order less than βr with $\delta r << \ell - z$. Application of the boundary conditions on the body show that

$$q(z) = \delta\, V_\infty^{(z)}\, S'$$

where S denotes the body cross-sectional area, $\pi[R(z)]^2$.

The lateral potential function can be determined in a similar manner by noting that if $\varphi\, (r, z)$ is a solution of equation (6), then both $\sin\theta\, \varphi_r$ and $\cos\theta\, \varphi_r$ are solutions of equation (7). Again using a series expansion for the source distribution, term-by-term integration and application of the boundary conditions yields

$$\varphi_r^{(\ell)} = \frac{V_\infty^{(x)} \cos\theta + V_\infty^{(y)} \sin\theta}{\pi} \left(\frac{-S}{r^2} \right) \tag{15}$$

$$\varphi_\theta^{(\ell)} = \frac{V_\infty^{(y)} \cos\theta - V_\infty^{(x)} \sin\theta}{\pi} \left(\frac{S}{r} \right) \tag{16}$$

$$\varphi_z^{(\ell)} = \frac{V_\infty^{(x)} \cos\theta + V_\infty^{(y)} \sin\theta}{\pi} \left(\frac{S'}{r} \right) \tag{17}$$

The potential functions can be combined and the velocity components and pressure coefficient determined.

D. The Velocity Components and Pressure Coefficient

Equations (12) and (17) and (13) and (15) can be combined to yield the perturbation velocities and

$$\frac{v^{(r)}}{V_\infty} = \tfrac{1}{2} \cos\alpha \cos\beta \left(\frac{R^2}{r} \right) - (\sin\beta \cos\theta + \sin\alpha \cos\beta \sin\theta)\frac{R^2}{r} \tag{18}$$

$$\frac{v^{(\theta)}}{V_\infty} = (\sin\alpha \cos\beta \cos\theta - \sin\beta \sin\theta) \frac{R^2}{r^2} \tag{19}$$

$$\frac{v^{(z)}}{V_\infty} = \tfrac{1}{2} \cos\alpha \cos\beta\, f + (\sin\beta \cos\theta + \sin\alpha \cos\beta \sin\theta) \left(\frac{R^2}{r} \right)' \tag{20}$$

where f denotes the body-geometry function and is

$$f = -\tfrac{1}{2} (R^2)' \left(\frac{1}{\sqrt{z^2 + \delta^2 r^2}} - \frac{1}{\sqrt{(\ell-z)^2 + \delta^2 r^2}} \right) + \tfrac{1}{2} (R^2)'' \left[\frac{\ell-z}{\sqrt{(\ell-z)^2 + \delta^2 r^2}} + \right.$$

$$\frac{z}{\sqrt{z^2 + \delta^2 r^2}} + \ell n \left(\frac{-z + \sqrt{z^2 + \delta^2 r^2}}{\ell-z + \sqrt{(\ell-z)^2 + \delta^2 r^2}} \right) \right] - \tfrac{1}{4} (R^2)''' \left(\frac{z^2}{\sqrt{z^2 + \delta^2 r^2}} - \right.$$

$$\frac{(\ell-z)^2}{\sqrt{(\ell-z)^2 + \delta^2 r^2}} + 2 \sqrt{(\ell-z)^2 + \delta^2 r^2} - 2 \sqrt{z^2 + \delta^2 r^2} \right) + \dots \qquad (21)$$

Equation (21) is not subject to the constraint that $\delta r << \ell-z$.

In probe analysis, the pressure coefficient is of major importance. The pressure itself can be related to the velocity by means of

$$p = p_\infty - \tfrac{1}{2} \rho V_\infty^2 \left(2 \frac{\vec{V}_\infty \cdot \vec{v}}{V_\infty^2} + \frac{v^2}{V_\infty^2} \right) \qquad (22)$$

where $\vec{v}$ is evaluated on the body surface. The pressure coefficient is defined as

$$C_p = \frac{p - p_\infty}{\tfrac{1}{2} \rho V_\infty^2} = -2 \frac{\vec{V}_\infty \cdot \vec{v}}{V_\infty^2} - \frac{v^2}{V_\infty^2} \qquad (23)$$

This can be written as

$$C_p = \cos^2 \alpha \, \cos^2 \beta \, [\, -f - (R')^2 \,] + \sin^2 \beta \, [\, 1 - 4 \sin^2 \theta \,] +$$

$$\sin^2 \alpha \, \cos^2 \beta \, [\, 1 - 4 \cos^2 \theta \,] + \cos \alpha \, \sin 2\beta \, [\, -2 R' \cos \theta \,] +$$

$$\sin 2 \alpha \, \cos^2 \beta \, [\, -2 R' \sin \theta \,] + \sin 2 \alpha \, \cos \beta \, [\, 4 \sin \theta \cos \theta \,] \qquad (24)$$

where f is to be evaluated on the body surface, i.e., $r = R$. Equation (24) represents the major result of the analysis and can be used to determine probe angular and static pressure sensitivity for arbitrary geometries.

III. Aerodynamic Probe Angular and Static Pressure Sensitivity

A. Differential and Averaged Pressure Coefficients

The flow angularity is determined by differencing the measured pressures between the side and top and bottom ports, see Figure 1, for instance. Since these ports are at the same z and R locations, the pressure difference is generated by subtracting C_p values at different θ locations and

$$\Delta C_p = - 4 \sin^2 \beta \, (\sin^2 \theta_1) - 4 \sin^2 \alpha \cos^2 \beta \, (\cos^2 \theta_2 \cos^2 \theta_1) -$$

$$2 R' \cos \alpha \sin 2 \beta \, (\cos \theta_2 - \cos \theta_1) - 2 R' \sin 2 \alpha \cos^2 \beta \, (\sin \theta_2 - \sin \theta_1) +$$

$$4 \sin 2 \alpha \cos \beta \, (\sin \theta_2 \cos \theta_2 - \sin \theta_1 \cos \theta_1) \tag{25}$$

The sensitivity to changes in flow angle is defined as $\partial \Delta C_p / \partial \alpha$ or $\partial \Delta C_p / \partial \beta$. The former can be written as

$$\frac{\partial \Delta C_p}{\partial \alpha} = 8 R' \cos 2 \alpha \cos^2 \beta \tag{26}$$

where θ_1 and θ_2 have been taken as 90 and 270° respectively. Note that the sensitivity to flow direction in one plane depends to some extent on the flow angle in the other direction.

Equation (26) is plotted in Figure 3. It is quite apparent from the figure that the probe angular sensitivity — regardless of shape — depends on α and β. Approximately a 10% reduction in sensitivity occurs for α and β values of 10°. Note that $\partial \Delta C_p / \partial \alpha$ is the same for both positive and negative values of α and β.

The averaged pressure coefficient can be used to determine the flow-field static pressure, P_∞. C_p is evaluated at a number of theta values, the results summed and divided by the number of theta values. Mathematically this process yields

$$< Cp > = \cos^2 \alpha \cos^2 \beta \, [-f - (R')^2] + \sin^2 \beta \, (1 - \sum_{i=1}^{4} \sin^2 \theta_1) + \sin \alpha \cos^2 \beta \, (1 -$$

$$\sum_{i=1}^{4} \cos^2 \theta_1) - \tfrac{1}{2} R' \cos \alpha \sin 2 \beta \sum_{i=1}^{4} \cos \theta_1 - \tfrac{1}{2} R' \sin 2 \alpha \cos^2 \beta \sum_{i=1}^{4} \sin \theta_1 +$$

$$\sin 2 \alpha \cos \beta \sum_{i=1}^{4} \sin \theta_1 \cos \theta_1 \tag{27}$$

With θ_1 as 0, 90°, 180° and 270°, equation (27) becomes
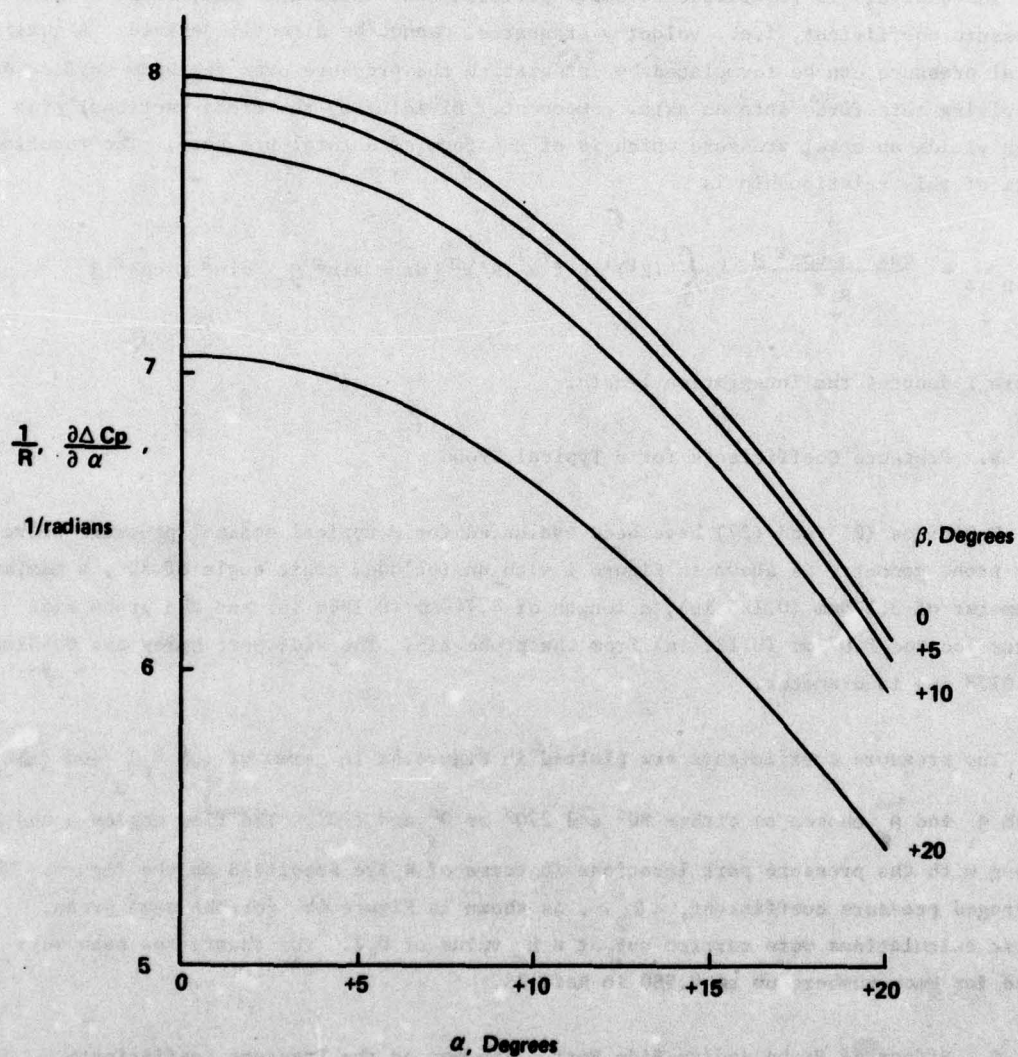
Figure 3. Probe Angular Sensitivity as a Function of α and β

$$<C_p> = \cos^2\alpha \cos^2\beta \left[-f - (R')^2 \right] - \sin^2\alpha \cos^2\beta \tag{28}$$

which is approximately parabolic with respect to α and β.

The analysis is restricted to small perturbations velocities and, thus, a total pressure coefficient, i.e., velocity stagnated, cannot be directly derived. A quasi-total pressure can be formulated by integrating the pressure over the body surface and resolving this force into an axial component. Dividing by the cross-sectional area then yields an axial pressure which is of the form of a total pressure. The functional form of this relationship is

$$<C_p>_z = \frac{\cos^2\alpha \cos^2\beta}{R_\ell^2} \int_0^\ell (R^2)' \left[-f - (R')^2 \right] dz - \sin^2\beta - \sin^2\alpha \cos^2\beta \tag{29}$$

where ℓ denotes the integration length.

B. Pressure Coefficients for a Typical Probe

Equations (25) and (27) have been evaluated for a typical conical pressure probe. The probe geometry is shown in Figure 1 with an included conic angle of 30°, a maximum diameter of 3.175mm (0.125 in), a length of 4.740mm (0.1866 in) and the probe side ports located 3.073mm (0.121 in) from the probe tip. The side port holes are 0.452mm (0.0178 in) in diameter.

The pressure coefficients are plotted in Figure 4a in terms of $(\Delta C_p)_\alpha$ and $(\Delta C_p)_\beta$, with θ_1 and θ_2 chosen as either 90° and 270° or 0° and 180°. The flow angles α and β, along with the pressure port locations in terms of θ, are specified on the figure. The averaged pressure coefficient, $<C_p>$, is shown in Figure 4b for the same probe. These calculations were carried out at a M_∞ value of 0.2. The theory has been verified for Mach numbers up to 0.980 in Ref. 23.

C. Effect of Probe and/or Side Port Alignment on the Pressure Coefficients

The influence of probe and/or side part alignment on the angular and averaged pressure coefficients can be calculated from equations (25) and (27). The port locations denoted by θ can be rotated relative to the design locations of 0°, 90°, 180° and 270°, and the resulting coefficients calculated. Coefficients generated in this manner are plotted in Figures 5 and 6. Note that the cone of Section III.B has been used in these calculations.
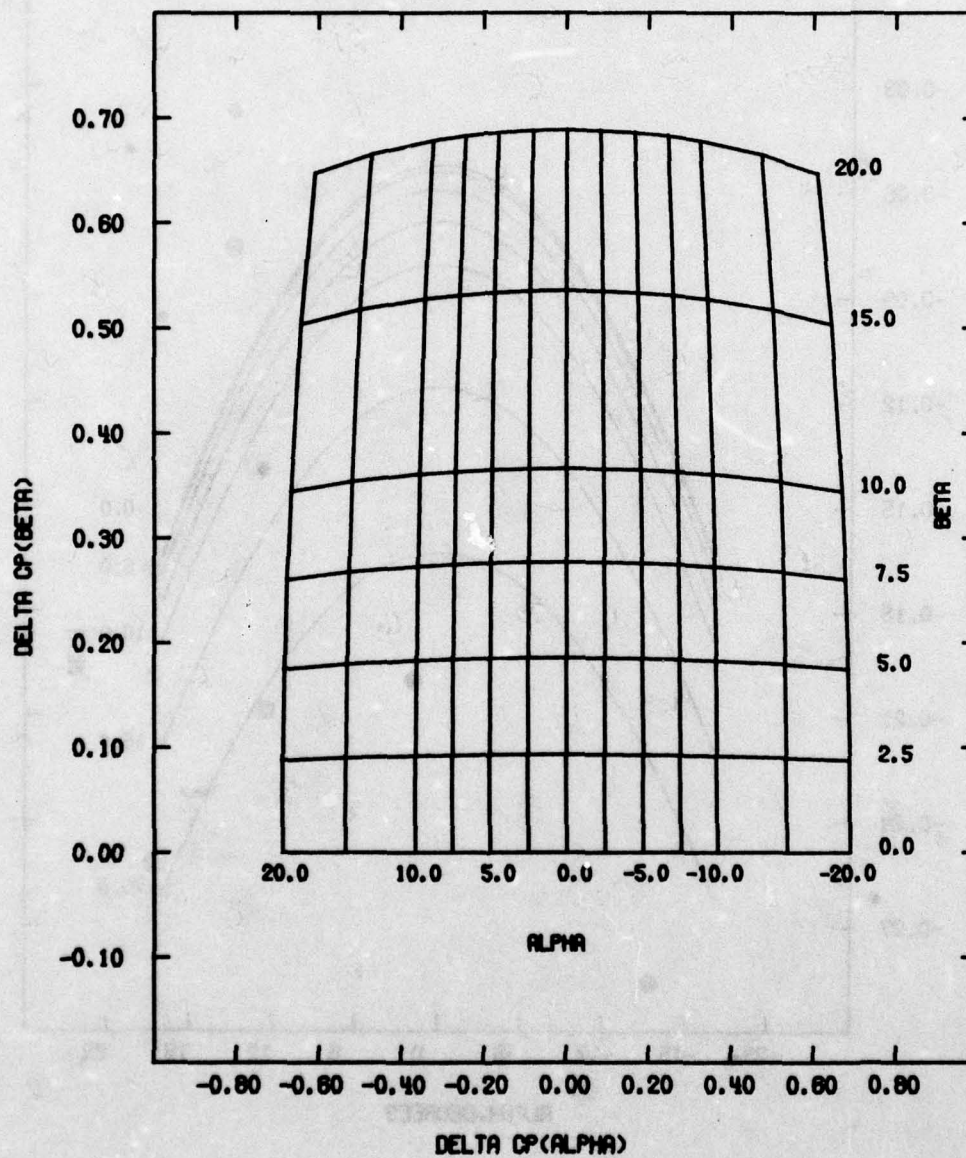
Figure 4a. $(\Delta C_p)_\alpha$ Versus $(\Delta C_p)_\beta$ for a Typical Flow Direction Probe ($\theta_1 = 0^\circ$, 90°, 180°, and 270°)

Figure 4b. $\langle C_{p_o} \rangle$ Versus α and β for a Typical Flow Direction Probe ($\theta_i = 0°$, $90°$, $180°$, and $270°$)

Figure 5a. $(\Delta C_p)_\alpha$ Versus $(\Delta C_p)_\beta$ for a Typical Flow Direction Probe ($\theta_1 = 2.5^\circ$, 92.5°, 182.5° and 272.5°)

Figure 5b. $\langle C_p \rangle$ Versus α and β for a Typical Flow Direction Probe (θ_1 = 2.5°, 92.5°, 182.5° and 272.5°)

Figure 6a. $(\Delta C_p)_\alpha$ Versus $(\Delta C_p)_\beta$ for a Typical Flow Direction Probe ($\theta_1 = 2.5^o$, 90°, 180° and 270°)
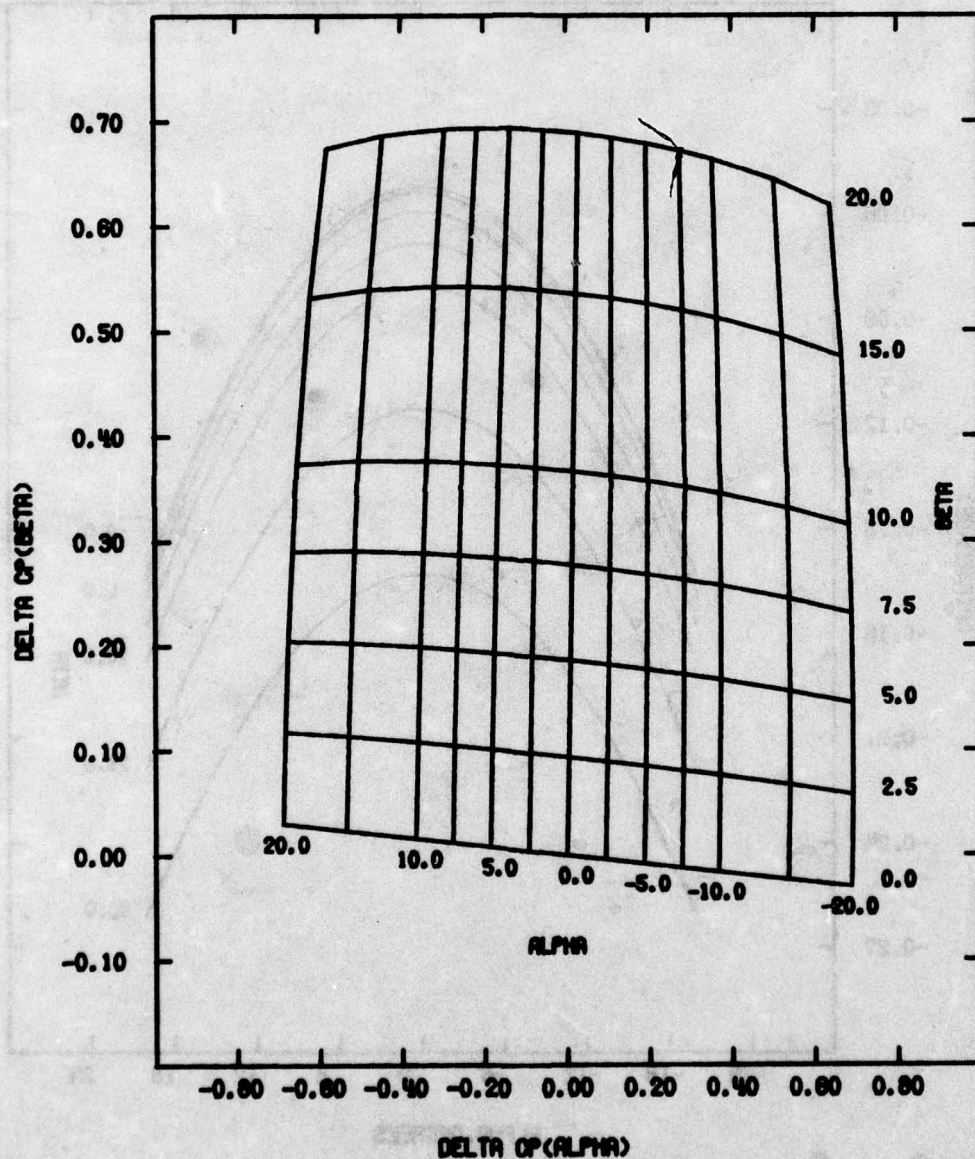
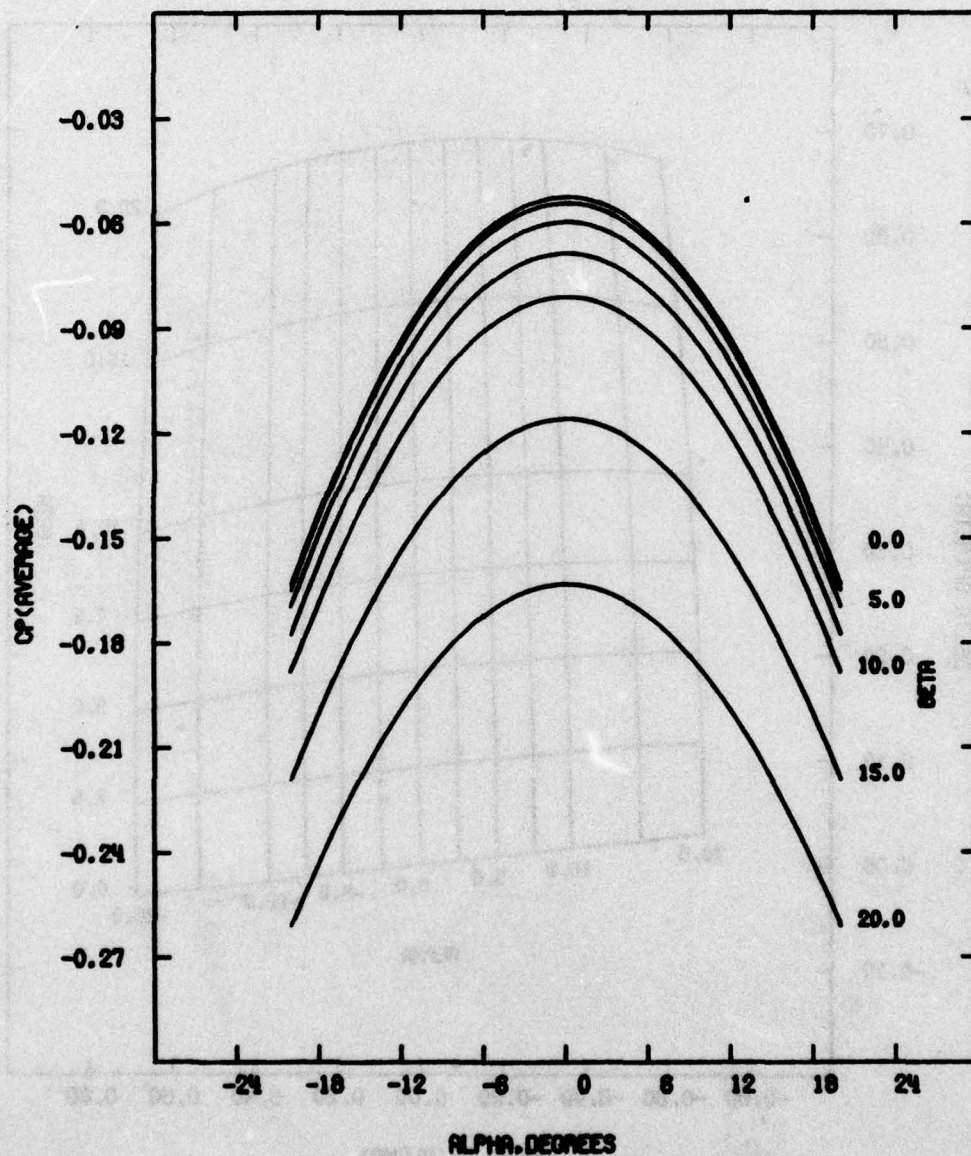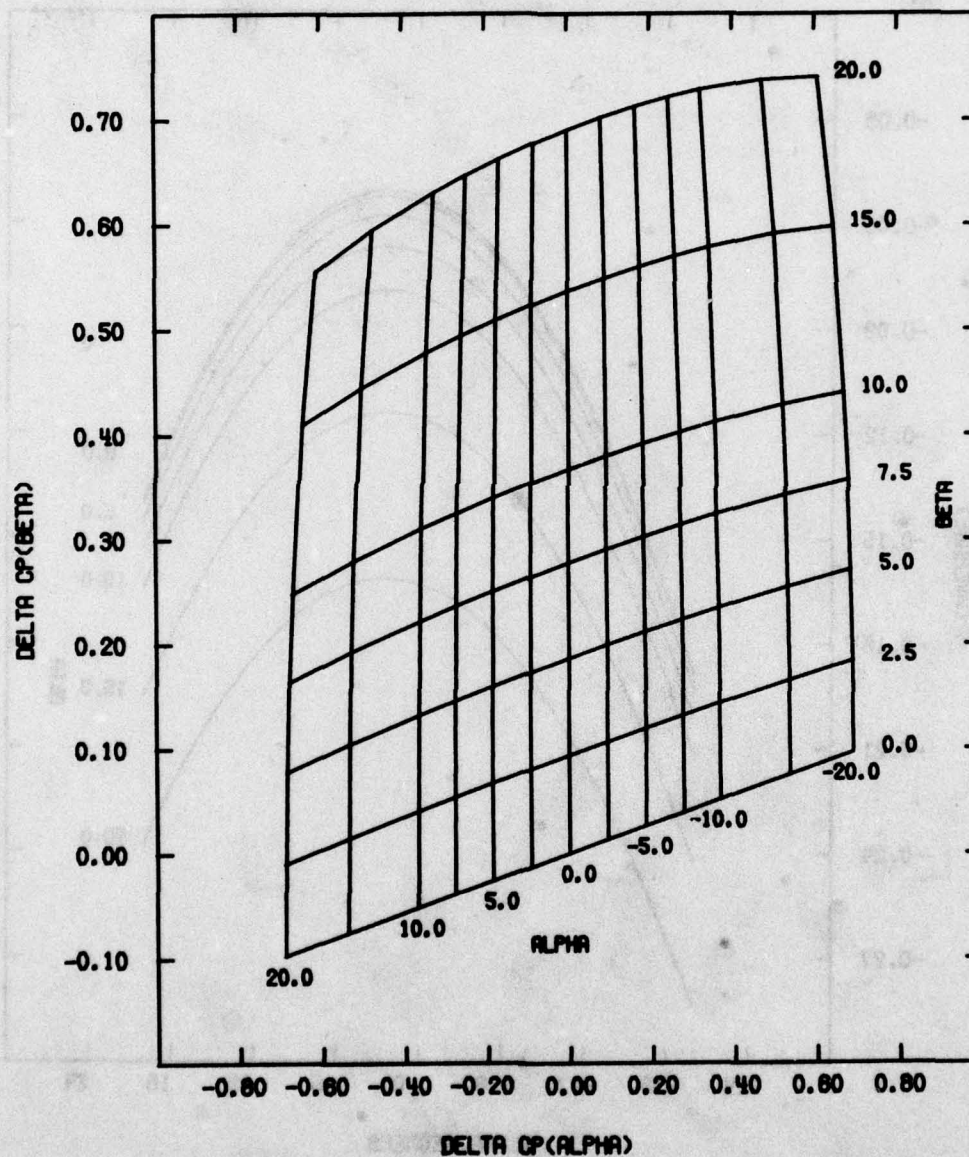Figure 6b. $\langle C_p \rangle$ Versus α and β for a Typical Flow Direction Probe ($\theta_1 = 2.5^{\circ}$, 90°, 180° and 270°)

Misalignments are of two types. The first consists of a rotation of the probe body itself relative to a fixed or pre-determined coordinate system. This could occur in a turbomachine application during installation of the sensor. In this case all θ values are displaced by the same amount. The angular and averaged coefficients are plotted in Figure 5 for a port displacement of 2.5°. Note that $(\Delta C_p)_\alpha$ and $(\Delta C_p)_\beta$ are strongly influenced by the rotation but $\langle C_p \rangle$ is unchanged.

The second misalignment consists of a manufacturing defect with only one port displaced. This case is plotted in Figure 6 for one side port located at 2.5° rather than 0. Now both the angular and averaged pressure coefficients are influenced.

IV. Flow Field Visualization Using Slender Body Theory

The flow field past a slender body at both an angle of attack and sideslip angle can be visualized by generating a series of particle trajectories. The velocity components can be integrated yielding the instantaneous particle position, i.e.,

$$r = r_0 + \int_0^t v^{(r)}\, dt \qquad\qquad \theta = \theta_0 + \int_0^t \frac{v}{r}^{(\theta)}\, dt \qquad\qquad (30)$$

$$z = z_0 + \int_0^t v^{(z)}\, dt$$

where $v^{(r)} = v_\infty^{(r)} + v^{(r)}$, etc. The flow field past the cone probe of section III.B at α and β values of 7° and 11° is shown in Figure 7.

V. Summary

Slender body theory has been used to model the flow field past an arbitrary body of revolution at a sideslip angle and angle of attack. Expressions for the pressure coefficient on the sensor surface have been derived. From these relations, angular and averaged (static) pressure coefficients have been determined. Expression for the angular probe sensitivity have also been evaluated. Finally, the effects of probe and probe side port misalignments have been quantified for a given sensor geometry.
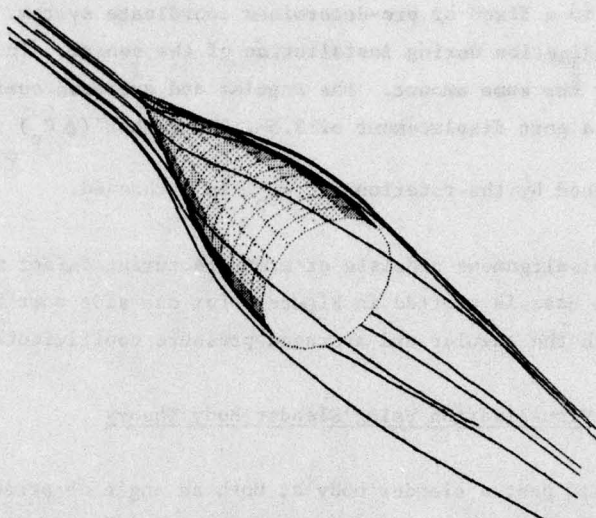
Figure 7a. Flow Field Past a 30° Cone Probe at $\alpha = \beta = 7°$
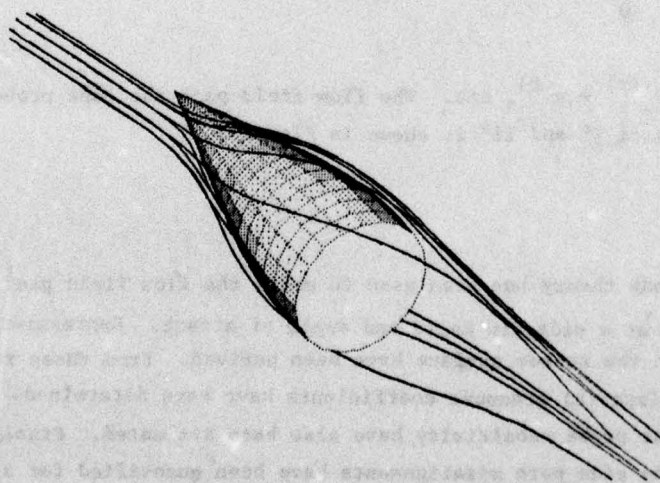
Figure 7b. Flow Field Past a 30° Cone Probe at $\alpha = \beta = 11°$

Symbols

C_p	Pressure Coefficient
ΔC_p	Angular Pressure Coefficient
$< C_p >$	Averaged Pressure Coefficient
f	Body Geometry Function
ℓ	length
M_∞	Free-stream Mach Number
p	Pressure
q	Source Distribution per Unit Length
r, θ, z	Cylindrical Coordinates
R	Body Radius
S	Body Cross-Sectional Area
v	Perturbation Velocity
V	Velocity
x, y, z	Cartesian Coordinates
α	Angle of Attack
β	Sideslip Angle
δ	$\sqrt{1 - M_\infty^2}$
ρ	Density
φ	Perturbation Potential
Φ	Potential Function

Subscripts

r, θ, z	Partial Differentiation with Respect to the Cylindrical Coordinates
o	Initial Condition
∞	Free-stream

Superscripts

a	Axial
ℓ	Transverse or lateral
r, θ, z	Cylindrical Coordinates
x, y, z	Cartesian Coordinates

References

1. Schultz, W. M. et al., <u>Several Combination Probes for Surveying Static and Total Pressure and Flow Direction</u>, NACA TN 2830, 1952.

2. Kettle, D. J., "Design and Calibration at Low Speeds of a Static Tube and Pitot-Static Tube with Semi-Ellipsoidal Nose Shapes," <u>J. Ray. Aer. Soc.</u>, <u>Vol. 58</u>, p. 835, 1954.

3. Smetena, F. O. and Stuart, J. W. M., <u>A Study of Angle-of-Attracks Angle-of-Sideslip Pitot-Static-Probes</u>, WADC TR 5723A, AD 118209, 1957.

4. Bryer, O. W. et.al., "Pressure Probes Selected for Three-Dimensional Flow Measurement," <u>Rep. Mem. Aero Res. Coun. London</u>, No. 3037, 1958.

5. Morrison, D. F. et. al., "Hole Size Effect on Hemisphere Pressure Distributions," <u>J. Roy. Aer. Soc.</u>, Vol 71, 1967.

6. Wright, M. A., "The Evaluation of a Simplified Form of Presentation for Spherical and Hemispherical Pitometer Calibration Data," <u>J. Sci. Instr (J. Phys. E)</u>, <u>Vol. 3</u>, p. 356, 1970.

7. Schaub, V. W. et. al., <u>An Investigation of the Three-Dimensional Flow Characteristics of a Non-Nulling Five-Tube Probe</u>, Nat. Res. Council of Canada, Aero Rpt. LR-393, NRC No. 7964, 1964.

8. Dudzinski, J. T. and Krause, L. N., <u>Flow Direction Measurement with Fixed-Position Probes</u>, NASA TMX-1904, 1969.

9. Beecham, L. J. and Collins, S. J., <u>Static and Dynamic Response of a Design of a Differential Pressure Yawmeter at Supersonic Speeds</u>, Roy. Aer. Est. Report No. GW 19, 1954.

10. Hutton, P. G., <u>Static Response of a Hemispherical-Headed Yawmeter at High Subsonic and Transonic Speeds</u>, Roy. Aer. Est. Tech. Note N. Aero 7525, CP No. 401, 1957.

11. Nowack, C.F.R., "Improved Calibration Method for a Five-Hole Spherical Pitot Probe," <u>J. Sci. Instr.</u>(J. Phys. E.), <u>Vol. 3</u>, p. 21, 1970.

12. Dau, K., et.al., "The Probes for the Measurement of the Complete Velocity Vector in Subsonic Flow," <u>Aero. J.</u>, <u>Vol. 72</u>, p. 1066, 1968.

13. Spaid, F. W. et. al., "Miniature Probe for Transonic Flow Direction Measurements," <u>AIAA J.</u>, <u>Vol. 13</u>, p. 253, 1975.

14. Glawe, G. F., et. al., <u>A Small Combination Sensing Probe for Measurement of Temperature, Pressure and Flow Direction</u>; NASA TN D-4816, 1968.

15. Treaster, A. L. and Yocum, A. M., <u>The Calibration and Application of Five-Hole Probes</u>," Penn. State Univ. Applied Research Laboratory Report TM 78-W, 1978.

16. Bryer, D. W. and Pankhurst, D. W., <u>Pressure Probe Methods for Determining Wind Speed and Flow Direction</u>, Published by Her Majesty's Stationary Office, London England, 1971.

17. Wuest, W., "Measurement of Flow Speed and Flow Direction by Aerodynamic Probes and Vanes," Paper Presented at the 30th Flight Mechanics Panel Meeting in Montreal, Canada, 1967.

18. Hess, J. L. and Smith, A.M.O., "Calculation of Potential Flow about Arbitrary Bodies," _Progress in Aeronautical Sciences_, Vol. 8, Pergammon Press, p. 81, 1966.

19. Smith, A.M.O. and Bauer, A.B., "Static-Pressure Probes that are Theoretically Insensitive to Pitch, Yaw and Mach Number," _J. Fl. Mech._, _Vol. 44_, p. 513, 1970.

20. Shapiro, A. H., _The Dynamics and Thermodynamics of Compressible Fluid Flow_, _Volume I_, The Ronald Press, New York, 1953.

21. Liepmann, H. W. and Roshko, A. _Elements of Gas Dynamics_, John Wile & Sons, New York, 1958.

22. Sears, W. R., "Small Perturbation Theory," in _General Theory of High Speed Aerodynamics_, Princeton University Press, Princeton N.J. P. 61, 1954.

23. Huffman, G. David et.al., "_Determination of Mach Number and Flow Direction with Pressure Probes_," AFAPL TR, in preparation.

WAVE DRAG PREDICTIONS ON SLENDER BODIES OF
REVOLUTION USING THE SUPERSONIC AREA RULE

Glen R. Schlotterbeck[*]

Abstract

This report discusses the mechanics and results of a computer program designed to
compute the wave drag of slender bodies of revolution in supersonic flow. The program is
based on the supersonic area rule and is intended for use as a tool in the first cut of
the design process. Hopefully, the program will indicate the most advantageous arrange-
ment of vehicle components for a minimization of wave drag over a range of Mach numbers.

I. Introduction

A. Background

Von Karman, in working with source distributions, first made the observation that the

wave drag integral was analogous to the classical, incompressible equation for the induced

drag of a lifting wing of length ℓ (Ref. 1). Specifically, von Karman noted that

$$D_w = \frac{-\rho}{4\pi} \int_o^\ell \int_o^\ell dx \, d\zeta \, f'(x) \, f'(\zeta) \, \log \left| x - \zeta \right| \tag{1}$$

where $f(x)$ was the intensity of the source distribution and ρ was the density of air.

If the function $f(x)$ were changed to denote the spanwise circulation distribution on a

loaded line, the induced drag would be given by

$$D_i = \frac{-\rho}{4\pi} \int_o^\ell \int_o^\ell dx \, d\zeta \, f'(x) \, f'(\zeta) \, \log \left| x - \zeta \right| \tag{2}$$

which is identical to the wave drag equation.

Based on this observation and slender body theory, Whitcomb developed what is now

known as the "area rule" (Ref. 2). Using stream tube observations and choking character-

istics, Whitcomb realized that three-dimensional flow fields within each individual

stream tube must obey one-dimensional flow laws. His "area rule," good in the transonic

---

[*]2nd Lt., USAF, Research Assistant, DFAN

region, stated that a slender body contained within a flow near the speed of sound had the same drag as a body of revolution with the identical cross-sectional areas of planes cut normal to the longitudinal axis.

Using the relationship between three-dimensional flow and one-dimensional flow, along with supersonic influence characteristics, Jones expanded upon Whitcomb's earlier work to include the supersonic regime (Ref. 3). His expansion was based on the idea that the three-dimensional disturbance field could be modeled by the superposition of one-dimensional disturbances taking the form of plane waves. Instead of using cross-sectional areas cut by planes normal to the longitudinal axis, Jones' method used areas formed by planes inclined at the Mach angle, called "Mach planes" (see Figure 1).
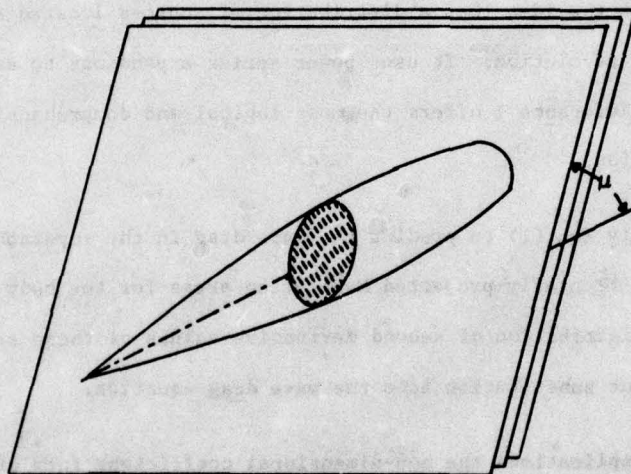
Figure 1. Mach Plane Areas (Ref. 4)

Experimental observation led Nelson and Welsh to conclude that greater accuracy could be obtained by using the frontal projection of these obliquely cut Mach plane areas rather than the actual cut areas (Ref. 5).

Thus, by redefining the area distribution necessary for the von Karman wave drag equation, the area rule, previously valid only in the transonic region, was expanded to include the supersonic regime.

B. Scope

This report describes a program which uses the von Karman formula coupled with the Mach plane area distribution concept advanced by Jones, together with the frontal projection technique developed by Nelson and Welsh, to compute the wave drag of a given slender body of revolution. The program's approach is to 1) calculate the frontal projection of the areas formed by Mach plane cuts at regular intervals along the body axis for a given Mach number, 2) calculate the second derivative of this area distribution, and 3) compute the wave drag coefficient based on the wave drag formula presented by von Karman.

II. Theory

Based on slender body and linear theory, the formulation of von Karman's wave drag equation begins with the idea that a distribution of sources located along an axial line describes a body of revolution. It uses power series expansions to arrive at the form given in Eqn (1). Reference 1 offers the most logical and comprehensive development of the wave drag equation.

In order to apply Eqn (1) to predict the wave drag in the supersonic region, the distribution of the frontally projected Mach plane areas for the body must be calculated. The corresponding distribution of second derivative values of these areas must then be determined for direct substitution into the wave drag equation.

For practical applications the non-dimensional coefficient form of the wave drag equation is most often used. However, as presented by von Karman, Eqn (1), transformed into coefficient form, is still not non-dimensionalized. Specifically, units of length remain in the argument of the logarithm term. To non-dimensionalize this term, therefore, both x and ζ need to be divided by a length value, namely, the total length of the body (Ref. 6). This transforms Eqn (1) into the truly non-dimensional coefficient form of the wave drag equation, given by

$$C_{D_w} = \frac{-1}{2\pi \, S_{Ref}} \int_o^L \int_o^L \frac{d^2 S}{dx^2} \frac{d^2 S}{d\zeta^2} \, \ell n \left| \frac{x}{L} - \frac{\zeta}{L} \right| dx \, d\zeta \tag{3}$$

where S_{Ref} is normally taken as the maximum cross-sectional area of the body. Eqn (3) appears to be the only working form of the wave drag equation in truly non-dimensional terms and has not been found in any other presentation of the formula.

Numerical integration of Eqn (3) is the logical solution approach due to the finite number of second derivative values calculated. However, in the region where ζ approaches x the value of the natural logarithm term goes to infinity and is actually undefined where ζ equals x . This necessitated the use of analytical methods employing a limiting technique in the region where ζ and x were one unit apart (Ref. 7). For this reason, Eqn (3) was separated into three regions, two of which were numerically evaluated and the third region, where ζ approaches x , which was analytically evaluated. Eqn (4) gives this expanded form of the wave drag equation in coefficient form as used in this computer program

$$C_{D_w} = \frac{-1}{2\pi \, S_{Ref}} \sum_{i=1}^{100} S_i'' \, \Delta x_i \left\{ \sum_{j=1}^{i-1} S_j'' \, \ell n \left| \frac{x_i}{L} - \frac{\zeta_i}{L} \right| \Delta \zeta_j \right.$$

$$+ \, S_i''(2)(L) \left| \left(\frac{x_i}{L} - \frac{\zeta_{i-1}}{L} \right) \ell n \left(\frac{x_i}{L} - \frac{\zeta_{i-1}}{L} \right) - \left(\frac{x_i}{L} - \frac{\zeta_{i-1}}{L} \right) \right| \tag{4}$$

$$\left. + \sum_{i+1}^{100} S_j'' \, \ell n \left| \frac{x_i}{L} - \frac{\zeta_i}{L} \right| \Delta \zeta_j \right\}$$

III. Discussion

The program divides the calculation of the wave drag coefficient into three logical phases. The first phase deals with the generation of a frontally projected Mach plane area distribution describing the body in question. A maximum of one hundred axial locations were investigated with respect to Mach plane/body intersection although more could be added if required. One hundred eighty radial distances, from body axis to Mach plane/body surface intersection, were calculated in order to describe the Mach plane area (see Figure 2).
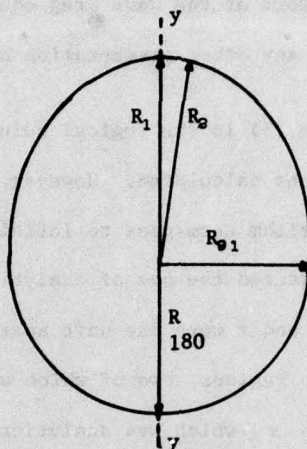
Figure 2. Radial Distances of Mach Plane Area

The bodies investigated to date have been tapered and since the Mach planes are inclined, the Mach plane areas were egg shaped rather than circular. This required the calculation of more than one radius value for Mach plane area sizing. Due to symmetry about the Y-Y axis, as seen in Figure 2, 180 radius values, corresponding to 180 degrees revolution about the body axis, adequately described each Mach plane area. From the radius values obtained, the program calculates the total Mach plane area for each axial location, generating an area distribution of the body.

The second phase deals with generating the second derivative distribution from the area distribution of the first phase. Initially, a cubic spline fit was attempted for the first and second derivation calculations, resulting in extreme fluctuations in the second derivative distribution. For this reason a five-point nested averaging technique is now used. Starting with the area distribution, a range of four slopes surrounding a given axis location are averaged to arrive at a first derivative value for that point. The same procedure is again used to calculate the second derivative. Each axial location along the body is handled in this manner except the extreme ends of the body where a five-point range is not available. In these two regions approaching either end of the body, progressively smaller slope averaging ranges are used. The end result is the generation of the second derivative of the area distribution for the body under investigation.

9.54"

R

x

Describing Equation: $R(x) = \left[\dfrac{-1}{(1.28)(6.04)}\left(\dfrac{x}{L}\right)+\dfrac{1.25}{6.04}\right]x$
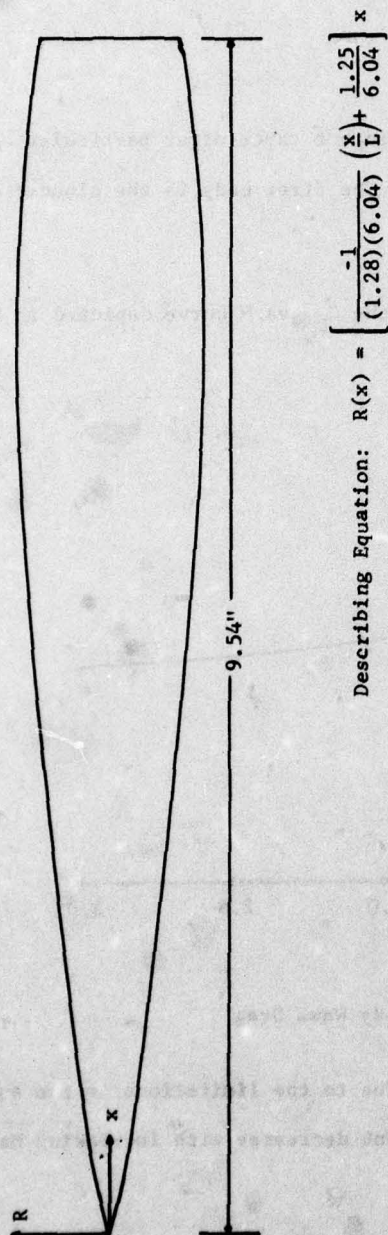
where L is the total length of the body, x is the distance from the nose to axial location in question, and R(x) is the radius value at that location, all given in inches.

L/d_{max}	L_{nose}/d_{max}	L_{nose}/L
6.04	4.83	.80

Figure 3. Slender Body (not to scale)

The third and final phase of the program deals with actually evaluating the wave drag equation as presented in Eqn (4). Knowing the reference area, S_{Ref}, of the body and the necessary area second derivative values, the program calculates the body wave drag coefficient for the particular Mach number specified.

IV. Test Case Results

Several body configurations were investigated, but three offer particular comparative capabilities and will alone be discussed here. The first body is the slender body of revolution specified in Figure 3.

For this smooth body, the program generated the C_{D_w} vs. M curve depicted in Figure 4.
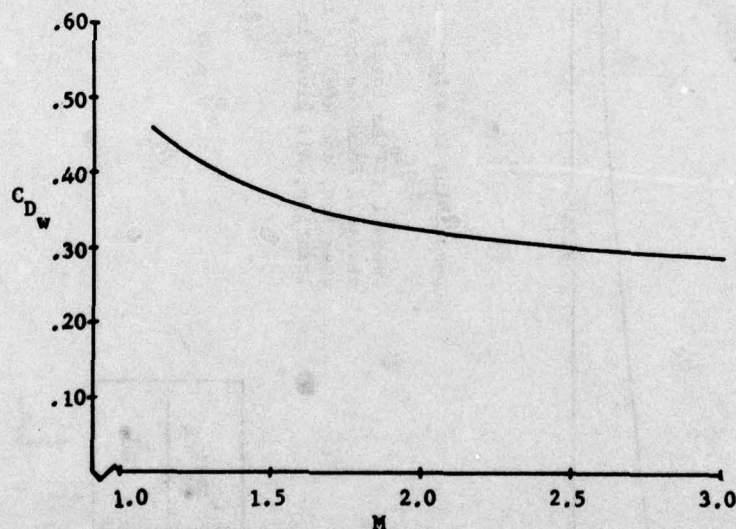
Figure 4. Smooth Body Wave Drag

Values near the speed of sound are invalid due to the limitations in the supersonic area rule theory. Also, the wave drag coefficient decreases with increasing Mach number within the velocity range investigated.

The second body used the first body as a baseline but had an axially symmetric protuberance added to a forward section of the body. The additional volume of the protuberance, given in Figure 5, was a small football-shaped volume addition distributed equally
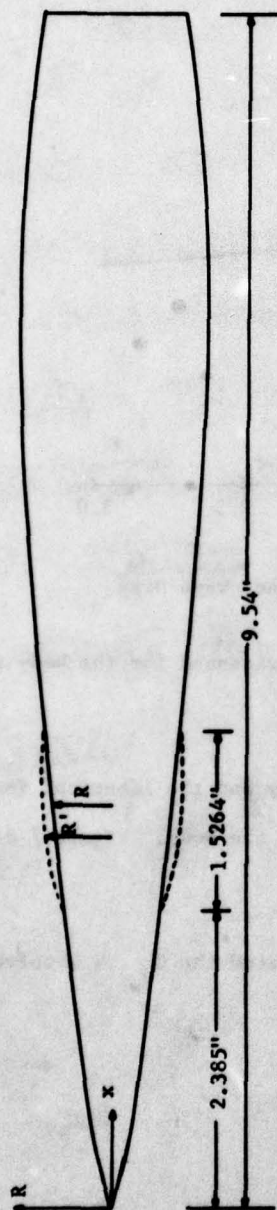
Describing Equation
in Region of Protuberance: $R'(x) = \sqrt{R(x)^2 + y(\zeta)^2}$

where R(x) is the radius of the underlying smooth body, R'(x) is the new radius of the body in the region of the protuberance, all given in inches. $y(\zeta)$ is given at left.

Additional Volume
Constituting Protuberance

$y(\zeta) = (-.2146018)\zeta^2 + (.3275681)\zeta$

(revolved around ζ axis)

Figure 5. Body With Forward Protuberance (not to scale)

67

about the slender baseline body axis.

For this body with forward protuberance, the program generated the C_{D_w} vs. M curve

depicted in Figure 6.
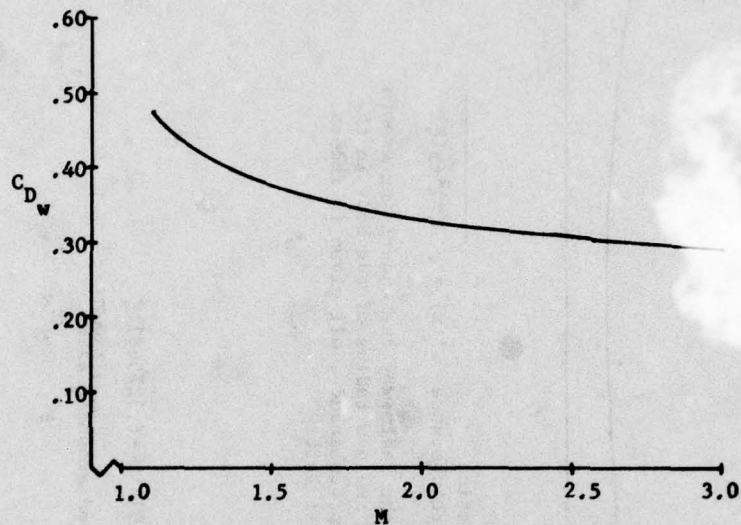
Figure 6. Body With Forward Protuberance Wave Drag

As with the smooth-body wave drag, the same trends were evidenced for the body with the
forward protuberance.

The third body also used the same smooth baseline body and the identical football-
shaped volume addition but located it in an aft region of the body. Figure 7 depicts
this third body.

For this body with aft protuberance, the program generated the C_{D_w} vs. M curve depicted

in Figure 8.

Describing Equation in
Region of Protuberance: $R'(x) = \sqrt{R(x)^2 + y(\zeta)^2}$

where $R(x)$ is the radius of the underlying smooth body, $R'(x)$ is the new radius of the body in the region of the protuberance, all given in inches. $y(\zeta)$ is given at left.

$y(\zeta) = (-.2146018) \zeta^2 + (.3275681)\zeta$
(revolved around ζ axis)

Figure 7. Body With Aft Protuberance (not to scale)
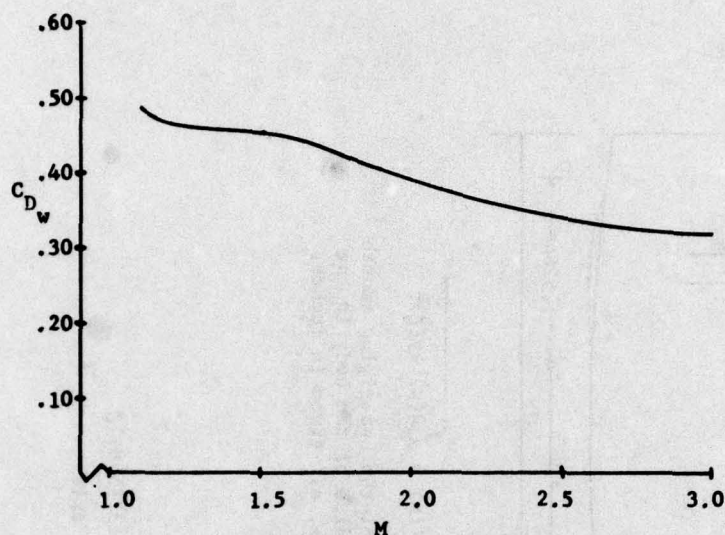
Figure 8. Body With Aft Protuberance Wave Drag

The shape of this curve was radically different from the previous two cases. The general trends still remain; however, the slope of this curve is noticeably different.

The three curves are shown together in Figure 9 along with smooth-body curves from reference 5.
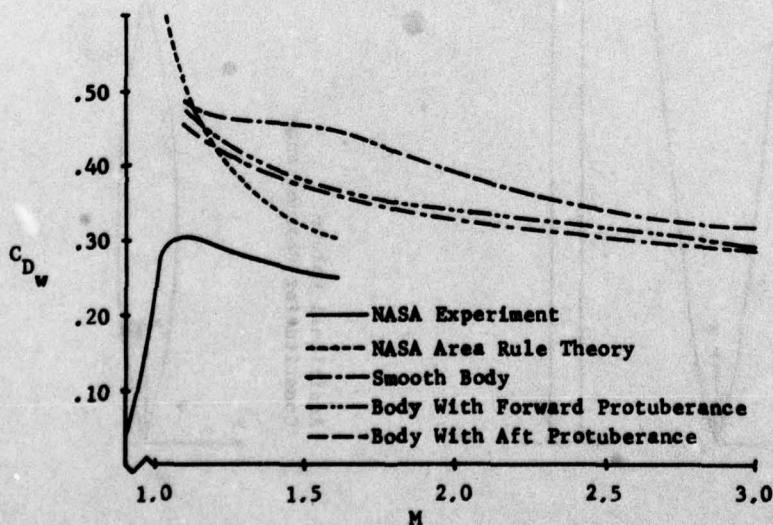
Figure 9. Wave Drag Comparison

This figure clearly shows that the curve trends identified for the three test cases are consistent with both NASA experimental data and NASA area rule theory. If the NASA curves are extrapolated toward higher Mach numbers, the difference between results becomes less pronounced. The forward protuberance does not appear to increase the wave drag appreciably over the velocity range studied. Conversely, the aft protuberance does, especially in the region between Mach 1.2 and Mach 2.20. The qualitative judgment can be made that the forward location is desirable over the aft location if the specified protuberance is to be added. Thus, this program offers an additional tool to the designer with respect to component location for minimum wave drag.

V. Conclusions

The sensitivity of this program allows even the slightest protuberance movement to be reflected in curve movement and shape changes. Ideal protuberance locations, over a range of Mach numbers, could possibly be theoretically determined for least wave drag. So far, values at higher Mach numbers more nearly approximate experimental data.

VI. Recommendations

Further research is needed in several areas. The models investigated in this report should be wind-tunnel tested for comparative purposes with the values obtained here. Additional baseline bodies and protuberance shapes need to be investigated to verify the capabilities of this program. The accuracy of both the area determination and second derivative calculation phases should be increased to determine the worth of such accuracy. A graphics capability to generate C_{D_w} vs. M curves for calculated values would drastically improve the program. Finally, a searching procedure to locate ideal protuberance location in order to achieve minimum wave drag over a desired Mach number range, should be added to the program to make it virtually self-contained.

References

1. Liepmann, H. W. and Roshko, A., Elements of Gasdynamics, John Wiley and Sons, New York, 1957.

2. Whitcomb, Richard T., "A Study of the Zero-Lift Drag-Rise Characteristics of Wing-Body Combinations Near the Speed of Sound," NACA Rep. 1273, 1956. (Supersedes NACA RM L52H08.)

3. Jones, Robert T., "Theory of Wing-Body Drag at Supersonic Speeds," NACA Rep. 1284, 1956. (Supersedes NACA RM A53H18a.)

4. Nicolai, Leland M., Fundamentals of Aircraft Design, Mets, Inc., Xenia, Ohio, 1975.

5. Nelson, Robert L., and Welsh, Clement J., "Some Examples of the Applications of the Transonic and Supersonic Area Rules to the Prediction of Wave Drag," NASA TN D-446, 1957. (Supersedes NACA RM L56D11.)

6. Jumper, Eric J., (Private correspondence), Department of Aeronautical Engineering, United States Air Force Academy, Colorado, July 1978.

7. Baker, W. P., and Nelson, D. A., (Private correspondence), Department of Mathematical Sciences, United States Air Force Academy, Colorado, 23-24 August 1978.

APPENDIX

COMPUTER LISTING

```
0100   $RESET FREE
0200   FILE 5(TITLE="DATA4",KIND=DISK,FILETYPE=7)
0300   FILE 6(KIND=PRINTER,MAXRECSIZE=60)
0400   DIMENSION RAD(10C,105),X(105),RC(150),Y(102),UNKY(300),AP(105)
0500   REAL MACH
0600   C
0700   C     CALCULATE X LOCATIONS AND CORRESPONDING RADII
0800   READ(5,100) NX,Y,EL,MACH,SREF,IFLAG
0900   100   FORMAT(I6,2F5.2,F12.7,I3)
1000   NX=NXY
1100   A=0
1200   DO 101 I=1,NX
1300   X(I)=EL/NX+A
1400   A=X(I)
1500   RC(I)=((-1./(1.28+6.C4))*(X(I)/EL)+(1.25/6.04))*X(I)
1600   101   CONTINUE
1700   N=0
1800   L=1
1900   DEG=.C174533*((3.1415927-(2*ARSIN(1/MACH)))/3.1415927)
2000   AFIN=0.0
2100   X1=EL/NX
2200   U1=ARSIN(1/MACH)
2300   C
2400   C     CALCULATE MACH ANGLE RADIUS AT X(I)
2500   1     X2=X(I)+X1
2600   Y1=X1*TAN(U1)
2700   K=X1/(EL/NX)
2800   IF(EL-X(I))*TAN(U1) .LE. R(NX)) Y1=R(NX)
2900   IF((EL-X(I))*TAN(U1) .LE. R(NX)) GO TO 7
3000   IF(ABS(Y1-RC(I+K)) .LT. 1.E-6) GO TO 7
3100   IF(Y1-RC(I+K)) 2,7,3
3200   X1=X1+EL/NX
3300   GO TO 1
3400   2     N=0
3500   B=((EL/NX)/2)
3600   3     X1=X1-B
3700   4     X2=X(I)+X1
3800   5     N=N+1
3900   RADIUS=((-1./(1.28+6.C4))*(X2/EL)+(1.25/6.04))*X2
4000   Y1=X1*TAN(U1)
4100   B=B/2
4200   IF(ABS(Y1-RADIUS) .LT. 1.E-6 .OR. N .GT. 30) GC TO 7
4300   IF(ABS(Y1-RADIUS) 6,7,4
4400   X1=X1+B
4500   GO TO 5
4600   6     IF(Y1-RADIUS) 6,7,4
4700   7     RAD(I,L)=Y1
4800   IF(L .EQ. 1) GO TO 8
4900   R3=(RAD(I,L)+RAD(I,L-1))/2
5000   DELA=(R3+R3*.0174533)/2
5100   AFIN=AFIN+DELA
5200   C
5300   C     CALCULATE MACH ANGLE RADIUS FOR 180 DEG OF REVOLUTION
5500   8     IF(ARSIN(1/MACH)*2*DEG .GT. 3.1415927) GO TO 20
5600   U1=ARSIN(1/MACH)*DEG
```

73

```
      N=0
      L=L+1
      IF(L .EQ. 91) GO TO 18
      IF(1.570796963-U1 .LT. C-C) GO TO 9
      IF(1.570796963-U1 .GT. 0.0) GO TO 16
      U2=3.1415927-U1
9     X1=EL/NX
10    X2=X(I)-X1
      Y1=X1*TAN(U2)
      K=X1/(EL/NX)
      IF(I .EQ. 1) GO TO 12
      IF(ABS(Y1-RC(I-K)) .LT. 1.E-6) GO TO 17
11    X1=X1+EL/NX
      GO TO 10
12    C=(C/2)
13    X1=X1-C
14    X2=X(I)-X1
      N=N+1
      RADIUS=((-1./(1.28*6.64))*(X2/EL)+(1.25/6.04))*X2
      Y1=X1*TAN(U2)
      C=C/2
      IF(ABS(Y1-RADIUS) .LT. 1.E-6 .OR. N .GT. 30) GO TO 17
15    X1=X1+C
      GO TO 14
16    X1=EL/NX
      DEG=DEG+.0174533*((3.1415927-(2*ARSIN(1/MACH)))/3.1415927 )
17    RAC(I-L)=Y1
      GO TO 19
18    RAD(I-L)=RC(I)
      X2=X(I)
19    R3=(RAD(I-L)+RAD(I-L-1))/2
      DELA=(R3+R3-.0174533)/2
      AFIN=AFIN+DELA
      DEG=DEG+.0174533*((3.1415927-(2*ARSIN(1/MACH)))/3.1415927 )
      GO TO 8
20    Y(I)=2*AFIN
      AFIN=0.0
21    CONTINUE
C
C     CALCULATE FIRST DERIVATIVE USING NESTED AVERAGE TECHNIQUE
C
22    UNKY(101)=(CY(2)-Y(1))/(EL/NXY)+Y(1)/(EL/NXY))/2
      UNKY(100+NXY)=(CYCNXY)-YCNXY)-YCNXY-1))/(EL/NXY)
      UNKY(99+NXY)=((YCNXY)-YCNXY-1))/(EL/NXY)+(Y(NXY-1)-Y(NXY-2))/(EL/
     1NXY))/2
      DO 23 J=3,NXY-1
      TRI=((Y(J)-Y(J-1))/(EL/NXY)+(Y(J-1)-Y(J-2))/(EL/NXY))/2
      QUAD1=((Y(J+1)-Y(J))/(EL/NXY)+(Y(J-1)-Y(J-2))/(EL/NXY))/2
      QUAD2=((Y(J)-Y(J-1))/(EL/NXY))/3
      IF(J .EQ. 3)) QUAD2=((Y(J-1)-Y(J-2))/(EL/NXY)+(Y(J-1)-Y(J-2))/(EL/N
     12))/(EL/NXY))/3
      IF(J .NE. 3) QUAD2=((Y(J-2)-Y(J-3))/(EL/NXY))/(EL/NXY)+(Y(J-1)-Y(J-2))/(EL/N
     1XY)+(Y(J-2)-Y(J-3))/(EL/NXY))/3
      QUAC=(QUAD1+QUAD2)/2
```

```
11700        IF(J .NE. 3) PENT=((Y(J+1)-Y(J))/(EL/NXY)+(Y(J)-Y(J-1))/(EL/NXY)
11800       1+(Y(J-1)-Y(J-2))/(EL/NXY)+(Y(J-2)-Y(J-3))/(EL/NXY))/4
11900        IF(J-1 .EQ. 3) PENT=((Y(J+1)-Y(J))/(EL/NXY)-(Y(J-2)-Y(J-3))/(EL/NXY)
12000       1+(Y(J-1)-Y(J-2))/(EL/NXY)+(Y(J-2)-Y(J-2))/(EL/NXY))/4
12100        UNK(Y(99-J)=(TRI+QUAD+PENT)/3
12200   23 CONTINUE
12300    C
12400    C    CALCULATE SECOND DERIVATIVE USING NESTED AVERAGE TECHNIQUE
12500    C
12600   24 AP(1)=0.0
12700        AP(2)=((UNKY(102)-UNKY(101))/(EL/NXY)+UNKY(101)/(EL/NXY))/2
12800        AP(NXY-1)=(UNKY(100+NXY)-UNKY(99+NXY))/(EL/NXY)
12900        AP(NXY)=((UNKY(100+NXY)-UNKY(99+NXY))/(EL/NXY)+(UNKY(99+NXY)-UNKYC
13000       198+NXY))/(EL/NXY))/2
13100        DO 25 J=2,NXY-2
13200        TRJ=(UNKY(J+101)-UNKY(J+100))/(EL/NXY)+(UNKY(J+100)-UNKY(J+99))/(
13300       1EL/NXY))/2
13400        QUAD1=((UNKY(J+102)-UNKY(J+101))/(EL/NXY)+(UNKY(J+101)-UNKY(J+100)
13500       1)/(EL/NXY)+(UNKY(J+100)-UNKY(J+99))/(EL/NXY))/3
13600        IF(J .EQ. 2) QUAD2=((UNKY(J+101)-UNKY(J+100))/(EL/NXY)+(UNKY(J+10
13700       10)-UNKY(J+99))/(EL/NXY)+(UNKY(J+99)+UNKY(J+98))/(EL/NXY))/3
13800        IF(J .NE. 2) QUAD2=((UNKY(J+101)-UNKY(J+100))/(EL/NXY)+(UNKY(J+10
13900       10)-UNKY(J+99))/(EL/NXY)+(UNKY(J+99)-UNKY(J+98))/(EL/NXY))/3
14000        QUAD=(QUAD1+QUAD2)/2
14100        IF(J .NE. 2) PENT=((UNKY(J+102)-UNKY(J+101))/(EL/NXY)+(UNKY(J+101)
14200       1-UNKY(J+100))/(EL/NXY)+(UNKY(J+100)-UNKY(J+99))/(EL/NXY)+(UNKY(J+99
14300       29)-UNKY(J+98))/(EL/NXY))/4
14400        IF(J .EQ. 2) PENT=((UNKY(J+102)-UNKY(J+101))/(EL/NXY)+(UNKY(J+101)
14500       1-UNKY(J+100))/(EL/NXY)+(UNKY(J+100)-UNKY(J+99))/(EL/NXY)+(UNKY(J+99
14600       29))/(EL/NXY))/4
14700        AP(J+1)=(TRI+QUAC+PENT)/3
14800   25 CONTINUE
14900    C
15000    C    CALCULATE WAVE DRAG
15100    C
15200        CDWTOT=0.0
15300        WCTOT=0.0
15400        CHDTOT=0.0
15500        DO 27 I=1,NXY
15600        IF(IFLAG .EQ. 1) WRITE(6,200) Y(I),AP(I+1)
15700  200 FORMAT(2F15.7)
15800        DO 26 J=1,NXY
15900        X1=I
16000        XJ=J
16100        XNXY=NXY
16200        ARGU=(XI/XNXY-(XJ-1.)/XNXY)
16300        ARG=ABS(XI/XNXY-XJ/XNXY)
16400        IF(J .LT. I .OR. J .GT. I) CDW=AP(J)*ALOG(ARG)*EL/NXY
16500        IF(J .EQ. I) CDW=AP(J)=2*(EL*(-ABS(ARGU*ALOG(ARGU)-ARGU)))
16600   26 CONTINUE
16700        WDTOT=AP(I)*EL/NXY+CDWTOT
16800        CWCTOT=CWDTOT+WDTOT
16900   27 CONTINUE
17000        CWCTOT=-.5*CWDTOT/3.1415927/SREF
17100        WRITE(6,201) MACH,CDWTOT
17200  201 FORMAT(//,F5.2,F15.7)
17300        END
17400
```

SECTION III

THERMODYNAMICS AND HEAT TRANSFER

A METHOD FOR MEASURING ATHLETIC POTENTIAL

John P. Jackson* and James E. Scott**

Abstract

This paper explores the use of the Keller runner model to obtain physiological para-
meters for use as an athletic aptitude measure. The Keller model is presented in detail
and related to sprints and distance runs. In this way four physiological parameters
representing strength, muscular endurance, flexibility and cardiorespiratory endurance
can be assigned numerical values. The technique of assigning values is demonstrated for
fourteen runners on which the appropriate data was taken. The consequences of this work
towark athletic aptitude measurement is discussed.

I. Introduction

There are a variety of techniques to measure athletic aptitudes of persons enrolled

in physical education programs. Often these are expressed in terms of accomplishment of

some feat: running so fast or jumping so far. Sometimes, however, athletic aptitudes

are related to physiological parameters of the human body but often involve expensive

test equipment such as the treadmill. The first category of measurements are usually

easier to make while the second correlates with physiological processes of the human

body. In this paper, we present a technique which combines the best of each category:

convenience of measurement and tie-in with human physiology. Only stop watches are

required, and yet, the final output of the measurement process is four physiological para-

meters characteristic of the human body.

These parameters are closely associated with four of the generally accepted com-

ponents of physical fitness (Ref 1). They are   Strength--the capacity of a muscle

to exert force against a resistance, Muscular Endurance--the capacity of a muscle to

exert a force repeatedly over a period of time, Flexibility--the ability to use a

muscle throughout its maximum range of motion, and Cardiorespiratory Endurance--

the capacity of the heart, blood vessels, and lungs to deliver nutrients and oxygen to

the tissues and to remove wastes.

*Captain, USAF, Associate Professor of Physics, DFP
**Captain, USAF, Director, Human Performance Lab, AHPR

II. Theory

A. Basic Equations

The athletic measurement process discussed herein depends upon the requirement that a runner must conserve energy and momentum. We use the analysis expressing this conservation as formulated by Joseph B. Keller (Ref 2 and 3).

A runner moving with a speed $v(t)$ will cover a distance x in time t according to the relation

$$x(t) = \int_0^t v(s)ds \qquad (1)$$

The speed $v(t)$, however, is not arbitrary, but must satisfy Newton's Law, that is, conservation of momentum:

$$f(t) - \frac{v}{\tau} = \frac{dv}{dt} , \qquad (2)$$

where $f(t)$ is the propulsive force per unit mass (which the runner exerts) and $\frac{v}{\tau}$ the friction force per unit mass. Strictly speaking, $f(t)$ is the forward contact force of the running surface upon the runner; but by Newton's Third Law, $f(t)$ is equal in magnitude to the actual force the runner exerts against the running surface (for which we assume no slip). Like Keller, we assume that body friction force per unit mass is proportional to speed with a constant of proportionality $1/\tau$. Thus, the friction coefficient τ is the first physiological parameter characteristic of the runner that will be measured.

Following Keller, we next make several conditions upon $v(t)$ and $f(t)$. First, we shall require that the runner starts from rest; hence,

$$v(0) = 0 \qquad (3)$$

Second, though $f(t)$ is under the control of the runner, we assume there exists an upper limit to $f(t)$ determined by the runner's physiology. Thus, for some F,

$$f(t) \leq F \text{ for all t.} \qquad (4)$$

F is the second physiological parameter.

A little thought will reveal that Equations (1) through (4) are insufficient to characterize a runner for all running situations. During a race, the runner does work at the rate fv which serves to deplete his body's energy reserves. In general, this rate always surpasses his ability to acquire energy by aerobic means if

78

f = F. For this reason, a runner can sprint only so far at full force before he exhausts all available energy resources. Thus, additional equations must be written to account for the energy balance.

If E(t) is the energy per unit mass available for running at some time t, then, according to Keller's simple formula,

$$\frac{dE}{dt} = \sigma - fv \tag{5}$$

where σ is the rate energy (per unit mass) can be made available to the runner by the aerobic process. Obviously, the runner always has an initial reserve of available energy E_o, for otherwise he would be unable to start running at all. Hence,

$$E(0) = E_o, \tag{6}$$

σ and E_o are the final two physiological parameters.

In order to couple Equation (5) with the running dynamics expressed by Equations (1) to (4), one more requirement must be stated: the available energy must always be positive during a run. If E becomes zero at any time, then the race must terminate. That is,

$$E(t) \geq 0 \quad \text{for } t \leq T \tag{7}$$

where T is the duration of the race.

Equations (1) through (7) are the basis for interpreting the scientifically controlled race described below. We obtained volunteer running subjects who we asked to run a set of four distances, D, in a minimal time, T. For short distances, this implied that f(t) equaled F. For long distances, f(t) was of necessity less than F; but in order to achieve a run in minimal time, all energy should have been used up at time, T, the time for the entire race. That is, E(T) = 0. As described below, these two conditions allowed a unique solution of Equations (1) through (7), and from these solutions the four athletic parameters were calculated from measurement data.

B. Sprints

First, consider the short distance runs (sprints). With f(t) = F, Equation (2) can be combined with Equation (3) to give

$$v(t) = F\tau \left(1 - e^{-t/\tau}\right). \tag{8}$$

Placing Equation (8) into Equation (1) gives

$$x(t) = F\tau^2 (t/\tau + e^{-t/\tau} - 1). \tag{9}$$

For times $t \ll \tau$, the initial acceleration of the runner is governed by the exponential term; but for times $t \gg \tau$, the maximum force is balanced by friction at a constant running speed and, as can be seen from Equation (9), x is linear with t.

The energy Equation (5) can be combined with Equation (2) and the result integrated to give

$$E(t) = E_o + \sigma t - \frac{1}{2} v^2 - \frac{1}{\tau} \int_o^t v^2 \, ds \geq 0 \qquad (10)$$

For the sprint, $v(t)$ is given by Equation (8) so that Equation (10) can be integrated to give $E(t)$. However, as already indicated, there will be a maximum time, T_c, for which a runner can spring with $f(t) = F$. Using the relation

$$E(T_c) = 0, \qquad (11)$$

we calculate from Equation (10)

$$T_c = \frac{E_o}{F^2 \tau - \sigma} \qquad (12)$$

(where it is assumed that $T_c \gg \tau$). Then, if we insert T_c into Equation (9), we compute the maximum distance, $D_c = x(T_c)$, for which a runner can sprint with $f(t) = F$:

$$D_c = \frac{1}{F} \left(\frac{E_o}{1 - \sigma/(F^2 \tau)} \right) \qquad (13)$$

Though this distance obviously changes from runner to runner, we interpret it as the natural dividing line between sprint and distance runs.

C. Distance Runs

Now, consider the distance run for which $f(t) < F$. Using optimal control theory, Keller showed that, with the exception of the start and finish (which may be ignored here), the speed v of the runner must be constant in order to minimize the time T for the given distance $D > D_c$. Perhaps we can make this plausible by the following argument: suppose the runner runs "slow" for part of the race to conserve energy. It is obvious he cannot run "slow" for the entire race, for then he would be unable to totally deplete his available running energy by the end of the race. This means he would then have energy left over which could have been used to give him a better time. Thus, he must speed up during some other interval of the race. However, according to Equation (10), the runner consumes his available energy, $E(t)$, as the speed squared; whereas, according to

Equation (1), he only buys an advantage in a shorter time according to the first power of his velocity. This strategy of variable speed wastes energy during times when he must run fast. Hence, he would make optimal use of his energy (and guarantee the shortest time) by running at a constant speed.

Substituting v = constant into Equation (10), and using E(T) = 0, we get

$$E_o + \sigma T - \frac{1}{2} v^2 - \frac{v^2}{\tau} T = 0 \tag{14}$$

from which we calculate v to be (using $T/\tau \gg 1$).

$$v = \sqrt{\frac{\tau(E_o + \sigma T)}{T}} \tag{15}$$

Since v = constant = D/T,

$$D = \sqrt{\tau (E_o + \sigma T)} \, T^{1/2} \tag{16}$$

in agreement with Keller.

III. Measurement of the Physiological Parameters

Equations (9) for sprints and (16) for distance runs show how running distance is related to time. Since these relations involve the four physiological parameters F, τ, σ, and E_o, it should be possible to compute these parameters for any given runner.

A. Sprints

In the case of sprints, the exponential term of Equation (9) can be neglected for times $t \gg \tau$. Under this approximation, Equation (9) becomes

$$t = \left(\frac{1}{F\tau}\right) x + \tau \tag{17}$$

Thus, if x(t) were plotted for a given runner, the slope of the line would be $(F\tau)^{-1}$ and the t-intercept would be τ. Following this reasoning, we timed volunteer runners using stopwatches at intervals of 10 meters as they sprinted a 100 meter dash. We analyzed the resulting data according to the method of least squares and calculated the best linear fit to the data. Since the method of least squares gives the error in both the slope and t-intercept, we were able to compute the statistical errors in F and τ. Figure 1 shows a typical graph of the least squares fit to a set of collected data on one individual.
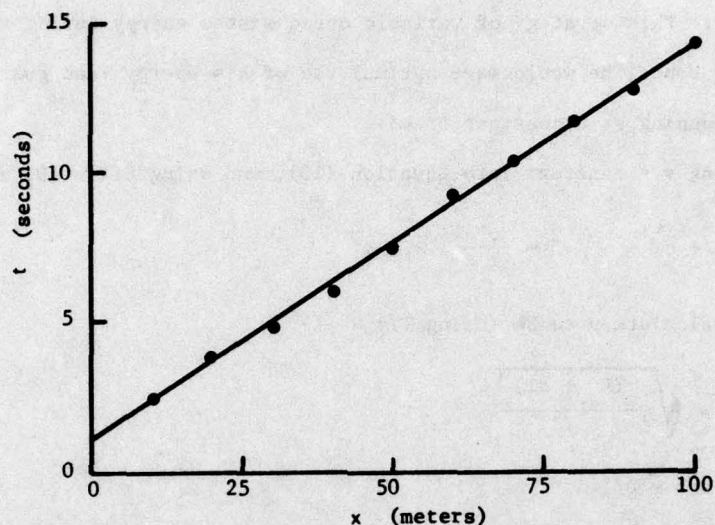
Figure 1. Typical time versus distance curve for volunteer subject. Line represents Least Squares fit to data measured by timers stationed at ten meter intervals.

B. Distance Runs

For distance runs, we had to collect and analyze the data quite differently. It was not possible to compute σ and E_o from just one race as for F and τ. The reason was that different running speeds must be used for different distances and hence we could not derive one equation analogous to Equation (17).

Using the same volunteers as in the sprints, we measured the time for run distances of 400, 800 meters, and the mile and a half (on separate days, of course). Actually, only two races are required to calculate the two parameters σ and E_o, but we used a third to estimate the error involved. We insured that the condition $E(T) = 0$ (Equation (14)) was well approximated by asking all subjects how much faster they thought they could have run the distance race; in all cases the estimated time decrease was much smaller than the total running time and so we assumed that Equation (14) was adequately satisfied.

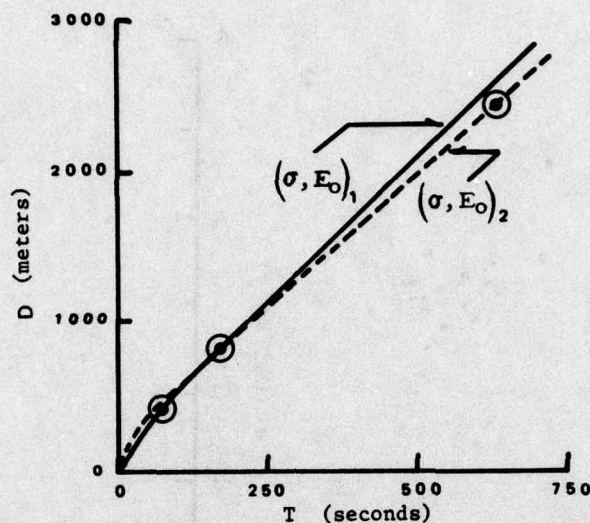Figure 2. Distance versus time graphs of Equation 16 drawn through three measured data points. Corresponding to each curve (only two of three possible are shown) is a unique set of σ and E_0. Note that each curve passes through only two of the three points (since each curve is uniquely determined by two parameters σ and E_0.)

Through any two points, it is possible to plot a curve according to Equation (16) which corresponds to a unique set of σ and E_0. Thus, as shown in Figure 2, we constructed three unique curves from the three data points, each corresponding to a specific σ and E_0. Since we could not establish which curve was the best characterization of the given runner, we treated each curve as having an equal a priori probability of being correct and simply computed the average σ and E_0 as well as their standard deviations as an estimate of the error. It should be pointed out that we also took into consideration the error involved in our previous measurements of τ. This, of course, was necessary since Equation (16), from which σ and E_0 were calculated, also involves τ. Hence, our reported error was increased accordingly.

IV. Results

Figure 3 shows the results of our measurements for F, τ, σ, and E_0. Though small, the data base of fourteen individuals (eight male, six female) reveals some noteworthy results. First, the distribution of mean values for all parameters fluctuate significantly more than the associated error limits. This means that this method of measuring athletic performance based on simple physiological parameters is capable of discriminating between individuals. Second, the data shows that Equations (9) and (16) predict the general features of how a runner covers a specific distance with time. If this were
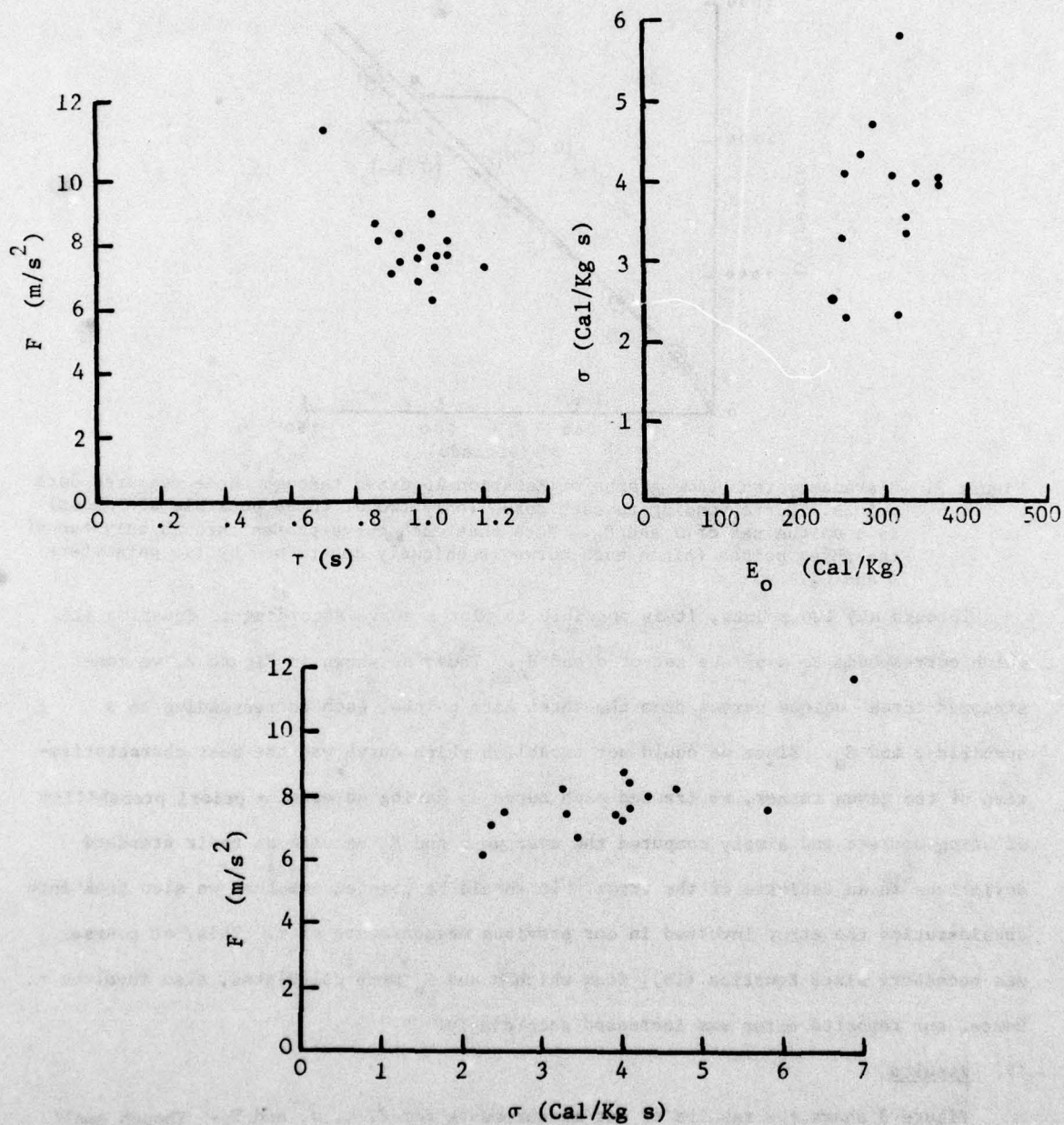
Figure 4. Correlation between physiological
parameters
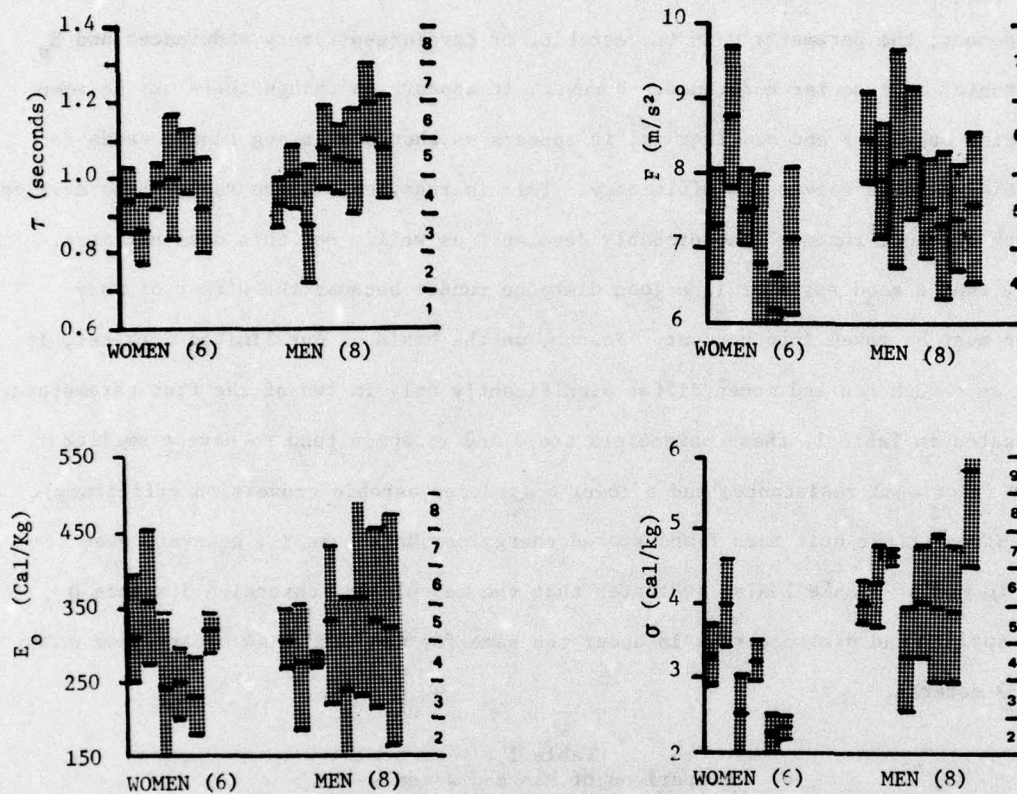
Figure 3. Measured values of physiological parameters for each subject. Shaded area indicates uncertainty in each parameter; mean value is at center. Superman values are $\tau = .89$ s, $F = 12.2$ m/s^2, $E_o = 575$ Cal/Kg, $\sigma = 9.9$ Cal/Kg s (Ref. 3). Point values for athletic evaluation scheme are shown at right of each chart.

not so, then our first observation would not be possible to make. It would seem, therefore, that other physiological factors (which certainly must play a role in a runner's performance but were not treated within the mathematical model) probably are second-order effects. Third, according to Figure 4, there appears to be little or no correlation between F and τ, and σ and E_o, that is, between the parameters associated with anaerobic and aerobic running.

Relating the four parameters to the components of physical fitness mentioned previously, we can make the following associations: the parameter F is most closely related

to the strength component; the parameter τ is probably greatly affected by the flexibility component; the parameter σ is the aerobic, or cardiorespiratory endurance; and E_o is anaerobic, or muscular endurance. However, it appears as though there may be some correlation between F and σ. That is, it appears as though a strong runner tends to have a high aerobic conversion efficiency. This is reasonable since runners who develop σ by long distance running also probably develop F as well. But this does not mean, however, that a good sprinter is a good distance runner because the effect of body friction must be taken into account. Fourth, on the basis of our limited data set, it appears as though men and women differ significantly only in two of the four parameters. As indicated in Table 1, these parameters are σ and τ; women tend to have a smaller τ (greater frictional resistance) and a lower σ (reduced aerobic conversion efficiency). Women's strength per unit mass F and stored energy per unit mass, E_o, however, seem comparable to men's. Table 1 also indicates that the calculated conversion distance, D_c, between sprints and distance runs is about the same for men (233 ± 44 meters) and women (220 ± 33 meters).

Table 1
Comparison of Men and Women's
Physiological Parameters

	τ	F	E_o	σ	D_c
Young Women:	$.956 \pm .066s$	$7.26 \pm .87 m/s^2$	$286.2 \pm 55.8 \frac{cal}{kg}$	$2.95 \pm .68 \frac{cal}{kgs}$	$220 \pm 33m$
Young Men:	$1.057 \pm .081s$	$7.76 \pm .46 m/s^2$	$309.9 \pm 40.9 \frac{cal}{kg}$	$4.18 \pm .77 \frac{cal}{kgs}$	$233 \pm 44m$

Fifth, the ratio of aerodynamic friction per unit mass, $\frac{\approx 1/2 \rho v^2 A}{M}$ (ρ, density of air; v, runner's sprint speed; A, cross-sectional area of sprinter; M, mass of runner), to the total body friction v/τ is no greater than about 10%; thus, most of the frictional resistance of a runner must be internally generated. Sixth, Figure 3 also shows the values calculated by Keller for a hypothetical athlete who runs every race in world record time regardless of distance. Appropriately enough, we refer to him as Superman; his parameters represent the "ideal" of human physiology.

V. Recommendations

Like measurements of academic potential, this method of determining athletic potential does not produce highly discriminating results. Nevertheless, it does seem

feasible to construct an evaluation system which arranges athletic potential in broad categories. To illustrate how this might be done, we have constructed the following simple evaluation scheme. We are not suggesting that this is the most suitable method, but it does show how athletic aptitude might be displayed. In our scheme, we assign the measurement of each physiological parameter an integer between one and ten. We chose the interval between each integer to correspond to the approximate measurement error of the parameter, for it is of no use to be concerned about fractions of a point since, as we have shown, the measurements are not that accurate. We arbitrarily selected the number five to be the approximate mean value of all subjects, regardless of sex. Figure 3 shows the way we assigned the integers to the four physiological parameters. Then, we summed the integer values for each parameter and plotted the resulting distribution as shown in Figure 5. Assuming that better athletic potential corresponds to higher values
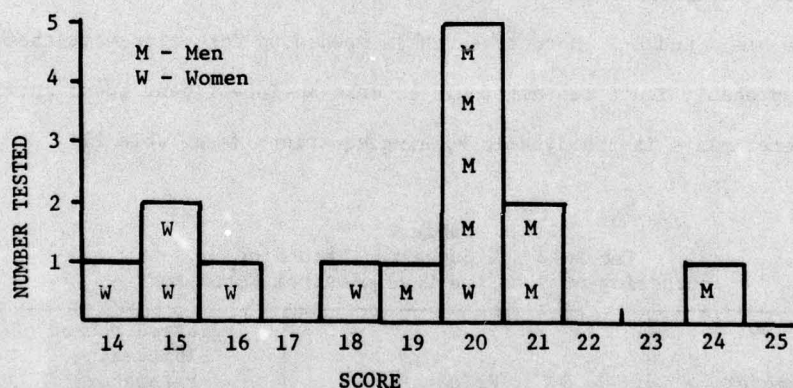
Figure 5. Distribution of total physiological score according to sex. Two overlaping distributions are suggested, one for women (14--20) and the other for men (19-24).

of each parameter, then, it would seem that the higher the summed score, the better the overall athletic aptitude. We note further that the use of a summed score allows deficiencies in one physiological parameter to be compensated by a stronger value in another.

Figure 5 shows the kind of distribution of parameters which can be expected using this running model. Differences of one point value on the summed scores correspond to significant differences in at least one parameter because of the way we assigned the integers to the measured data. It is noteworthy that two distributions seem to be apparent: one centered at 15 (an average of 3.75/parameter) and the other at 20 (an

average of 5/parameter). The lower distribution consists entirely of women; the upper consists of eight men and two women. This indicates that men and women should be evaluated separately, a fact not readily obvious since the physiological parameters do not depend on body mass.

An obvious question is what does one do with these data. We can only provide a partial answer at this time. Suppose a subject has a point rating of 18 which is distributed as follows: $\tau = 3$, $F = 5$, $E_o = 3$, $\sigma = 7$ (Recall from Figure 5, 3.75 is average for women, 5 for men). If the subject is a woman, her athletic aptitude should be considered high and, therefore, it would probably be difficult to raise her value appreciably (note that she is already almost average or above in all parameters.) But if the subject is a male, then his summed score might be raised considerably if certain parameters could be increased. These probably would be τ and E_o since F and σ are already average or above. Thus, an athletic program for him should involve those things which tend to increase his τ and E_o. More research is needed to determine what these things might be, but it probably isn't too difficult to make an intelligent guess knowing the role each parameter plays in the dynamic running equations (see Table 2).

Table 2
The Role and Suggested Method of
Increasing each of the Physiological Parameters

Parameter	Role	Suggested Method of Increasing Parameter
τ	Internal body friction, flexibility	Gymnastic exercise, limbering up.
F	Body strength per unit mass	Weight training.
E_o	Energy stored in body available for physical exercise, muscular endurance.	Diet, rest.
σ	Aerobic efficiency, cardiorespiratory endurance.	Distance running, distance swimming.

Finally, it should be pointed out that it is possible to determine via Equations (9) and (16) the effect on running time of a change in the physiological parameters. Thus, an indication how a given exercise program will translate into athletic performance is possible. This could be of value to track athletes in particular.

In conclusion, we present this study of a way to measure athletic potential as a feasibility study, not necessarily the way in which such a method would actually be implemented. Questions still remain. Could more accurate measurements be made, thereby reducing the error of each parameter? How would the data distribute for a much larger sample? Do the suggested exercises of Table 2 really affect the parameter significantly? Are the measured values of a physiological parameter repeatable for a given individual? Can the progress of training be followed by measuring athletic potential? How applicable is the friction coefficient t (as measured for sprints) to distance runs? In spite of these and other unanswered questions, it does appear to us that the method described herein could be used as an inexpensive method of measuring athletic aptitude and obtaining useful physiological information.

References

1. Getchell, Bud, <u>Physical Fitness</u>: <u>A Way of Life</u>, John Wiley and Sons, Inc, N.Y., 1976.

2. Keller, Joseph B., "Optional Velocity in a Race," <u>American Mathematical Monthly</u>, vol 81, pp. 474-480, 1974.

3. Keller, Joseph B., "A Theory of Competitive Running," <u>Physics Today</u>, September 1973.

DESIGN PROCEDURE FOR COUPLING
SAVONIUS AND DARRIEUS WIND TURBINES

R. C. Oliver[*] and P. R. Nixon[**]

Abstract

A design procedure for a combined Savonius and Darrieus Wind Turbine System is
presented and demonstrated. Individual system characteristics are described and dis-
cussed. System characteristics are combined and procedures prescribed to design either
maximum power output or minimum starting time systems. Generalizations are provided
for system design when specific test data does not exist and a possible application of
the resulting system is described.

I. Introduction

The recent upsurge of interest in alternate energy sources has included wind power.
Historical uses included, among others, grinding grain and pumping water. This use was
discontinued to a large degree as thermodynamics advanced and engines of high power
capacities were developed. Wind power could not compete with low-cost fuels and the
high-capacity engines. Recent developments increasing wind turbine efficiency and
the continued rise of conventional fuel costs have made wind-power systems a poten-
tially viable power source for certain situations. There is little doubt as to the
technical attainability of wind energy today, but the question of economic compet-
itiveness for general use remains (Ref. 1). The suitability of wind power to supple-
ment Air Force energy requirements has not been generally determined; however, several
current applications exist where wind power may be a viable alternative or supplement
for conventional fuels. Perhaps the most obvious use is a remote-site power source.
Wind energy is quiet, unobtrusive and has no identifying heat or noise emissions.
Depending on the location, the wind could supply all or a major portion of the power
required. Even used as a supplemental power source, a wind system can result in a
significant reduction of site logistical support. Supply and logistical support of
many such sites is costly, and often fuel must be transported over large distances or
difficult terrain. The amount of power needed is generally not large and within the
capabilities of moderate to small wind systems. In such a situation a wind system
may be the optimal choice. Used alone, some type of energy storage system sized for
windless periods would be required.

---

[*]Major, USAF, Assistant Professor of Aeronautics, DFAN

[**]C1C, USAF Academy

II. Background

With the remote site application in mind, a variety of wind-power systems were considered. The Darrieus Vertical Axis Wind Turbine (DVAWT) seems to be the most promising. Although invented in 1926, new interest has triggered significant study and advancement since 1971. Large programs by Sandia Laboratories and the Canadian National Research Council have been supplemented by NASA Langley, Oregon State University and other organizations (Ref. 2). The DVAWT, recognized by its eggbeater shape (see Figure 1), has several important advantages over other systems. First, due to shape, the wind can be accepted from any direction, and no yaw control system is required to orient the turbine into the wind. Additionally, the relatively simple tower construction, delivery of the mechanical energy naturally to the ground, and the lack of a pitch control system for synchronous applications contribute to the advantages of the DVAWT (Ref. 3). As a result of these factors, the power output per rotor weight and cost are among the best (Ref. 4), resulting in a cost which may approach one sixth that of horizontal axis systems (Ref. 5, 6 and 7). One item not yet addressed, however, is the inability of a Darrieus system to self start, even in gale force winds. The task reported here began with selection of a starter system for a remote-site Darrieus wind-power system.

III. Theory

A variety of concepts from electric motors to aerodynamic systems was considered as possible starting systems. The specific application greatly influenced the choice as did the previous selection of the primary system. An electric starter with its control and energy supply systems would add complexity and increase system weight while decreasing portability. An aerodynamic starter would have to be compatable with the vertical axis primary system (a horizontal turbine would require a yaw-control system and a transfer system to start the Darrieus.) A self-starting vertical axis turbine, however, avoids these complications and, therefore, a Savonius vertical axis turbine was selected. Invented in 1929, and finding a multitude of uses since then (Ref. 8), the Savonius Vertical Axis Wind Turbine (SVAWT) is capable of self-starting although it operates at a drastically different tip speed range than the DVAWT. The tip speed parameter is a ratio of the device rotational velocity to the wind speed. If used, the combined system must permit each device to operate in its own regime, or drag rather than thrust will result.

Luckily, the performance characteristics of both the Darrieus (Ref. 9, 10) and the Savonius (Ref. 11, 12) are known and documented for positive power conditions. Figure 2 illustrates the performance of characteristic Darrieus and Savonius turbines. The optimum tip-speed ratio for the best performance (maximum power) occurs at about 0.85 for the Savonius and about 6.0 for the Darrieus.
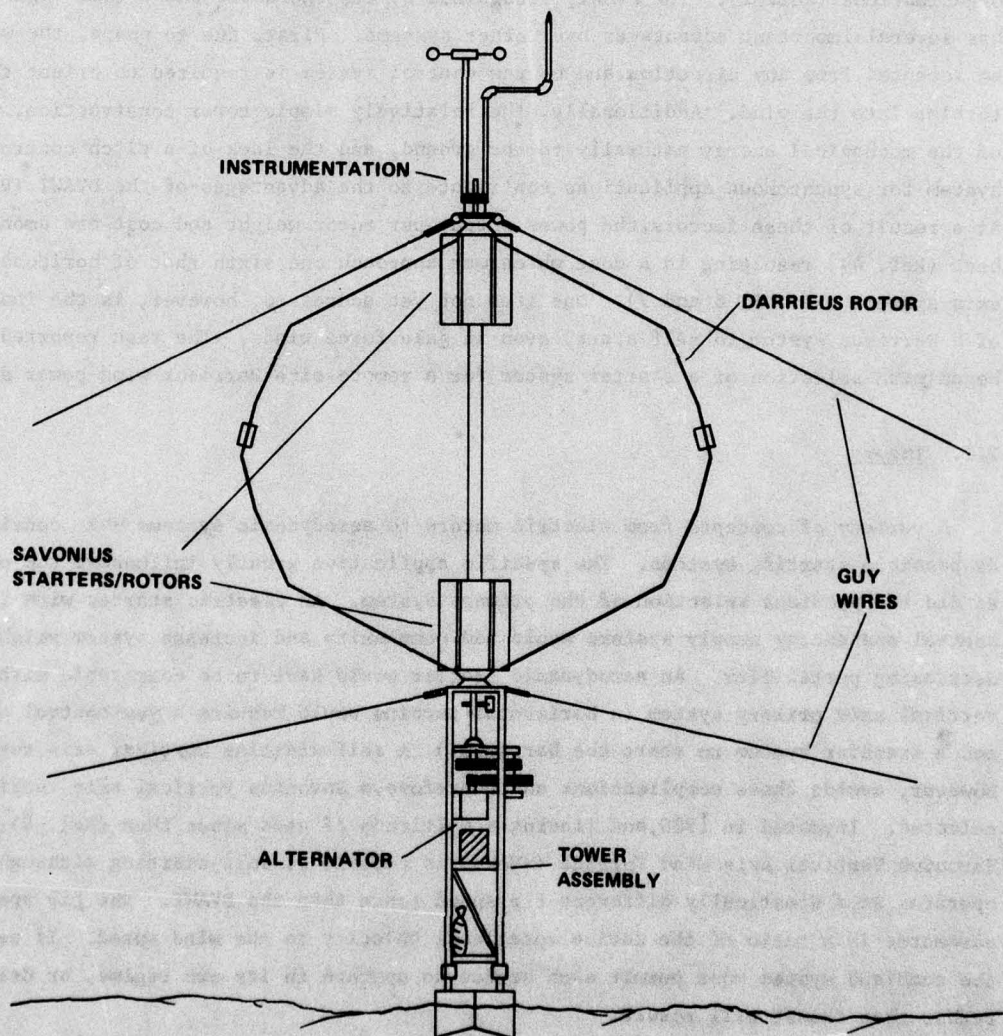
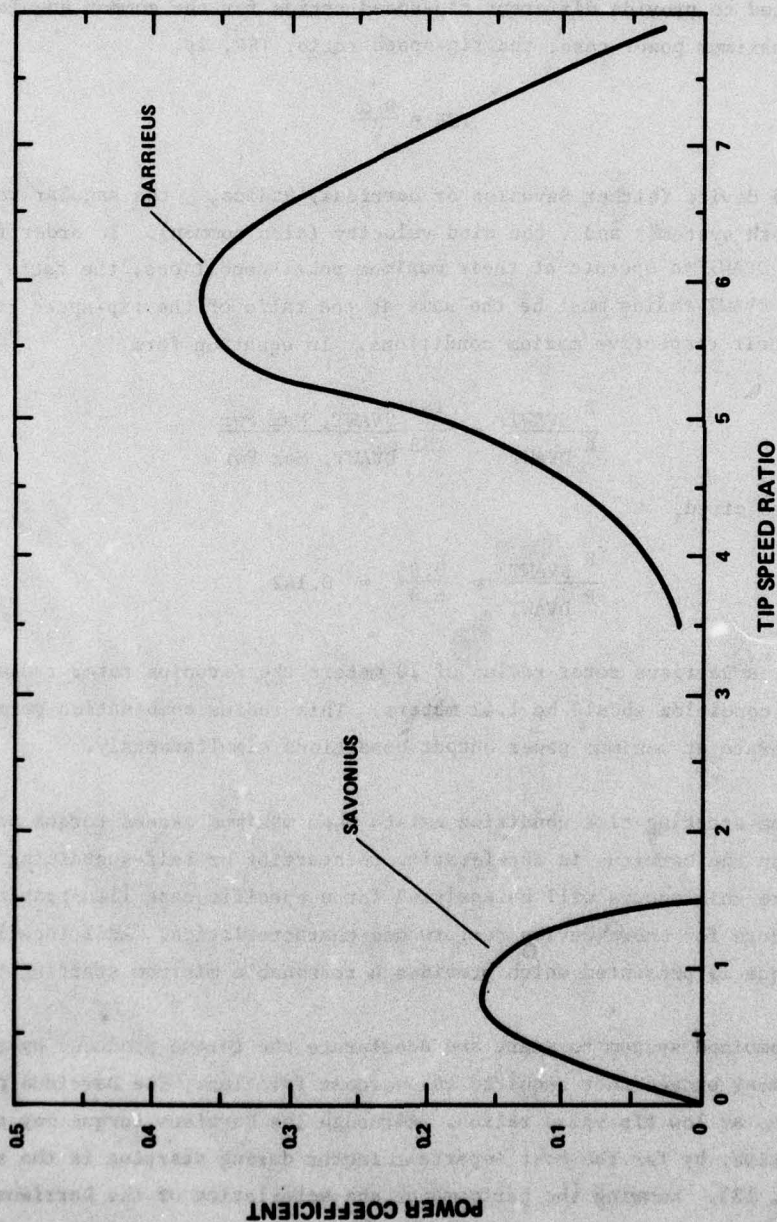Figure 1.   Schematic of Combined Darrieus and Savonius Self-Starting Wind Turbine

Figure 2. Performance of Characteristic Darrieus and Savonius Rotors

Maximum power for the combined system would be produced when both rotors operate at or near their respective tip-speed ratios for maximum power. The minimum starting time condition for the combined system, however, would exist when maximum Savonius power is produced during the Darrieus starting period. Both of these cases are addressed below. Since both the DVAWT and the SVAWT are on the same axis, the individual radii must be adjusted to provide different tip-speed ratios for the common angular velocity. Consider the maximum power case, the tip-speed ratio, TSR, is

$$TSR = \frac{R\,\omega}{V} \tag{1}$$

where R is the device (either Savonius or Darrieus) Radius, ω the angular velocity (common for both systems) and V the wind velocity (also common). In order for both the SVAWT and the DVAWT to operate at their maximum power conditions, the ratio of the SVAWT radius to the DVAWT radius must be the same as the ratio of the tip-speed ratios corresponding to their respective maxium conditions. In equation form

$$\frac{R_{SVAWT}}{R_{DVAWT}} = \frac{TSR_{SVAWT,\ Max\ Pwr}}{TSR_{DVAWT,\ Max\ Pwr}} \tag{2}$$

For the devices cited,

$$\frac{R_{SVAWT}}{R_{DVAWT}} = \frac{0.85}{6.0} = 0.142 \tag{3}$$

Therefore, for a Darrieus rotor radius of 10 meters the Savonius rotor radius for the maximum power condition should be 1.42 meters. This radius combination permits both devices to operate at maximum power output conditions simultaneously.

The minimum starting time condition exists when maximum excess torque occurs during the period when the Darrieus is accelerating to starting or self-sustaining speed. The condition where this occurs will be analyzed for a specific case illustrating the general procedure for known device performance characteristics. Additionally, a simple design technique is presented which provides a reasonable minimum starting time design.

For the combined system to start and accelerate, the torque produced by the Savonius and Darrieus must exceed that required to overcome friction. The Darrieus produces no positive torque at low tip-speed ratios. Although the Darrieus torque may even be slightly negative, by far the most important factor during starting is the system friction (Ref. 13). Knowing the performance characteristics of the Darrieus and the Savonius and the system friction, we can estimate the time required to accelerate the system to self-sustaining speed, where the Darrieus produces sufficient torque to overcome friction and continue accelerating to design conditions. The difference between the combined or total torque produced, T_{Total}, and the friction torque, $T_{Friction}$,

is a measure of the systems ability to accelerate. This can be stated mathematically as

$$T_{Total} = T_{Friction} + I \alpha \qquad (3)$$

where I is the system polar moment of inertia and α the angular acceleration,

$$\alpha = \frac{\delta \omega}{\delta t} \qquad (4)$$

where ω is the angular velocity, and t is time. The net torque, T_{Net}, then, provides the acceleration.

$$T_{Net} = T_{Total} - T_{Friction} = I \alpha \cong I \frac{\Delta \omega}{\Delta t} \qquad (5)$$

A constant acceleration or a short time period is assumed, to permit the difference form for the angular acceleration.

For a given system the performance characteristics can be determined based on the selected radius ratio and the starting time estimated using equation 5. In order to better understand the process, a sample problem for a representative DVAWT system is provided.

IV. Example Calculation

The characteristics of the system are presented in Table 1.

TABLE I

CHARACTERISTICS OF A DARRIEUS WIND
TURBINE FOR REMOTE-SITE APPLICATION

Height	12 Ft
Radius:	6 Ft
Polar Moment of Inertia:	700 lbm-Ft^2
	22 Ft-lbf-Sec^2
Starting Wind Velocity:	10 MPH
Self-Sustaining Speed	100 MPH
Frictional torque, including electrical generation system:	1.8 Ft-lbf
Operational Altitude	7000 Ft
Tip Speed Ratio:	6.0

Both Darrieus and Savonius characteristics are known and presented as a plot of power coefficient, C_p versus the tip-speed ratio and expressed as:

$$C_p = \frac{T \omega}{\rho V^3 RH} \qquad (6)$$

where T is the device torque, ω the angular velocity, V the wind speed, ρ the air

density, R the device radius, and H the height. The data are experimentally obtained. For any given system we can calculate the combined torque. The torque required to overcome friction can be estimated, but is more accurate if measured, when possible. Having the net torque and polar moment of inertia, we can use Equation 5 to solve for the required time.

Table 2 is an example calculation for the Darrieus data given in Table 1 combined with a Savonius having a radius of 1.79 feet and a height of 6 feet. Using a Savonius height of half the height of the Darrieus prevents possible interference with the highly loaded Darrieus center section. The Savonius starter would be split and mounted at the top and bottom portions of the Darrieus, (see Figure 3). The common angular velocity is ω, and X, C_p, T represent the tip-speed ratio, power coefficient and torque of the Savonius and Darrieus. The total torque is reduced by the frictional torque yielding the net torque. Equation 5 is then used to solve for the time required. The starting time is the sum of all times before the starting point. The Darrieus is considered started at a Darrieus tip-speed ratio of about 4.7. Note (Table 2) that at this point the Darrieus torque has begun to exceed friction with sufficient excess to provide continued acceleration.

TABLE 2

Sample Calculations for Combined System

Common ω [Rad/Sec]	SAVONIUS			DARRIEUS			TORQUE		Time ΔT Sec
	X_s*	C_{p_s}*	T_s	X_D**	C_{pD}**	T_D Ft lbf	Total T_T Ft lbf	Net T_N Ft lbf	
1.64	0.2	0.085	3.386	0.67		0	3.386	1.586	6.78
3.28	0.4	0.16	3.1864	1.34		0	3.1864	1.386	7.76
4.92	0.6	0.22	2.92	2.0		0	2.92	1.12	9.61
6.56	0.8	0.24	2.39	2.68	0	0	2.39	0.59	18.24
8.2	1.0	0.23	1.83	3.35	0.84	1.2	3.032	1.232	8.72
9.83	1.2	0.21	1.46	4.02	0.125	3.78	5.38	3.58	3.0
11.4	1.4	0.16	0.9	4.69	0.22	6.67	7.57	5.77	1.86

*Data Reference 12, pg 86
**Data Reference 13, pg 37

The total time until the system starts for this case is estimated at about 56 seconds. Any other case could be investigated in the same way by inputting the new radius and height. The specific performance characteristics of the devices also affect the results; thus, good data is a necessity.

In the general case, or for the designer who lacks comparative data, there exists a simpler technique for estimating the minimum starting time and maximum power conditions. Approximate data exist with respect to the tip-speed ratio for maximum power. The Savonius ratio for maximum power varies only fractionally with size, so a ratio of 0.85 will always be close. For a Darrieus of less than 5 meters radius a ratio of about 5.5 to 6.0 will result in maximum power. In general, a Darrieus will start at a ratio greater than three for a large rotor (Ref. 14), nearing 4.5 as the rotor size decreases. Based on these guidelines, we could choose the following conditions.

Maximum Power:
$$\frac{R_{SVAWT}}{R_{DVAWT}} = \frac{X_{XVAWT, max\ pwr}}{X_{DVAWT, max\ pwr}} = \frac{0.85}{5.75} = 0.148 \tag{7}$$

So for a small turbine a Savonius with 15% the radius of the Darrieus provides maximum combined power.

Minimum Starting Time:
$$\frac{R_{SVAWT}}{R_{DVAWT}} = \frac{X_{SVAWT, positive\ pwr}}{X_{DVAWT, start}} = \frac{1.4}{4.5} = .311 \tag{8}$$

For minimum starting time a Savonius radius of about 30% of the Darrieus rotor should be used. X_{SVAWT} for positive power is the highest value of tip-speed ratio for which the Savonius produces useable positive power and is generally a constant.

Although these results are based on general conditions, an error of a few percent does not have a significant input on the results. Recall, however, that this case is based on a Savonius height of half of the Darrieus height.

Having described the dynamic starting problem for a specific case, including several general guidelines, it is now necessary to assure a static start for the design chosen.

A static starting check of the system can be made using the functional relationship proposed by Blackwell (Ref. 15) similar to Equation 6.

$$CQ = \frac{Q}{\frac{1}{2} \rho V^2 R A_s} \tag{9}$$

Where CQ is an experimentally determined static torque coefficient, Q is the net static torque produced, A_s is the turbine swept area, and the other terms have been previously

defined. The swept area is twice (2 buckets) the height times the radius, so

$$CQ = \frac{Q}{\rho V^2 R^2 h} \tag{10}$$

Using the minimum torque coefficient suggested, 0.25, and the device parameters as specified, including a height of 6 feet, we find that the static torque is 2 ft-lbf which is sufficient to overcome the frictional drag of 1.8 ft-lbf. In all cases examined, the device designed for dynamic starting provided sufficient static torque for starting. An actual device was constructed based on the described design example. Details are provided in a subsequent section and Figure 3 is a picture of the device.

One additional characteristic of the combined system which must be described is its ability to self-regulate or prevent an overspeed condition naturally, without controls. Both the Darrieus and Savonius contribute to this ability. Firstly, the Darrieus blades are high lift-to-drag ratio sections for which the lift and drag forces are strong functions of the local blade angle of attack. The velocity of the blade, due to rotation and the wind velocity, combine to form the resulting total flow which strikes the blade. At low rotational speeds a small angle of attack results and the lift-to-drag ratio is small (as in the previously described case where the torque is slightly negative.) As the rotational velocity approaches the design point, the angle of attack increases and produces a large lift-to-drag ratio providing the positive torque regime. As rotational speed increases further, the angle of attack increases, causing a stall of the blades, reducing the lift-to-drag ratio and preventing an overspeed or runaway condition. Basic airfoil theory explains both the starting problem and the natural speed limiting (Ref. 16).

The Savonius also contributes to this inherent speed limiting; although not explained as clearly in terms of the angle of attack, the Savonius also produces negative torque or drag once its tip-speed ratio exceeds that where positive power is produced. See Figure 1. Although the tip-speed ratio at which this occurs can be estimated, the exact performance beyond this point is in question. It is postulated that, unlike the Darrieus which simply stops producing torque, the Savonius actually produces negative torque or drag beyond its maximum tip-speed ratio for positive power. No data was found to support this contention because experimental results have been concerned with the positive power output regime. Not only will this additional drag help prevent overspeeding, but it should also be considered in the maximum power output. For example, the starter (Savonius) designed for minimum starting time will be in the drag regime during the Darrieus maximum power condition and, once quantified, should be considered. The ability to self-regulate is a significant advantage relative to other wind power systems which often employ active control systems to prevent overspeeding.
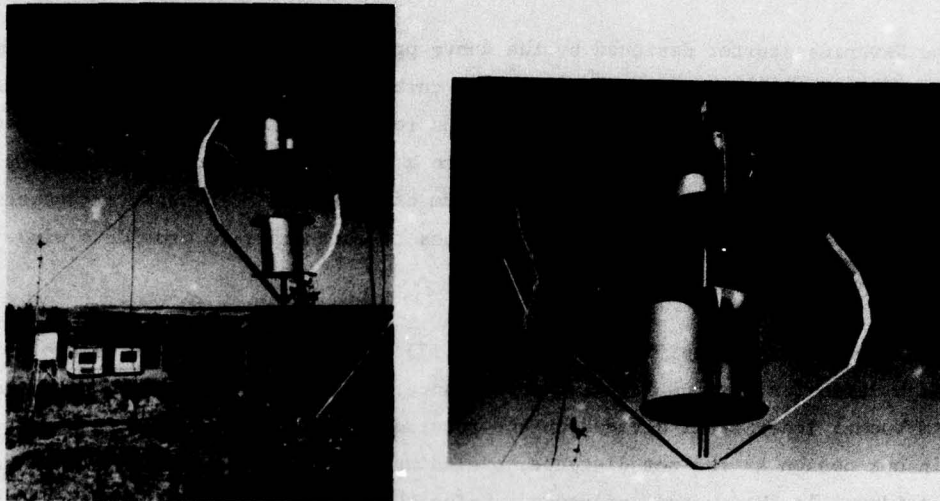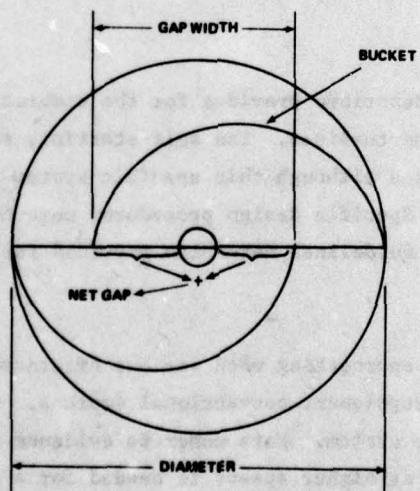
Figure 3. Photographs of Device Constructed

Figure 4. Sketch of Savonius Starter Illustrating Net Gap Width

V. Construction Details

The Savonius starter designed by the above procedure for minimum starting time was constructed and will be tested on a Darrieus turbine of the design described; results will be reported when available. Two Savonius rotors of three-foot height were constructed. Considerable attention was given to a design permitting easy assembly of the entire apparatus in the field by a minimum of personnel. The starter buckets of the two Savonius rotors were mounted 90 degrees to each other to provide a wind-catching surface in all directions.

Many experiments (specifically Reference 17) have shown that there exists an optimum gap width ratio for maximum Savonius performance. This ratio is the gap distance between bucket inner radii divided by the rotor diameter, see Figure 4. The gap width used in our design is the net distance, excluding the center support pole which was not considered in the quoted reference. Using the net distance, then, the gap width ratio should be between 0.1 and 0.15 for maximum performance (Ref. 18).

A minimal load analysis of the Savonius rotor buckets indicated that 0.063 inch aluminum sheet buckets with 0.10 inch aluminum end plates would suffice under the given conditions (Ref. 19).

VI. Summary

The design procedure described provides for the combination of Darrieus and Savonius Vertical Axis Wind turbines. The self-starting, self-regulation combined system has a variety of uses although this specific system was designed for possible remote site application. Specific design procedures were outlined for known performance characteristics. General guidelines were also provided for designs when specific data is not available.

The period is rapidly approaching when various alternate energy schemes must be considered to replace or supplement conventional sources. A combined Darrieus-Savonius system offers one possible system. More concrete evidence as to exact performance, specifically the Savonius at higher speeds is needed for a precise analysis.

References

1. B. F. Blackwell and L. V. Feltz, Wind Energy - A Revitalized Pursuit, Sandia Laboratories Energy Report Sand 75-0166, p. 6, 1975.

2. R. W. Thrasher and R. W. Wilson, "Design Consideration for the Darrieus Rotor," Eleventh Intersociety Energy Conversion Engineering Conference Proceedings, Vol II, American institute of Chemical Engineers, New York, pp. 1695-1703, 1976.

3. E. G. Kadlec, "The Darrieus Verticle-Axis Wind Turbine Program," Sharing the Sun, Vol 7, Winnipeg, Canada, p. 351, 1976.

4. Department of Energy, "A Fresh Interest in Wind Energy," The Sacramento Bee, p. CL 11-12, March 4, 1978.

5. P. South and R. S. Rongi, "The Performance and Economics of the Verticle-Axis Wind Turbine Developed at the National Research Council," Paper No. PNW 73-303, American Society of Agricultural Engineers, pp. 14-16, 1974.

6. Ibid., Blackwell, p. 8-9, 1975.

7. B. F. Blackwell, The Verticle Axis Wind Turbine "How it Works," Sandia Laboratories Energy Report, SLA-74-0160, p. 3, 1974.

8. D. M. Simmons, Wind Power, Noges Data Corp, Park Ridge, NJ, pp. 101-104, 1975.

9. R. J. Templin, Aero Dynamic Performance for the NRC Verticle-Axis Wind Turbine, National Research Council of Canada, LTR-LA-160, 1974.

10. R. E. Sheldahl, B. F. Blackwell, Free-Air Performance Tests of a 5-Meter -Diameter Darrieus Turbine, Sandia Report, SAND 77-1063, 1977.

11. B. G. Newman, Measurements on a Savonius Rotor with Variable Gap, Sherbrooke University Symposium on Wind Energy, 1974.

12. B. F. Blackwell and others, Wind Tunnel Performance Data for Two and Three Bucket Savonius Rotors, Sandia Energy Report, SAND 76-0131, 1977.

13. B. F. Blackwell, R. E. Sheldahl and L. V. Feltz, Wind Tunnel Performance Data for the Darrieus Wind Turbine with NACA 0012 Blades, Sandia Laboratories Energy Report Sand 76-0130, p. 31, 1976.

14. Ibid., Blackwell, p. 8, 1974.

15, Ibid., Blackwell, p. 10-36.

16. B. F. Blackwell, and others, "Engineering Development States of the Darrieus Wind Turbine," Sandia Energy Report, Sand.

17. Ibid., Blackwell, 1977.

18. Ibid., Blackwell, p. 31, 1977.

19. P. R. Nixon, A Starter for the Air Force Academy Darrieus Wind Turbine, unpublished report, 1978.

SECTION IV

INSTRUMENTATION AND HARDWARE

HARMONIC OPTIMIZATION OF A
PERIODIC FLOW WIND TUNNEL

John P. Retelle, Jr.[*] and Donald A. Kennedy[**]

Abstract

Numerous methods have been used to generate axial gusting in wind tunnels. Attempts to increase the amplitude of velocity oscillations about a mean velocity have usually resulted in increasing the harmonic content of the power spectrum of the free stream velocity. This work describes a wind tunnel modification which was specifically designed to produce a sinusoidal perturbation to the mean velocity which was free from unwanted higher harmonic effects. Velocity perturbations were produced by rotating vanes mounted downstream of the tunnel test section. A flow bypass mechanism provided harmonic supression which could be optimized for the various combinations of velocity-oscillation amplitude and frequency used in unsteady flow experiments. Depending on the flow conditions, results showed that the second harmonic power amplitude could be greatly suppressed and that higher harmonics could not be detected.

I. Introduction

Recent experimental investigations of unsteady boundary layer separation and dynamic stall have used unsteady variations of airfoil angle of attack (Ref. 1, 2), free stream velocity (Ref. 3, 4, 5), or both (Ref. 6). Of these configurations, experiments dealing with oscillatory velocity perturbations about a mean velocity have provided greater ease of data collection near the surface of a fixed airfoil, while still producing unsteady flow phenomena resembling that noted during dynamic stall on an airfoil oscil-

lating in pitch. These unsteady effects, such as the presence of regions of unseparated, reversed flow in the airfoil boundary layer, have been observed (Ref. 5) to be strong functions of the frequency and amplitude of the oscillatory free stream velocity perturbations. In addition, recent experimental data (Ref. 5) have shown that the presence of higher harmonic content in the power spectrum of the oscillating free stream velocity produced large unsteady variations in the response of the unseparated flow reversal regions. Thus, free stream flow oscillations can be extremely useful in reproducing unsteady flow effects. To simplify the flow physics, however, care must be taken to suppress or eliminate the second and higher harmonics (terms of factor 2 or higher in a Fourier series expansion of the free stream velocity) which are especially prevalent at large oscillation amplitudes.

[*]Captain, USAF, Assistant Professor, Department of Aeronautics, U.S. Air Force Academy

[**]Assistant Professor, Department of Aerospace Engineering Sciences, University of Colorado, Boulder.

The wind tunnel modification described below was specifically designed to produce a large-amplitude sinusoidal perturbation to the mean velocity which was free from unwanted higher harmonic effects. A set of rotating vanes at the downstream end of the test section was designed to periodically block the flow to the axial flow fan located further downstream. A nearly constant air flow was provided to the fan by a bypass mechanism which allowed the fan to operate at a nearly constant pressure rise, improving the harmonic suppression in the flow. It was found that this harmonic suppression could be optimized for the various combinations of velocity oscillation amplitude and frequency used in other experiments.

Several experiments in wind tunnels have used the rotating vane principle to perturb the flow. Two similar tunnels made no attempt to improve the suppression of higher harmonics. An apparatus on an open-circuit wind tunnel described by Despard (Ref. 7) used four rotating vanes downstream of the test section to produce velocity variations of up to 40 percent at oscillation frequencies of up to 240 Hz. The second and third harmonics contributed 23 percent and 4 percent of the velocity power spectrum, respec- tively. An almost identical apparatus was described by Morkovin, Loehrke, and Fejer (Ref. 8) which perturbed the flow in a closed-circuit wind tunnel. They found resonances which corresponded to the tunnel circuit length, the distance between the rotating vanes, and the tunnel contraction. They also noted large departures from sinusoidality associated with large velocity oscillation amplitudes. Recent work in this tunnel by Saxena, Fejer, and Morkovin (Ref. 4) produced plots of the velocity and pressure fluctuations which indicated a higher harmonic content in the pressure fluctuation than in the longitudinal velocity variation.

Several different schemes have been tried to eliminate higher harmonic content in the velocity oscillations of these rotating-vane tunnels. Karlsson (Ref. 9) used four rotating vanes downstream of the test section of an open-circuit wind tunnel to produce root-mean-square velocity variations of 34 percent of vane rotation frequencies of up to 48 Hz. At high frequencies the higher harmonics were responsible for about 15 percent of the total root-mean-square amplitude of the fluctuation. In an effort to reduce these harmonics, the lowest vane was turned at a higher rate, but no mention is made of the success of this device. Simpson (Ref. 10) described an apparatus of this type which used five rotating vanes downstream of the test section of an open-circuit tunnel. A programmable motor was used to adjust the angular velocity of the rotating vanes, thereby optimizing the higher harmonic suppression. The resulting velocity waveforms appeared sinusoidal, but no harmonic analysis was presented.

An interesting variation to the rotating vane device was described by Charnay and Mathieu (Ref. 11). Their eight rotating vanes were positioned upstream of the test section in the settling chamber ahead of the screens and honeycomb sections of the open- circuit wind tunnel. They found that the smallest harmonic content occurred when the

vane vortex-shedding frequencies matched the tunnel resonant frequencies. Turbulent velocities were measured to evaluate the effect of the upstream-mounted vanes. They observed that optimum sinusoidality was indicated by maxima of the magnitudes of the longitudinal and vertical turbulent fluctuating velocities, u_1' and u_s', and by minima of the skewness and flatness factors of u_1'. They measured the turbulence intensity in the test section downstream of the vanes to be on the order of 0.7 percent.

The rotating vane apparatus described below was capable of higher harmonic suppression to a greater degree than the devices described above, with the possible exception of the device described by Simpson (Ref. 10). Careful adjustment of the bypass mass flow vided regulation of the higher harmonics in the test section for a given tunnel mean velocity and vane rotation frequency. Depending on the vane size and flow conditions, the second harmonic power amplitude could be suppressed as much as 48 db.

II. Experimental Apparatus

The unsteady flow device was installed in the two foot by two foot (0.61 meter by 0.61 meter) cross-section, low-speed wind tunnel at the University of Colorado, Boulder. It was an open-return, suction-type wind tunnel with the addition of the unsteady flow apparatus. Figure 1 shows a schematic of the wind tunnel. The test section was 14 feet (4.27 meters) in length with a 10 foot (3.05 meter) long plexiglass wall, ½ inch thick. Downstream of the test section were the unsteady flow device, a transition section to the fan, the fan, and the conical diffuser.

A periodic disturbance to the mean flow was produced by a set of six rotating vanes located just downstream of the test section. Figure 2 shows a schematic of the vane drive apparatus. Three sets of vanes of varying width were used during this experiment to change the amount of maximum tunnel blockage and, thus, the velocity amplitude variation, N. The vanes were made in a modified diamond shape, both for ease of construction and for minimal pressure and friction losses. Of the three sets of vanes, set A used a 2.000 inch chord, set B used a 3.495 inch chord, and set C used a 3.980 inch chord. The three vane sets produced tunnel area blockages of 50, 87.5, and 99.5 percent, respectively. The rotating vanes were driven by a gear train which was in turn powered by a General Electric Stratitrol II 3/4 horsepower, full-wave, direct-current motor controlled by a Variac-equipped, direct-current power supply. An 8-to-1 gear reduction allowed the motor to run smoothly near the middle of its 0-1759 revolutions-per-minute speed range preventing surging at low speeds. The gear drive was designed to allow the vanes to counterrotate and, thus, produced no net local lift perturbation to the flow.

The bypass mechanism allowed air to enter the fan section when the test section was blocked by the front (free stream-controlling) vanes. Three rotating vanes on the top
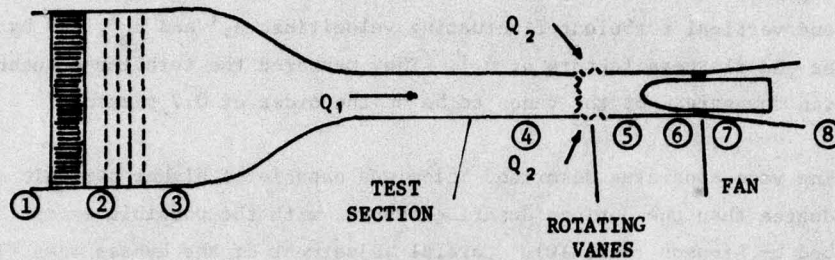
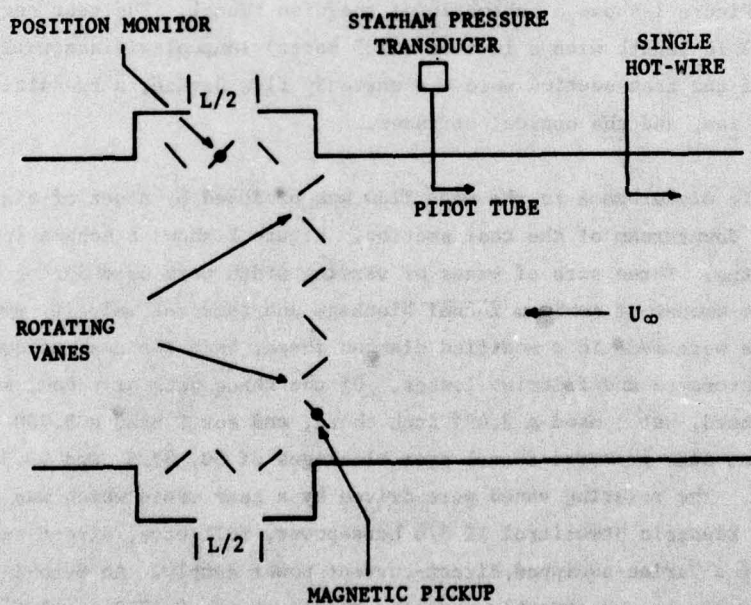Figure 1. Schematic of Wind Tunnel

Figure 2. Test Section Schematic

of the device and three on the bottom were driven by the same gear train which drove the front vanes. The vanes on the top and bottom allowed air from the laboratory to enter the fan section at a varying rate which balanced the decrease flow in the test section. The adjustment of the bypass air flow into the fan section was controlled by moveable slides which are shown in the test section schematic of Figure 2. These slides were set to predetermined bypass openings based on the flow conditions desired in the test section. Unlike the front vanes, the bypass vanes had a fixed 2-inch (5.08 cm) chord (vane set A).

The free stream steady turbulence level, $\left(\sum_{i=1}^{3} \sqrt{\overline{u_i'^2}}\right) \Big/ U_\infty$, for the basic wind tunnel was measured by Francis (Ref. 12) at a nominal value of 0.06 percent for a free stream velocity of 60 feet per second (18.29 meters per second). In this expression, u_i are the turbulent velocity components, and U_∞ is the magnitude of free stream velocity. Turbulence intensity measurements with the rotating vane device installed were made using a Bruel and Kjaer type 2417 Random Noise Voltmeter which had a bandwidth of 2-20,000 Hz. With the large front vanes (set C) fixed at the minimum resistance (full open) position, the steady flow turbulence level was measured to be 0.08 percent at a free stream velocity of 60 feet per second (18.29 meters per second). The vanes were then rotated at 3.33 Hz and the turbulence level was measured to be 0.54 percent at a mean flow velocity of 12 feet per second (3.66 meters per second). To determine the effect of unsteadiness on the higher frequency turbulence, this velocity data signal was filtered through a 4 Hz high-pass filter. The higher frequency root-mean-square turbulence level was then measured to be 0.05 percent.

III. Unsteady Flow Field Analysis and Optimization

Results of an analysis by McMichael (Ref. 13) show that a tunnel of this type could be optimized to suppress flow harmonics and could, in certain configurations, eliminate all even harmonics. The applications of this analysis are described below as well as a description of the mechanical optimization using the unsteady flow device.

The analysis of McMichael (detailed in the Appendix) showed that the smallest temporal change in the pressure rise across the fan occurred when the pressure and frictional losses across the bypass ports and vanes were equal to the sum of the pressure drop across the main tunnel vanes and the frictional loses in the test section. Careful adjustment of the bypass port openings permitted a fine tuning of the bypass frictional losses and permitted an almost steady flow to reach the fan. The resulting unsteady free stream velocity was of the form

$$U_\infty(x,t) = U_1(x)\left\{1 + N\sum_{n=1}^{\infty}\left[a_n \cos(n\omega t) + b_n \sin(n\omega t)\right]\right\} \tag{1}$$

where U_1 (x) is the mean velocity (as a function of axial distance x) and N is the oscillation amplitude. The analysis showed that, once the free stream velocity and oscillation frequency were set and the resulting oscillation amplitude measured, the bypass flow could be varied to suppress all the coefficients in equation (1) except b_1. In addition to the harmonic suppression, McMichael has shown that the even harmonics of the flow oscillation can be eliminated when the main flow vanes and bypass flow vanes are identical.

The goal of the unsteady flow analysis was to provide a longitudinally oscillating flow at a desired amplitude ratio, oscillation frequency, and mean velocity whose power spectrum was as free as possible of harmonic content. For the experiment, of the four controllable tunnel parameters, a combination of vane size, steady tunnel velocity, and vane rotation frequency (or rotation period) were selected to produce the desired frequency and oscillation amplitude ratio. The upper and lower fixed bypass openings, each at a setting of L/2 (see Figure 2), were then adjusted for maximum second harmonic suppression according to the parameters suggested by the analysis. The variable bypass provided a more uniform flow to the fan over the period of, and in correlation to, the vane rotation.

IV. Results of Unsteady Flow Optimization

Mean and oscillating velocities were measured in the test section using a single-wire hot-wire anemometer. The linearized output voltage was ensemble-averaged over 50 data entries, with the start of each data-collection cycle being triggered by a magnetic pickup mounted on the vane gear drive. A power spectrum of the resulting signal was produced using a Fourier analyzer. A typical power spectrum of the linear-ized velocity signal for the small vanes (set A) is shown in Figure 3 for a non-dimensional frequency of k=0.873 and a bypass opening of (L/2)=1 inch (2.54 cm).

The second harmonic power was observed to be approximately 48 db lower than the power of the fundamental. The absence of odd harmonics was difficult to confirm experimentally since, for the small vanes, usually only the second harmonic was large enough to be de-tected by the Fourier analyzer on a logrithmic-magnitude power spectrum (maximum scale of 80 db). The db differences between the first and second harmonics, $20 \log_{10} (V_1/V_2)$, are plotted in Figure 4 for a variation of L/2 at this flow condition. For vane set A, at a mean velocity of 51.6 feet per second (15.72 meters per second), the optimum or maximum power difference is observed to be approximately 48 db and the smallest difference is 32 db. The power differences between the fundamental and third harmonic and between the fundamental and fourth harmonic were also noted, if measurable. In no case were they measured to be less than 60 db and 70 db respectively for the small vanes.

The power spectrum results for the larger vane sets were acceptable, but not as
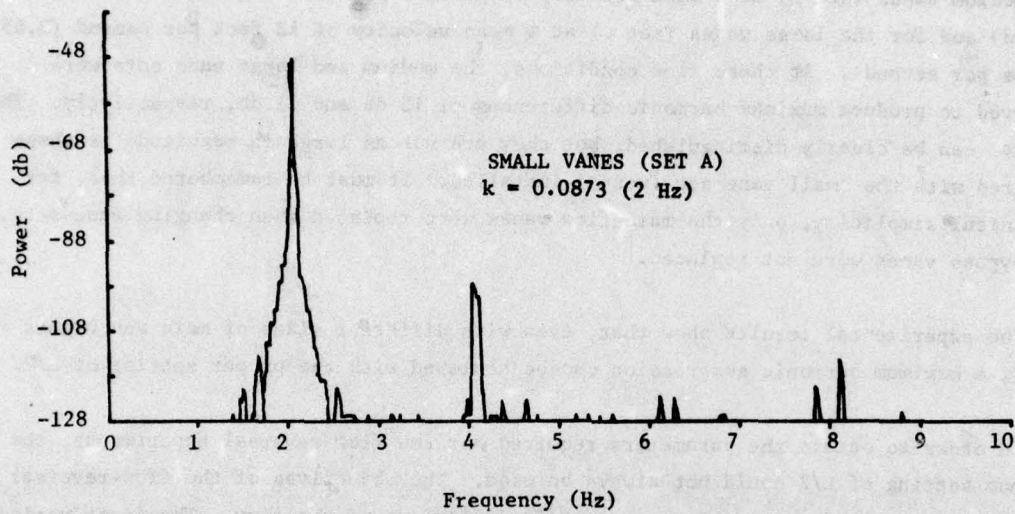
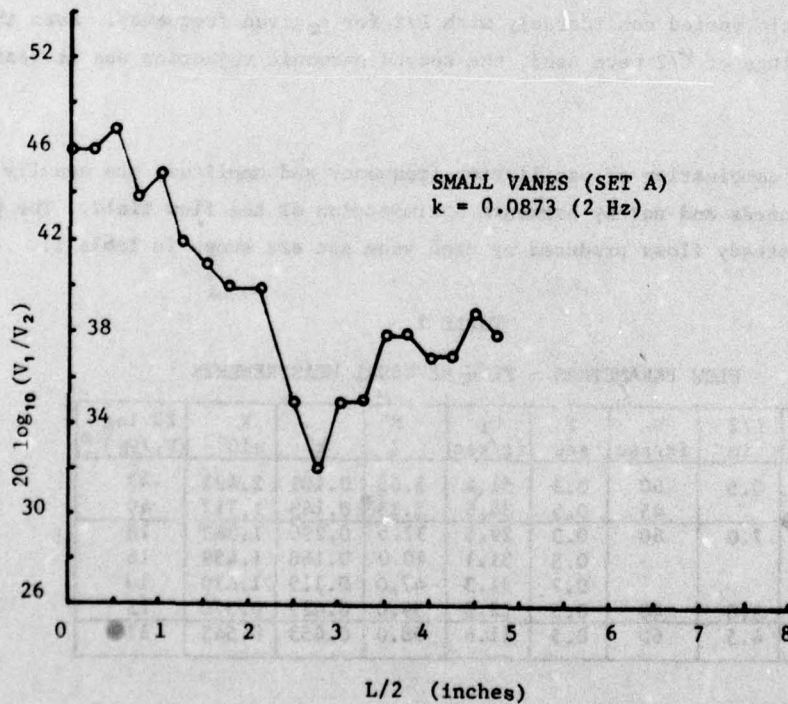Figure 3. Power Spectrum (AC)

Figure 4. Difference in First and Second Harmonic Power Levels

free from harmonics as those for the smallest vanes. The power differences between the
fundamental and second harmonic as functions of L/2 are presented in Figure 5 for both
the medium vanes (set B) at a mean velocity of 31 feet per second (9.45 meters per
second) and for the large vanes (set C) at a mean velocity of 12 feet per second (3.65
meters per second). At these flow conditions, the medium and large vane sets were
observed to produce maximum harmonic differences of 15 db and 11 db, respectively. The
maxima can be clearly distinguished, but they are not as large in magnitude as those
measured with the small vane set (set A) installed. It must be remembered that, for
mechanical simplicity, only the main-flow vanes were replaced when changing vane sets;
the bypass vanes were not replaced.

The experimental results show that, even with different sizes of main and bypass
vanes, a maximum harmonic suppression can be achieved with the proper setting of L/2.

In order to obtain the parameters required for the flow-reversal experiments, the
optimum setting of L/2 could not always be used. The objectives of the flow-reversal
experiments required two separate parametric variations of the flow. The first varied
the reduced frequency and held the mean velocity and oscillation amplitude nearly
constant. The second varied the oscillation amplitude, with the reduced frequency and
mean velocity almost constant. It was observed that the magnitudes of the mean velocity
and amplitude ratio varied considerably with L/2 for a given frequency. Even though
off-optimum settings of L/2 were used, the second harmonic rejection was at least 10 db
for all cases.

The required combination of oscillation frequency and amplitude are usually dictated
by experimental needs and not by harmonic optimization of the flow field. The para-
meters of the unsteady flows produced by each vane set are shown in Table 1.

TABLE 1

FLOW PARAMETERS - FLOW REVERSAL MEASUREMENTS

Vane Set	L/2 in	U_0 ft/sec	T sec	U_1 ft/sec	N %	k	R x10^5	20 log $(V_1/V_2)^{10}$
A	0.5	60	0.5	51.6	5.65	0.101	2.421	47
		45	0.5	36.6	5.15	0.143	1.717	49
B	7.0	60	0.3	29.5	37.5	0.296	1.383	18
			0.5	31.1	40.0	0.168	1.459	16
			0.7	31.3	47.0	0.119	1.470	10
	3.0	40	0.5	12.2	59.0	0.429	0.570	13
C	4.5	60	0.5	11.6	98.0	0.453	0.542	11

As an aside, it was found that harmonic optimization could also be confirmed using
the method of Charnay and Mathieu (Ref. 11) who measured the skewness and kurtosis
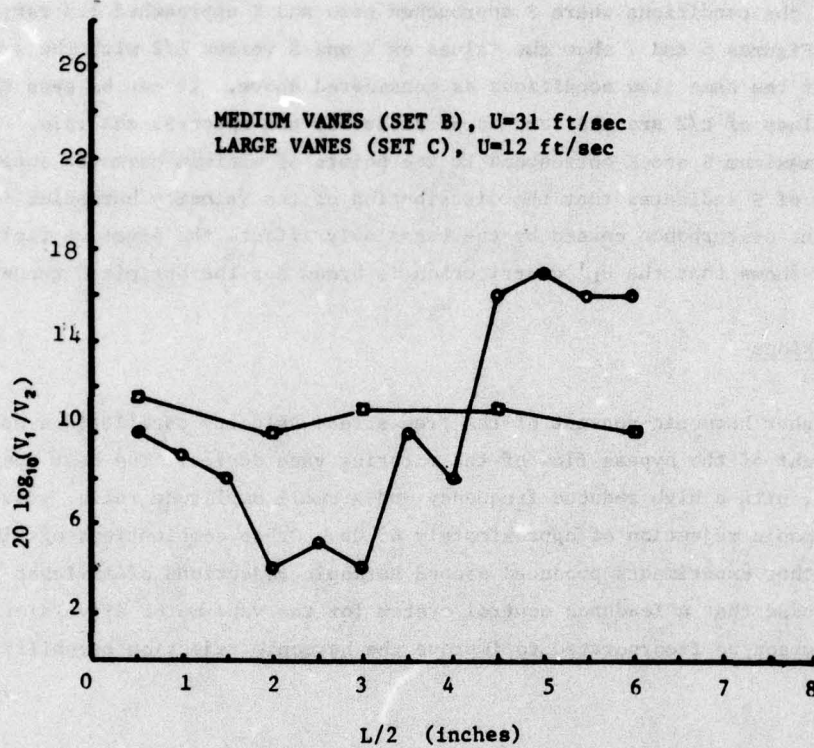of the longitudinal turbulent velocity component, u_1', in an oscillatory flow tunnel.

MEDIUM VANES (SET B), U=31 ft/sec
LARGE VANES (SET C), U=12 ft/sec

Figure 5. Difference in First and Second Harmonic Levels
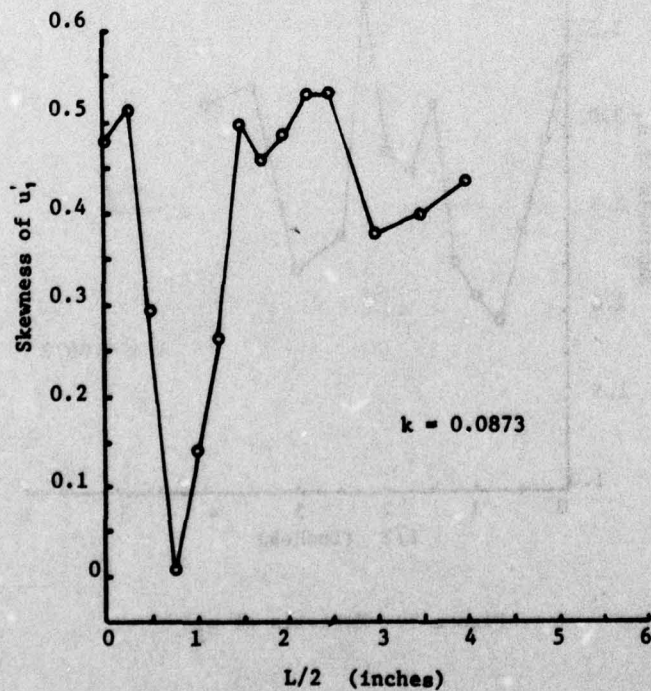
k = 0.0873

Figure 6. Skewness of u_1'

They found the conditions where S approached zero and K approached 1.5 represented an optimum. Figures 6 and 7 show the values of K and S versus L/2 with the small vanes (set A) for the same flow conditions as considered above. It can be seen that the optimum values of L/2 are the same as predicted by the spectral analysis. Also, the points of maximum S and K correspond to the points of minimum harmonic suppression. The zero value of S indicates that the distribution of the velocity harmonics is Gaussian and that the disturbance caused by the vanes only affects the pressure field. The low value of K shows that the u_1' distribution is broad for the optimized tunnel condition.

V. Conclusions

The higher harmonic content of the free stream velocity oscillations was reduced by adjustment of the bypass flow of the rotating vane device. The best operating conditions, with a high reduced frequency and a small amplitude ratio, provided a second harmonic rejection of approximately 48 db. Other combinations of flow parameters used for other experiments produced second harmonic rejections of at least 10 db. It is recommended that a feedback control system for the vane motor drive, similar to that used by Simpson, be incorporated to improve the harmonic rejection capability of this device.
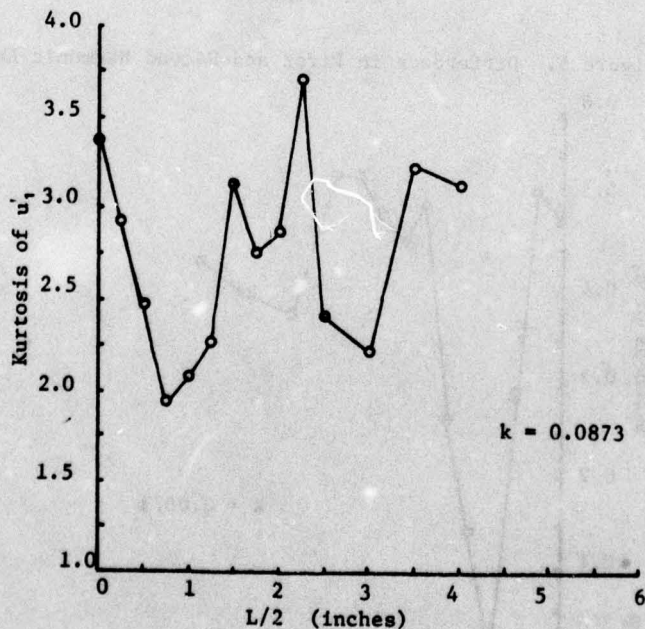

Figure 7. Kurtosis of u_1'

Symbols

$A(x)$	wind tunnel cross-section area, as a function of longitudinal distance
F_1	pressure drop coefficient across main-flow rotating vanes
F_2	pressure drop coefficient across bypass-flow rotating vanes
K	kurtosis factor of u_1', i.e., $\overline{(u_1'^4)}/\overline{(u_1'^2)^2}$
K_{mn}	pressure changes between wind tunnel stations m and n
$L/2$	width of top or bottom bypass port opening in the unsteady flow generator
N	oscillating velocity amplitude ratio, i.e., $N = \dfrac{\Delta U}{U_1} = \dfrac{(U_{maximum} - U_1)}{U_1}$
$Q(x,t)$	mass flow per unit volume, $A(x)u(x,t)$
Q_o	steady-flow mass flow per unit volume
Q_1	mass flow per unit volume through main-flow rotating vanes
Q_2	mass flow through bypass rotating vanes
R	Reynolds number, $\dfrac{U_1 \rho c}{\mu}$
R_1	sum of coefficients of viscous and pressure losses for flow through tunnel test section and main-flow vanes
R_2	sum of coefficients of viscous and pressure drop losses for flow through bypass ports and bypass vanes
R'	coefficient of viscous and pressure losses for identical main-flow and bypass rotating vanes
S	skewness factor of u_1', i.e., $\overline{(u_1'^3)}/\overline{(u_1'^2)}^{3/2}$
U_∞	free stream velocity (steady or oscillatory)
U_o	free stream velocity prior to operating unsteady flow device
U_1	mean value of oscillating longitudinal free stream velocity
V_1	voltage used to compute the power contained in the first harmonic of the velocity oscillation power spectrum
V_2	voltage used to compute the power contained in the second harmonic of the velocity oscillation power spectrum
$\langle V \rangle$	average voltage resulting from the ensemble average process
c	airfoil chord length
$f_1(t)$	unsteady component of pressure drop coefficient across main-flow rotating vanes
$f_2(t)$	unsteady component of pressure drop coefficient across bypass rotating vanes
$\bar{f}_1(t)$	nondimensional value of $f_1(t)$, i.e., $f_1/2R'$
$\bar{f}_2(t)$	nondimensional value of $f_2(t)$, i.e., $f_2/2R'$
k	reduced frequency, $\dfrac{\omega c}{2U_1}$
$q_1(t)$	unsteady component of $Q_1(x,t)$

113

$q_2(t)$ unsteady component of $Q_2(x,t)$

r^2 ratio of $R_1/R_2 = (Q_{20}/Q_{10})^{\frac{1}{2}}$

t time

u_1 velocity component in longitudinal direction

u_2 velocity component in vertical direction

x length dimension along longitudinal (axial) coordinate

$\underset{\sim}{x}$ position vector, $|\underset{\sim}{x}| = \sqrt{x^2 + y^2 = z^2}$

α_{mn} mass flow passing between wind tunnel stations m and n

β coefficient of fan pressure drop

$\gamma(x)$ coefficient of viscous losses

ΔP_f steady pressure drop across fan

ΔP_f unsteady pressure drop across fan

μ coefficient of viscosity of air

ρ air density

τ_1 time constant associated with area changes upstream of test section, i.e., α_1/RQ_o

τ_3 time constant associated with area changes downstream of test section, i.e., α_3/RQ_o

ϕ_1 vane rotation angle of main-flow vane

ϕ_2 vane rotation angle of bypass-flow vane

$(\bar{\ })$ denotes a time average

$\langle(\ )\rangle$ denotes an ensemble average

USAFA-TR-79-1

References

1. McCroskey, W. J., Philippe, J. J., "Unsteady Viscous Flow on Oscillating Airfoils," AIAA Journal, Vol. 13, No. 1, Jan 1975, pp. 71-79.

2. McCroskey, W. J., Carr, L. W., McAlister, K. W., "Dynamic Stall Experiments on Oscillating Airfoils," AIAA Journal, Vol. 14, No. 1, Jan 1976, pp. 57-63.

3. Despard, R. A., Miller, J. A., "Separation in Oscillating Laminar Boundary Layer Flows," Journal of Fluid Mechanics, Vol. 47, Part 1, 1971, pp. 21-31.

4. Saxena, L. S., Fejer, A. A., Morkovin, M. V., "Features of Unsteady Flows over Airfoils," Proc. AGARD Symp. on Unsteady Aerodynamics, Ottawa, Sep 26-28, 1972.

5. Retelle, John P., "Unsteady Boundary Layer Flow Reversal in a Longitudinally Oscillating Flow," Frank J. Seiler Research Laboratory SRL-TR-78-0006, August 1978.

6. Pierce, G. A., Kunz, D. L., Malone, J. B., "The Effect of Varying Freestream Velocity on Airfoil Dynamic Stall Characteristics," J. American Helicopter Society, April, 1978, pp. 27-33.

7. Despard, R. A., "Laminar Boundary Layer Separation in Oscillating Flow," Ph.D. Thesis, Naval Postgraduate School, June 1969.

8. Morkovin, M. V., Loehrke, R. I., Fejer, A. A., "On the Response of Laminar Boundary Layers to Periodic Changes in Freestream Speed," Proc. Symp. on Recent Research on Unsteady Boundary Layers, Quebec, 1972.

9. Karlsson, S.K.F., "An Unsteady Turbulent Boundary Layer," J. Fluid Mechanics, Vol. 5, 1959, p. 622.

10. Simpson, R. L., "Features of Unsteady Turbulent Boundary Layers as Revealed From Experiments," Proc. AGARD Symp. on Unsteady Aerodynamics, OHAWA, Sep 26-28, 1977.

11. Charnay, G., Mathieu, J., "Periodic Flow in a Wind Tunnel Produced by Rotating Shutters," J. Fluid Engineering, Trans. ASME, Ser. 1, Vol. 98, No. 2, Jun 1976, pp. 278-283.

12. Francis, M. S., "An Experimental Investigation of Wing Trailing Vortex Formation," Frank J. Seiler Research Laboratory TR-76-0013, August 1976.

13. McMichael, J. M., Private Communication, December 18, 1975.

APPENDIX

UNSTEADY FLOW ANALYSIS

The following is an analysis of an unsteady flow wind tunnel which has been adapted for the tunnel configuration described in Section II. Following the discussion of McMichael (Ref. 5), the momentum equation for the wind tunnel flow may be written.

$$\frac{\partial u}{\partial t} + u \frac{\partial u}{\partial x} = - \frac{\partial}{\partial x}\left(\frac{P}{\rho}\right) - \gamma(x) u^2 \tag{A1}$$

where $\gamma(x)$ represents losses due to the friction of the walls. The mass balance is:

$$Q(x,t) = A(x) u(x,t) \tag{A2}$$

where $A(x)$ is the local cross-sectional area. Substituting,

$$\frac{1}{A(x)} \frac{\partial Q}{\partial t} + \frac{Q^2}{2} \frac{\partial}{\partial x}\left(\frac{1}{A^2(x)}\right) + \frac{Q^2 \gamma(x)}{A^3(x)} = - \frac{\partial}{\partial x}\left(\frac{P}{\rho}\right). \tag{A3}$$

The wind tunnel stations and mass flows are defined in Figure 1. Integrating between arbitrary stations m and n yields:

$$(P_m - P_n) = \alpha_{mn} \frac{\partial Q}{\partial t} + K_{mn} Q^2 \tag{A4}$$

where:

$$\alpha_{mn} = \rho \int_m^n \frac{dx}{A(x)}$$

$$K_{mn} = \frac{P}{2}\left[\frac{1}{A^2(x)}\right]_m^n + P \int_m^n \left(\frac{\gamma(x)}{A^3(x)}\right) dx.$$

Knowing that $P_1 = P_8 = Pa$ (atmospheric pressure) and assuming quasi-steady, high Reynolds number flow, the pressure differences at each station are:

$$P_1 - P_2 = \alpha_{12} Q_1 + K_{12} Q_1^2$$

$$P_3 - P_4 = \alpha_{34} Q_1 + K_{34} Q_1^2 \tag{A5}$$

$$P_5 - P_6 = \alpha_{56} (\dot{Q}_1 + \dot{Q}_2) + K_{56} (Q_1 + Q_2)^2$$

$$P_7 - P_8 = \alpha_{78} \, (\dot{Q}_1 + \dot{Q}_2) + K_{78} \, (Q_1 + Q_2)^2$$

also:

$$P_2 - P_3 = C_{23} \, Q_1^2$$

$$P_4 - P_5 = C_{45} \, Q_1^2 \tag{A6}$$

$$P_4 - P_5 = C_{45} \, Q_2^2$$

where C_{mn} is the pressure drop coefficient across the indicated mechanical devices. Also:

$$P_6 - P_7 = - P_f \text{ (fan pressure rise).} \tag{A7}$$

Then, McMichael writes:

$$(P_1 - P_5) = (P_a - P_5) = (\alpha_{12} + \alpha_{34}) \, \dot{Q}_1 + (K_{12} + K_{34} + C_{23} + C_{45}) \, Q_1^2 . \tag{A8}$$

Now define

$$\alpha_1 = (\alpha_{12} + \alpha_{34})$$

$$K_1 = (K_{12} + K_{34} + C_{23})$$

$$F_1 = C_{45}$$

$$F_2 = C_{a5} .$$

Combining these terms gives

$$F_2 Q_2^2 = \alpha_1 \dot{Q}_1 + (K_1 + F_1) Q_1^2 . \tag{A9}$$

The adjustable bypass ports can be opened a distance L and essentially add a resistance $K_2(L)$ so that

$$P_a - P_5 = (K_2 + F_2)Q_2^2. \tag{A10}$$

Thus

$$(P_a - P_5) = (K_2 + F_2) Q_2^2 = \alpha_1 \dot{Q}_1 + (K_1 + F_1)Q_1^2. \tag{A11}$$

Note that $\alpha_2 Q_5$ was considered negligible because of the short distance between the by-pass port and bypass vanes. For the fan duct exit

$$(P_5 - P_a) = (P_5 - P_6) + (P_6 - P_7) + (P_7 - P_8)$$

$$= (\alpha_{56} + \alpha_{78}) (\dot{Q}_1 + \dot{Q}_2) + (K_{56} + K_{78}) (Q_1 + Q_2)^2 - P_f \tag{A12}$$

define

$$K_3 = K_{56} + K_{78}$$

$$\alpha_3 = \alpha_{56} + \alpha_{78}.$$

Collecting the previous relations yields

$$P_a - P_5 = \begin{cases} (K_2 + F_2) Q_2^2 \\ (K_1 + F_1) Q_1^2 + \alpha_1 \dot{Q}_1 \\ -K_3(Q_1 + Q_2)^2 - \alpha_3 (\dot{Q}_1 + \dot{Q}_2) + P_f, \end{cases} \tag{A13}$$

A reference state for the tunnel flow may be defined using the time average of the vane pressure drop coefficients and mass flows at a given mean tunnel velocity. Then,

$$F_1(t) = F_{10} + f_1(t)$$

$$F_2(t) = F_{20} + f_2(t)$$

$$Q_1(t) = Q_{10} + q_1(t)$$

$$Q_2(t) = Q_{20} + q_2(t)$$

118

where

$$\overline{F_1(t)} = F_{10}$$

$$\overline{F_2(t)} = F_{20}$$

$$\overline{Q_1(t)} = Q_{10}$$

$$\overline{Q_2(t)} = Q_{20}$$

and

$$\overline{f_1(t)} = \overline{f_2(t)} = \overline{q_1(t)} = \overline{q_2(t)} = 0$$

also,

$$P_f = P_{f_0} + \Delta P_f$$

and

$$\frac{q_1}{Q_{10}} \sim \frac{q_2}{Q_{20}} \sim \frac{\Delta P_f}{P_{f_0}} << 1.$$

The reference state (time average) of equation 13 shows

$$(K_2 + F_{20})Q_{20}^2 = (K_1 + F_{10})Q_{10}^2 \tag{A14}$$

$$(K_1 + F_{10})Q_{10}^2 = P_{f_0} - K_3(Q_{10} + Q_{20})^2. \tag{A15}$$

Equations (2), (3), and (4) are then linearized about the reference state (second-order terms dropped):

$$2(K_2 + F_{20})Q_{20} q_2 + f_2 Q_{20}^2 = 2(K_1 + F_{10})Q_{10} q_1 + f_1 Q_{10}^2 + \alpha_1 \dot{q}_1 \tag{A16}$$

$$2(K_2 + F_{20}) Q_{20} q_2 + f_2 Q_{20}^2 = \Delta P_f - \alpha_3(\dot{q}_1 + \dot{q}_2) - K_3(Q_{10} + Q_{20})(q_1 + q_2). \tag{A17}$$

For the simplified case where the main-flow and bypass vanes are identical, equations

119

(5) and (6) show that $F_{10} = F_{20} \equiv F_0$. To balance the reference state flow rates, K_2 is adjusted so that $K_1 = K_2$, so that $Q_{10} = Q_0/2$. Then define:

$$R_1 = K_1 + F_{10}$$

$$R_2 = K_2 + F_{20}$$

$$r = R_1/R_2$$

$$Q_{20} = rQ_{10} .$$

The equations (7) and (8) become:

$$2rR_2 Q_{10} q_2 + f_2 r^2 Q_{10}{}^2 = 2R_1 Q_{10} q_1 + f_1 Q_{10}{}^2 + \alpha_1 \dot{q}_1 \qquad (A18)$$

$$= \Delta P_f - \alpha_3 (\dot{q}_1 + \dot{q}_2) - 2K_3 Q_{10} (1 + r) (q_1 + q_2)$$

for simplification, ΔP_f may be approximated as

$$\Delta P_f \simeq \beta(q_1 + q_2) \qquad (A19)$$

where β is a constant. Equation (9) may be non-dimensionalized using

$$R_1 = R_2 = R'$$

$$\hat{f}_1 = f_1/2R'$$

$$\hat{f}_2 = f_2/2R'$$

$$\hat{q}_1 = q_1/(Q_0/2)$$

$$\hat{q}_2 = q_2/(Q_0/2)$$

which gives

$$2\hat{q}_2 + 2\hat{f}_2 = 2\hat{q}_1 + 2\hat{f}_1 + \frac{2\alpha_1}{RQ_0} \dot{\hat{q}}_1 =$$

$$= \frac{2\beta}{RQ_0} (\hat{q}_1 - \hat{q}_2) - \frac{2\alpha_3}{RQ_0} (\dot{\hat{q}}_1 - \dot{\hat{q}}_2) - \frac{2K_3}{R} (\hat{q}_1 + \hat{q}_2) \tag{A20}$$

Now define the time constants

$$\tau_1 = \frac{\alpha_1}{RQ_0}, \qquad \tau_3 = \frac{\alpha_3}{RQ_0}$$

and also let

$$G = \frac{\beta}{RQ_0} - \frac{K_3}{R}.$$

Substituting gives

$$\tau_1 \tau_3 \ddot{\hat{q}}_1 + [\tau_1(1-G) + 2\tau_3]\dot{\hat{q}}_1 + (1-2G)\hat{q}_1$$

$$= G(\hat{f}_1 - \hat{f}_2) - \tau_3(\dot{\hat{f}}_1 - \dot{\hat{f}}_2), \tag{A21}$$

The damping ratio for this second order system is

$$\zeta = \frac{(1-G)\tau_1 + 2\tau_3}{2\sqrt{(1-G)\tau_1\tau_3}} \tag{A22}$$

and the resonant frequency is

$$\omega_0 = \frac{\sqrt{1-2G}}{\sqrt{\tau_1\tau_3}} = \frac{RQ_0\sqrt{1-2G}}{\sqrt{\alpha_1\alpha_3}} \tag{A23}$$

It can also be shown that these small vanes of set A ideally generate only even harmonics in the velocity field. Equation (21) shows that the forcing function is $(\hat{f}_1 - \hat{f}_2)$. McMichael shows the angular dependence between the two sets of vanes to be

$$2\phi_1 = \omega t + \pi/2$$

$$2\phi_2 = \omega t - \pi/2.$$

For a given vane resistance function

$$\hat{f}(\phi) = \frac{a_o}{2} + \sum_{n=1}^{\infty} a_n \cos (2n\phi) \qquad (A24)$$

it can be seen that

$$\hat{f}_1(\phi_1) + \hat{f}_2(\phi_2) = \frac{a_o}{2} + \sum_{n=0,2,4,\ldots}^{\infty} a_n \cos \left(n(\omega t + \pi/2) \right) \qquad (A25)$$

and

$$\hat{f}_1(\phi_1) - \hat{f}_2(\phi_2) = \sum_{n=1,3,5,\ldots}^{\infty} a_n \cos \left(n(\omega t - \pi/2) \right) \qquad (A26)$$

The forcing function $(f_1 - f_2)$ in the dynamic equation thus ideally only contains odd harmonics. This was difficult to determine experimentally since, for the small vanes, usually only the second harmonic was of a large enough amplitude to be detected by the Fourier analyzer on a logrithmic-magnitude power spectrum (maximum scale of 80 db). The equations cannot be so easily simplified for the situation where the main-flow vanes and bypass vanes are different, because $F_{10} \neq F_{20}$ and $K_1 \neq K_2$. The first line of equation (9) may then be written (including the assumption for ΔP_f):

$$q_2 = A'f_1 - B'f_2 + C'\dot{q}_1 + D'q_1 \qquad (A27)$$

where

$$A' = Q_{10}/(2rR_2)$$

$$B^1 = rQ_{10}/(2R_2)$$

$$C' = \alpha_1/(2rR_2Q_{10})$$

$$D' = r.$$

Substituting expression (B-11) into the second line of equation (B-8) yields:

$$q_1 \left[\frac{\alpha_2 \alpha_1}{2rR_2Q_{10}} \right] + \dot{q}_1 \left[\alpha_1 \left(1 + \frac{2K_3(1+r)Q_{10} - \beta}{2rR_2Q_{10}} \right) + \frac{\alpha_2\alpha_4}{2rR_2Q_{10}} + \alpha_3 \right]$$

$$+ q_1 \left[2r^2 R_2 Q_{10} - \beta(1+r) + 2K_3 Q_{10} (1+r)^2 \right].$$

$$= -\alpha_3 \dot{f}_1 + \dot{f}_2 \left[\frac{\alpha_3 r Q_{10}}{2R_2} \right] + \frac{f_1}{2rR_2} \left[\beta Q_{10} - 2K_3 Q_{10}^2 (1+r) - 2rR_2 Q_{10}^2 \right]$$

$$+ \frac{f_2}{2R_2 r} \left[2K_3 Q_{10}^2 (1+r)r^2 - Br^2 \right] \tag{A28}$$

The effect of the variable bypass, through R_2, is seen to affect each term of equation (A28).

SECTION V

ENGINEERING EDUCATION

CONFIDENCE IN FUNDAMENTALS

Roger W. Gallington[*]

Abstract

The technical performance of recent engineering graduates may be limited by a lack of
confidence in fundamentals. This contention is supported here by three real engineering
problems requiring only undergraduate knowledge for their solutions, which the author
doubts many recent graduates could solve with sufficient confidence to direct the activ-
ities of others to implement the solutions. A means of building confidence during edu-
cational programs by systematic comparisons between different approaches to the same
problem is suggested.

I. Introduction

Many engineering educators comment that the graduates are increasingly unable to

solve the technical problems they face after leaving the educational institution. I

believe there are two reasons for this trend. The first reason is that faculties are

becoming more isolated from industry and, consequently, the new graduate simply does not

have an appropriate background. The second reason is that, because of the lack of

specific experiences in his education, the new graduate does not have sufficient confi-

dence in the fundamentals of his field. This paper addresses the second reason.

A lack of confidence in fundamentals may be limiting the technical performance of our

graduates.

To illustrate the importance of specific experiences in building confidence, I will

describe three practical engineering problems I have solved since my assignment to the

Academy. None of these problems is especially difficult and none requires technical

information beyond that taught in the typical modern undergraduate Aeronautical Engineer-

ing program. Confidence in these solutions is based on specific past experiences. As

you read through these examples ask yourself what fraction of recent graduates could

correctly work these problems without assistance and be confident enough of their answers

to direct the activities of technicians in implementing the solutions. I have pondered

this question and think the fraction must be very low. Herein lies a major challenge in

---

[*]Lt Col, USAF, Associate Professor of Aeronautics, DFAN

engineering education. How do we increase the students' confidence in their fundamental technical education? After the example problems, suggestions for building technical confidence are made.

II. Some Real Engineering Problems

These three problems are real in every sense of the word. They are facilities oriented simply because facilities happen to be my present responsibility. However, similar practical problems occur in all types of engineering including the most sophisticated research and development. In fact, inability to correctly and quickly solve problems of this sort can cause major and unnecessary slippage in programs intending to address much more challenging technical issues.

A. Turning Vane Problem

A bearing failed in the subsonic wind tunnel. During the repair operation it was necessary to cut a turning vane (several of these are located in each corner of a wind tunnel circuit) in two places. It was obvious to the technicians that future repairs would be easier if during the re-assembly the turning vane was bolted together instead of being welded. Welding would return the vane to its original strength whereas the bolted
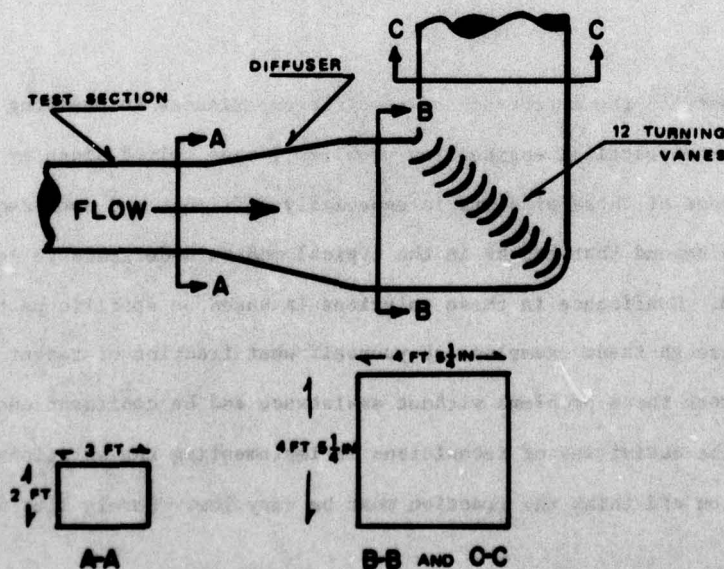

Figure 1. Wind Tunnel Geometry

126

vane would be weaker. The question for the engineer was whether to allow the bolted repair or to require welding.

1. Given:

The geometry of the relevant part of the wind tunnel and needed dimensions were all available from the construction drawings shown in Figure 1. The maximum achievable velocity in the test section is 400 ^{ft}/sec, and the density of air at the Air Force Academy is about 0.0018 ^{slg}/ft³ .
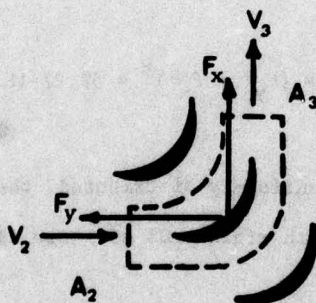
2. Find:

The air load on the turning vane.

Figure 2. Control Volume

3. Solution:

Draw the control volume shown in Figure 2. Assume that the row of turning vanes approximates a perfect two-dimensional cascade so that the pressures on the two curved stream surfaces of the control volume balance each other. Further, assume that the flow is incompressible, uniform across the inlet and outlet areas of the control volume, and attached to the tunnel walls and turning vanes. The continuity equation was applied between station 1 and 2 and stations 2 and 3 yielding:

$$V_2 = V_3 = \frac{A_1}{A_3} V_1 = \frac{6}{19.69} \times 400 = 121.88 \frac{ft}{sec} . \tag{1}$$

Bernouli's equation was applied to the flow through the turning vanes, showing that the pressures on the inlet and outlet areas were equal and, therefore, balanced. The two remaining components of the momentum equation became

$$F_x = \rho\, V_3^2\, A_3 \Big/ n + 1 = 0.0018 \times (121.88)^2 \times \frac{19.69}{13} = 40.50 \text{ lbf} \tag{2}$$

and

$$F_y = \rho\, V_2^2\, A_2 \Big/ n + 1 = 40.50 \text{ lbf} \tag{3}$$

where n is the number of turning vanes and n + 1 is the number of channels.

The total force becomes

$$F_{TOT} = (F_y^2 + F_x^2)^{\frac{1}{2}} = 57.27 \text{ lbf} \quad . \tag{4}$$

Since the load was assumed to be uniformly distributed, the loading could be described as that of a uniformly loaded beam with rigid ends as shown in Figure 3.
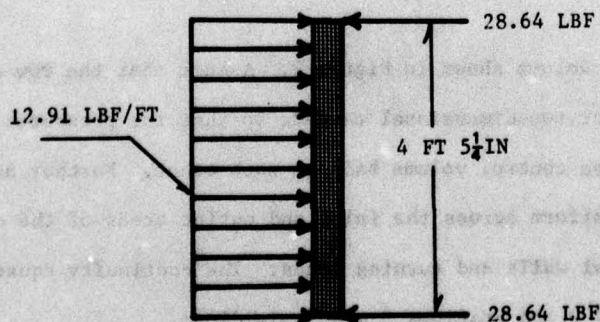

Figure 3. Load on Turning Vane

128

Having found the load to be small, approval was given for the bolted repair. After the turning vane was re-installed and before the tunnel was operated, the total calculated load was applied to the center of the vane. (This loading condition is more severe than the calculated one). The vane deflection was negligible.

The tunnel was carefully run up to its top speed, verifying both the bearing repair and the adequacy of the bolted turning vane.

B. Wind Tunnel Blow-Down Problem

The two large (200 horsepower, 600 psig) air compressors which normally supply air to the supersonic wind tunnel were being repaired. Due to contractural and funding difficulties it was obvious that they would be inoperative for some time. The tunnel is of the blow-down type (meaning that the compressors charge large air storage tanks and the tunnel is subsequently run by rapidly depleting the stored air). The question was: Could the tunnel be operated to complete two cadet projects during the current semester by using a five-horsepower compressor capable of delivering air at 110 psig? Suprisingly enough the answer was yes. The details follow.
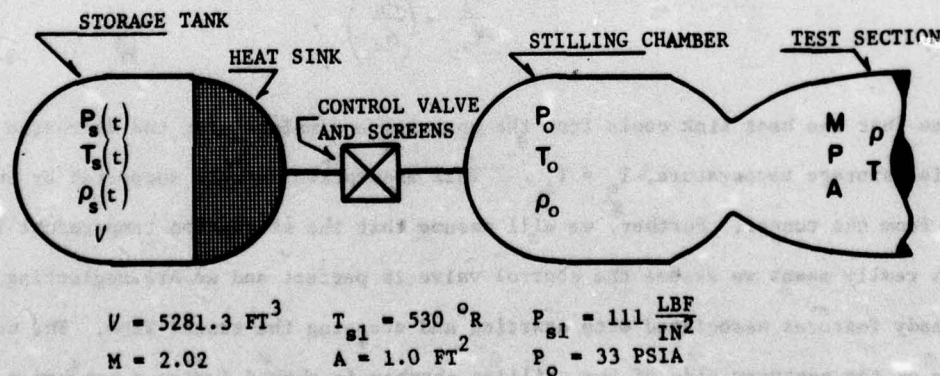

$$V = 5281.3 \text{ FT}^3 \qquad T_{s1} = 530 \text{ }^\circ R \qquad P_{s1} = 111 \frac{\text{LBF}}{\text{IN}^2}$$
$$M = 2.02 \qquad A = 1.0 \text{ FT}^2 \qquad P_o = 33 \text{ PSIA}$$

Figure 4. Blow-Down Tunnel Schematic

1. **Given:**

A schematic of the parts of the system essential to the solution is shown in Figure 4.
The following are fixed by the hardware and the working gas:

volume of storage tanks, $V = 5218.3$ ft^3

area of test section, $A = 1$ ft^3

gas constant, $R = 1715 \dfrac{\text{ft-1bf}}{\text{slug}^\circ\text{R}}$

ratio of specific heats, $\gamma = 1.4$

2. **Find:**

The available test time as a function of test Mach number, initial storage pressure
and temperature, and tunnel total pressure.

3. **Assumptions:**

A series of assumptions leads to an easy and accurate solution.
Assume that the air in the tank expands isentropically causing the pressure and the
density to be related by

$$\frac{P_s}{P_{s_1}} = \left(\frac{\rho_s}{\rho_{s_1}}\right)^\gamma. \tag{5}$$

Assume that the heat sink cools from the upstream end, maintaining the discharge at the
initial storage temperature, $T_o = T_{s_1}$. This assumption is well supported by experimental
data from the tunnel. Further, we will assume that the stagnation temperature is constant,
which really means we assume the control valve is perfect and we are neglecting the
unsteady features associated with starting and stopping the tunnel flow. The control
valve on the upstream side of the stilling chamber is choked during a run, and a run ends
when this ceases to be true.

4. Solution:

For quasi-steady flow the negative rate of change of mass in the storage tanks must equal the mass flow rate through the test section by conservation of mass:

$$-V \frac{d\rho_s}{dt} = \rho \ VA = \frac{\rho}{\rho_o} \ \rho_o \ (\gamma \ RT)^{\frac{1}{2}} \ MA$$

$$= \left(\frac{\rho}{\rho_o}\right) \rho_o \left[\left(\frac{T}{T_o}\right)_1 \gamma \ RT_o \right]^{\frac{1}{2}} MA \tag{6}$$

$$-V \frac{d\left(\rho_s / \rho_{s_1}\right)}{dt} = \left(\frac{\rho}{\rho_o}\right)\left(\frac{\rho_o}{\rho_{s_1}}\right)\left[\left(\frac{T}{T_o}\right) \gamma \ RT_o\right]^{\frac{1}{2}} MA \tag{7}$$

Using the perfect gas law and the energy equation, Eqn (7) becomes

$$-V \frac{d\left(\rho_s / \rho_{s_1}\right)}{dt} = \left(\frac{\rho}{\rho_o}\right) \frac{P_o}{R \ T_o} \frac{R \ T_{s_1}}{P_{s_1}} \left[\left(\frac{T}{T_o}\right) \gamma \ RT_{s_1}\right]^{\frac{1}{2}} MA \tag{8}$$

and integrating, yields:

$$-V \int_1^{\rho_s / \rho_{s_1}} d\left(\rho_s / \rho_{s_1}\right) = \frac{\rho}{\rho_o} \frac{P_o}{P_{s_1}} \left[\left(\frac{T}{T_o}\right) \gamma \ RT_{s_1}\right]^{\frac{1}{2}} MA \int_0^t dt \tag{9}$$

$$V \left(1 - \frac{\rho_s}{\rho_{s_1}}\right) = \left(\frac{\rho}{\rho_o}\right)\left(\frac{P_o}{P_{s_1}}\right)\left[\left(\frac{T}{T_o}\right) \gamma \ RT_{s_1}\right]^{\frac{1}{2}} MAt \tag{10}$$

or rearranging,

$$\frac{t\left(\gamma \ RT_{s_1}\right)^{\frac{1}{2}} A}{V} = \left(\frac{\rho_o}{\rho}\right)\left(\frac{T_o}{T}\right)^{\frac{1}{2}}\left(\frac{P_{s_1}}{P_o}\right) \left(1 - \frac{\rho_s}{\rho_{s_1}}\right) \frac{1}{M} \ . \tag{11}$$

If we now apply the isentropic relation between pressure and density in the storage tank, Eqn (11) becomes

$$\frac{t\left(\gamma\ RT_{s_1}\right)^{\frac{1}{2}}A}{V} = \left(\frac{\rho_o}{\rho}\right)\left(\frac{T_o}{T}\right)^{\frac{1}{2}}\frac{P_{s_1}}{P_o}\left[1 - \left(\frac{P_s}{P_s}\right)^{\frac{1}{\gamma}}\right]\frac{1}{M} \quad . \tag{12}$$

At the final time (end of the run) the flow between the storage tank and the stilling chamber is barely choked, which means at t_f

$$P_s = P_o\left(1 + \frac{\gamma-1}{2}\right)^{\frac{\gamma}{\gamma-1}} = P_o\left(\frac{\gamma+1}{2}\right)^{\frac{\gamma}{\gamma-1}} \quad . \tag{13}$$

Substituting into Eqn (12) yields

$$\frac{t_f\left(\gamma\ RT_{s_1}\right)^{\frac{1}{2}}A}{V} = \frac{1}{M}\left(1 + \frac{\gamma-1}{2}M^2\right)^{\frac{\gamma+1}{2(\gamma-1)}}\frac{P_{s_1}}{P_o}\left[1 - \left(\frac{P_o}{P_{s_1}}\right)^{\frac{1}{\gamma}}\left(\frac{\gamma+1}{2}\right)^{\frac{1}{\gamma-1}}\right]. \tag{14}$$

By making the appropriate substitutions of M = 2.02, P_{s_1} = 111 psia, P_o = 33 psia, and T_{s_1} = 530°R, the available test time per compressor pumping was found to be 15.75 seconds. Since only force data was required on the cadet projects, the time was adequate.

This solution is especially gratifying because by running the tunnel we were able to compare the actual run time with that computed using Eqn (14). This comparison is shown in Figure 5. The actual test time is seen to be within a fraction of a second of the calculated time.

Another calculation had to be made to determine the time required to charge the storage tanks to 110 psig given the substitute compressor first-stage cylinder displacement and the compressor's rotational speed. Can your students do this one?

C. Stagnation Pressure Controller Design

The trisonic tunnel has operated since 1958 with manual control of the stagnation pressure. During the years, some components of an automatic system have been acquired. Completion of the system has become essential to reduce the total pressure fluctuations in the tunnel by an order of magnitude and make the trisonic tunnel perform up to standards.
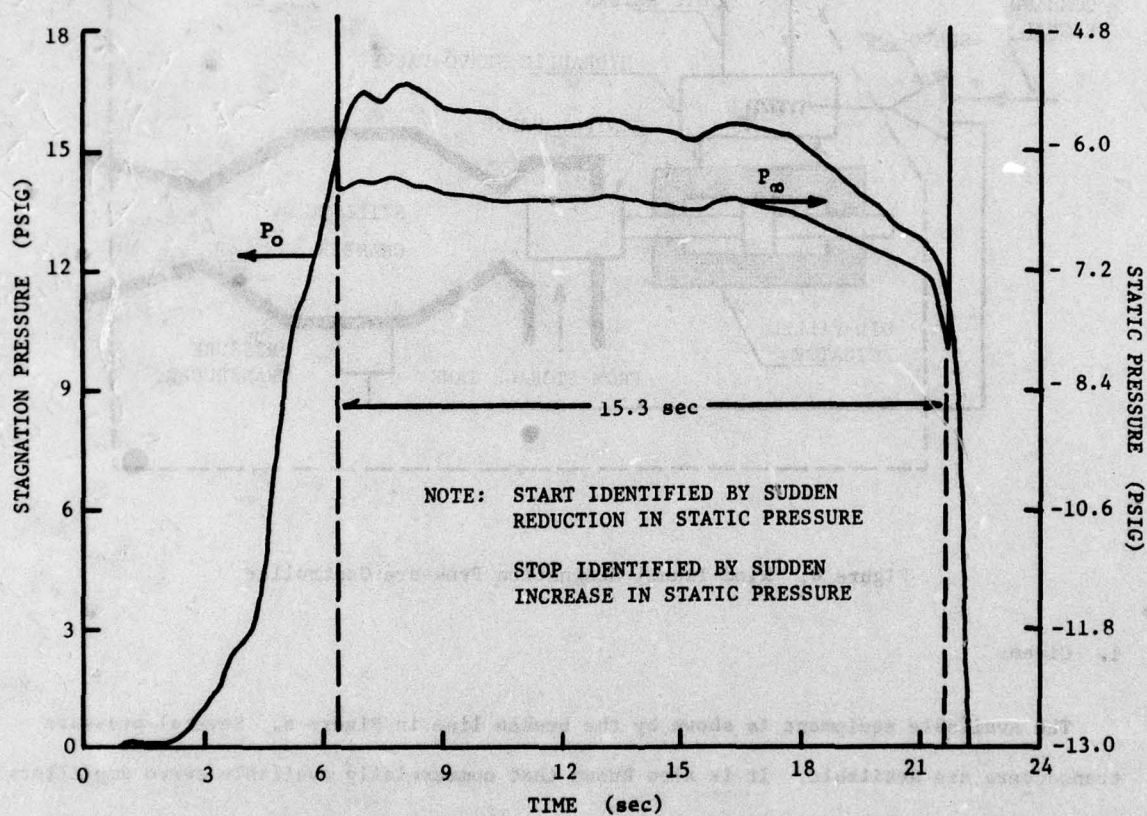
132

Figure 5. Blow-Down Tunnel Run Time

Several components of the system are on hand, and the engineers problem is to
select the remaining components to complete the system. Again, the details follow. In
this case it was necessary to delete some of the secondary calculations supporting the
assumptions and present results for only one Mach number to fit the solution into a
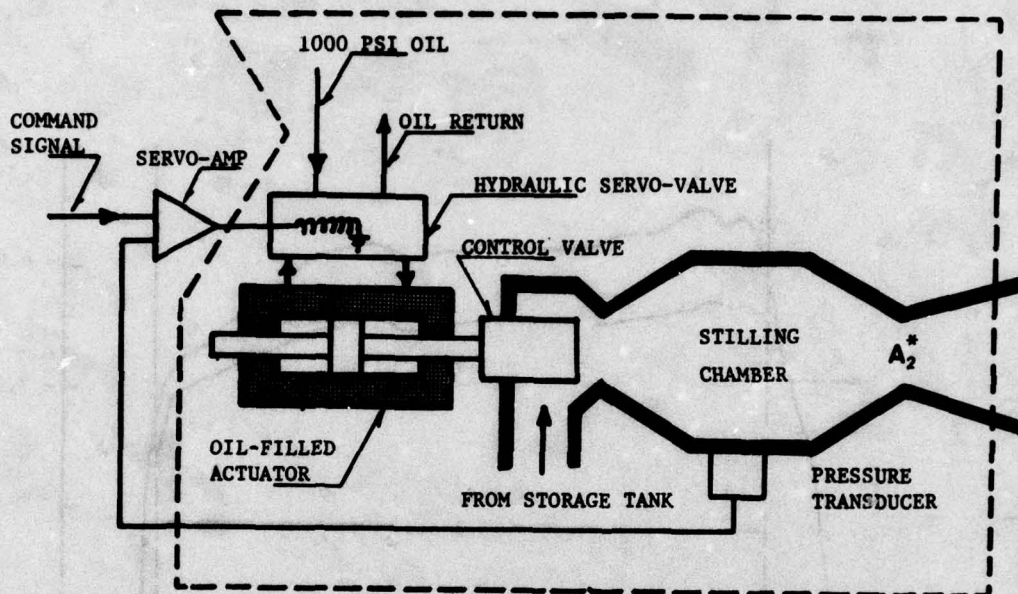concise presentation.

Figure 6. Wind Tunnel Stagnation Pressure Controller

1. Given:

The available equipment is shown by the broken line in Figure 6. Several pressure transducers are available. It is also known that commercially available servo amplifiers have gains from 2.5 to 250 milli-amps per volt. The important parameters are:

gain of hydraulic servo valve $K_q = \dfrac{5}{15} \dfrac{Gal}{Min \cdot MA}$

piston area of hydraulic actuator $A = 10.16 \ in^2$

area of open control valve $A^*_{1_{max}} = 81 \ in^2$

stroke of valve and actuator $x_{max} = 6 \ in$

gain of control valve $\approx \dfrac{A^*_{1_{max}}}{x_{max}}$ $K_{ax} = 1.33 \ in$

volume of stilling chamber $V = 27 \ ft^3$

134

area of throat at M = 4.5 $\qquad$ $A_2^* = \frac{1}{16.56} \text{ ft}^2$

nominal storage pressure $\qquad$ $P_{s_1} = 611 \text{ psia}$

gain of commercial servo-amp $\qquad$ $K_{sa} = 2.5\text{-}250 \frac{\text{ma}}{\text{V}}$

2. Find:

The engineering problem is to determine the proper gain of the pressure transducer
to achieve the tightest possible control without oscillation.

3. Solution:

The first step is to estimate the time constants associated with the response of:
(1) the valve-body/oil-filled actuator, (2) the servo-valve, (3) the transducer, (4)
stilling chamber pressure (to a change in valve position), and (5) the change in pressure
in the storage tanks. Without proof, the conclusion of these estimates is that the valve
body, servo-valve, and transducer are all very fast compared to the response of stilling
chamber pressure to a change in valve position. The response of stilling chamber pressure
to valve position is very fast compared to the slow decay of pressure in the tanks.
Therefore, it is appropriate to consider the transducer and servo-valve to be essentially
instantaneous and to neglect mechanical vibration of the valve body/actuator. It is
also appropriate to assume the supply pressure to be constant for purposes of estimating
the remaining required gains. It is a fact that the tank pressure does slowly
decrease causing the actual stagnation pressure, P_o , to be slightly less than the
commanded pressure, P_{o_c} . This slight difference between commanded and actual pressure
causes the servo-amp to have a small output, causing the servo valve to pass some oil;
this, then, causes the valve to open slowly as the run progresses. After an appropriate
feedback gain is found, it is a straightforward problem to estimate the pressure differ-
ence required to drive the valve at the velocity required to maintain constant stagnation
pressure. This calculation uses the same basic approach as in the previous problem and
will not be done here.

This long list of results, then, brings us to the problem an undergraduate should be able to solve. Find the proper gain to make the system stable and non-oscillitory. Figure 7 shows the idealized feedback loop to be analyzed. In that loop, note that the actuator contributes to the dynamics of the system because the output of the actuator is proportional to the input integrated over time. Clearly the transfer function $P_o(s)/A_1^*(s)$ is a key to this problem.
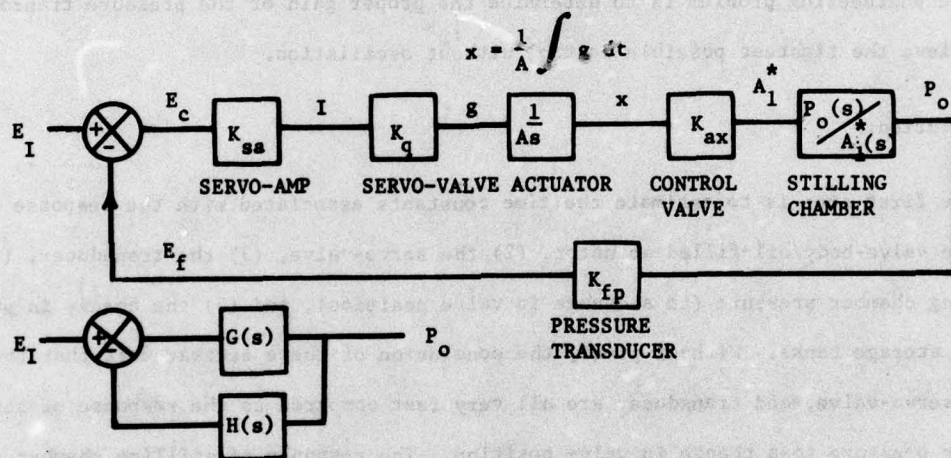

Figure 7. Idealized Feedback Loop

The mass flow rate into the stilling chamber is given by

$$\dot{m}_1 = A_1^* \frac{P_s \sqrt{\gamma}}{\sqrt{RT_o}} \left(\frac{2}{\gamma+1}\right)^{\frac{\gamma+1}{2(\gamma-1)}} \tag{14}$$

The mass flow rate out of the stilling chamber is given by

$$\dot{m}_3 = A_2^* \frac{P_o \sqrt{\gamma}}{\sqrt{RT_o}} \left(\frac{2}{\gamma+1}\right)^{\frac{\gamma+1}{2(\gamma-1)}} \tag{15}$$

If we differentiate the perfect gas law, $P_o = \rho_o RT = \frac{M}{V} RT_o$, and substitute, i.e.

$$\frac{dP_o}{dt} = \frac{dM}{dt} \frac{RT_o}{V} = \frac{(\dot{m}_1 - \dot{m}_2) RT_o}{V} \tag{16}$$

or,

$$\frac{dP_o}{dt} = \frac{P_s A_1^* - P_o A_2^*}{V} \left(\gamma RT_o \right)^{\frac{1}{2}} \left(\frac{2}{\gamma+1} \right)^{\frac{\gamma+1}{2(\gamma-1)}} \tag{17}$$

Put the differential equation in standard form,

$$\frac{dP_o}{dt} + P_o \frac{A_2^*}{V} \left(\gamma RT_o \right)^{\frac{1}{2}} \left(\frac{2}{\gamma+1} \right)^{\frac{\gamma+1}{2(\gamma-1)}}$$

$$= P_s A_1^* \left(\gamma RT_o \right)^{\frac{1}{2}} \left(\frac{2}{\gamma+1} \right)^{\frac{\gamma+1}{2(\gamma-1)}} \tag{18}$$

Take the Laplace transform,

$$\left[s + \frac{A_2^* \left(\gamma RT_o \right)^{\frac{1}{2}}}{V} \left(\frac{2}{\gamma+1} \right)^{\frac{\gamma+1}{2(\gamma-1)}} \right] P_o(s)$$

$$= \frac{P_s \left(\gamma RT \right)^{\frac{1}{2}}}{V} \left(\frac{2}{\gamma+1} \right)^{\frac{\gamma+1}{2(\gamma-1)}} A_1^*(s) \tag{19}$$

And the sought-after transfer function is

$$\frac{P_o(s)}{A_1^*(s)} = \frac{\dfrac{P_s \left(\gamma RT_o \right)^{\frac{1}{2}}}{V} \left(\dfrac{2}{\gamma+1} \right)^{\frac{\gamma+1}{2(\gamma-1)}}}{s + \dfrac{A_2^*}{V} \left(\gamma RT_o \right)^{\frac{1}{2}} \left(\dfrac{2}{\gamma+1} \right)^{\frac{\gamma+1}{2(\gamma-1)}}} \left[\frac{\text{psi}}{\dfrac{\text{in}^2 \ \text{sec}}{1/\text{sec}}} \right] \quad . \tag{20}$$

Further, if we let

$$\frac{1}{\tau} = \frac{A_2^*}{V} \left(\gamma\, RT_o \right)^{\frac{1}{2}} \left(\frac{2}{\gamma+1} \right)^{\frac{\gamma+1}{2(\gamma-1)}} = \frac{1}{0.7 \text{ sec}} \tag{21}$$

then

$$\frac{P_o(s)}{A_1^*(s)} = \frac{\dfrac{P_s}{A_2^*} \dfrac{1}{\tau}}{\left(s + \dfrac{1}{\tau} \right)} \tag{22}$$

The forward transfer function then becomes

$$G(s) = \frac{K_{sa}\, K_q\, K_{sx} \dfrac{P_s}{A_2^*} \dfrac{1}{\tau}}{A\, s \left(s + \dfrac{1}{\tau} \right)} \tag{23}$$

and the feedback transfer function becomes

$$H(s) = K_{fp} .$$

$$H(s)\, G(s) = \frac{K_{sa}\, K_q\, K_{ax} \dfrac{P_s}{A_2^*} \dfrac{1}{\tau}\, K_{fp}}{A\, s \left(s + \dfrac{1}{\tau} \right)} = \frac{K}{s \left(s + \dfrac{1}{\tau} \right)} \tag{24}$$

The closed-loop transfer function becomes

$$\frac{P_o(s)}{E_I(s)} = \frac{G(s)}{1 + G(s)\, H(s)} \tag{25}$$

Therefore, we want to find the valve of the loop gain K such that
the roots of the equation,

$$1 + G(s)\, H(s) = 0 , \tag{26}$$

just lie on the negative real axis so that any increase in K will cause them to have imaginary parts. Combining Eqn (23) and (24) into Eqn (26) gives

$$s^2 + \frac{s}{\tau} + K = 0 \tag{27}$$

For $K = \frac{1}{4\tau^2}$ this becomes a perfect square leading to equal, real negative roots.

$$\left(s + \frac{s}{\tau} + \frac{1}{4\tau^2}\right) = \left(s + \frac{1}{2\tau}\right)^2 \tag{28}$$

Increasing the gain above $K = \frac{1}{4\tau^2}$ leads to a pair of complex conjugate roots and an oscillating solution. Reducing the gain below $K = \frac{1}{4\tau^2}$ gives less than achievable performance.

Now Equation (24) is used to find the minimum required gain for the pressure transducer. If a transducer with greater than the minimum gain is available, then no other amplifiers other than the servo-amplifier are required.

$$K_{sa} \, K_q \, K_{gx} \, \frac{P_s}{A_s^*} \, \frac{1}{\tau} \, K_{fp} = \frac{1}{4\tau^2} = K$$

Pressure transducers with

$$\tag{29}$$

$$K_{fp} = 0.000015 \, \frac{volt}{psi} = 0.015 \, \frac{mv}{psi}$$

or greater are readily available in the laboratory and, therefore, the only new equipment required is the servo-amplifier.

III. What Experiences Build Confidence?

How can we build technical confidence in our students? To answer this question I turned a bit introspective and asked how I knew each of the above solutions would work. The answer is experience - not years of it - but specific experiences that built confidence in each of the analytical techniques used.

The turning vane problem reminded me of a 1959 mechanical engineering laboratory experiment that was part of a required course which I detested. After all, I aspired to be a theoretician and a researcher, and knowledge of the torque of a Pelton Wheel (an impulse water turbine) could hardly contribute to this lofty goal. I did remember, however, that the calculated torque and the measured torque were within a few percent of each other. The calculation was based on the momentum equation — the same principle applied to the turning vane problem.

The wind tunnel blow-down time problem exercised considerable knowledge of compressible flow and basic thermodynamics. Several physical observations supported confidence in this solution. The detested mechanical engineering laboratory had examples of airflow measurement with choked and un-choked nozzles, and I recalled that the correction to the theoretical calculations were on the order of 2-5%. Another feature of the blowdown time problem is that it is fundamentally unsteady, and an assumption of quasi-steady flow had to be made to get the solution. My confidence that this assumption was adequate was based on a single homework problem in Shapiro which showed, when properly worked, that the unsteady terms are only important when a significant fraction of the flow has kinetic energy.

In the stagnation pressure control problem, confidence in the linearized analysis and the use of Laplace Transforms dates from a 1963 course in analog computing at the University of Arkansas Graduate Institute of Technology (a city extension campus located in Little Rock). In that course we modeled many different systems, both linear and non-linear systems. The observation that the behavior of a non-linear system around the operating point is very closely predicted by the linear system gives me absolute confidence that selection of equipment based on this analysis of the trisonic tunnel will yield an adequate controller.

Since the earliest confidence-building experiences, many engineers have had reinforcing experiences which maintained confidence in fundamentals. However, it was these first verifications of the fundamentals that started the confident assault on problems of increasing difficulty.

IV. Suggestions for Preparation of Course Material

The critical first impression of new technical material is always based on at least one comparison. Possible candidates for comparisons are: (1) analytical solutions, (2) laboratory experiments, (3) simulations, and (4) numerical solutions. Each of these can be exact or approximate. It seems clear that a large number of successful comparisons would tend to bolster confidence in the material.

A personal note of caution on making these comparisons· any comparison must be done carefully and the reasóns for differences correctly identified. Vague statements of "experimental error" or "approximations in the theory" are not reasons! The exact assumptions or experimental measurement inadequacies contributing to the difference must be identified. Our students must constantly place relative values on the technical material we give them. If we don't convincingly identify the correct source of differences in these comparisons, we fail to give them the information necessary to make these value judgments; in this way, we actually prevent them from developing confidence in fundamentals.

Symbols

A - area

G - forward transfer function

H - feedback transfer function

K - sensitivity factor

F - force

$\dot{m}$ - mass flow rate

M - Mach number

P - pressure

R - gas constant

s - Laplace variable (frequency domain)

t - time

V - volume

V - velocity

x - Cartesian coordinate

y - Cartesian coordinate

$\overline{z}$ - Cartesian coordinate

ρ - density

γ - ratio of specific heats

x - stroke of actuator

Subscripts and superscripts

f - final

s - storage tank

o - stagnation conditions

* - throat or sonic conditions

1 - initial condition

142

SECTION VI

ABSTRACTS

AERODYNAMIC CHARACTERISTICS OF AN
UNSTEADY SEPARATED FLOW[*]

M. S. Francis[**], J. E. Keesee[***], J. D. Lang[†], G. W. Sparks[††], G. E. Sisson[††]

Extended Abstract

During flight vehicle maneuvers at high angles of attack, dynamic stall or other
complex flow phenomena involving time-varying separation may occur resulting in aero-
dynamic loads which differ significantly from those predicted by steady flow consider-
ations. Future designs of advanced maneuverable flight vehicles may well seek to in-
corporate the advantageous effects of these highly energetic flows in a positive way
to enlarge the effective flight envelope. The capability to stabilize and control flow
behavior necessary for productive improvements in performance must be preceded by a more
complete knowledge of the mechanics of unsteady separation. The investigation discussed
in this paper is directed at a realistic modeling of these types of flows through an
improved understanding of the role of the dominant physical mechanisms.

An experiment which provided a simplified and controlled unsteady separation having
a two-dimensional flow geometry was devised using a NACA 0012 airfoil with an oscill-
ating fence-type spoiler located at mid-chord on one surface immersed in a subsonic wind
tunnel free stream. With the capability of adjustable spoiler mean height, oscillation
amplitude and frequency characteristics, this configuration provided for control of the
size of the separated region while fixing the separation point with respect to the free-
stream coordinate direction.

A characteristic feature of the resultant flow field observable for a wide range of
flow conditions was the generation and subsequent roll up of a large amount of vorticity.
While this variable represents a physically significant descriptor of regions of vis-
cous interaction in real fluids, it is a parameter whose experimental determination is
often difficult. In the experiments described below, the time-varying spatial vorticity
distribution associated with the separated region was inferred from both hot-wire ane-
mometer and two-color laser doppler velocimeter measurements using a spatial contour
integration technique (Ref 1). In this procedure, measurements of select instantaneous
velocity component values obtained over a mesh of spatial sampling locations were first

ensemble averaged (a phase-locked average correlated to spiler position) using a digital computer. The results were employed to calculate the circulation about elements of a planar array of spatial, rectangular contours like that shown in Figure 1. The resultant value of vorticity for any given phase point, spatially averaged over the "i"-th element of the mesh was then determined by the relationship

$$<\xi(t)>_i = \frac{1}{A_i} \oint_{C_i} \overline{U(\vec{x},t)} \cdot d\vec{l}(\vec{x})$$

where ξ is the vorticity component perpendicular to the plane of the integration array and A_i is the area of the mesh element. The conversion of data time histories to instantaneous spatial distributions allowed for a more useful description of results through the generation of iso-vorticity contour maps.

Resultant vorticity distributions were then compared with airfoil surface pressure measurements obtained from sixteen miniature transducers located in the wing's interior in an effort to generate a correlation for modeling purposes. A schematic of the complete experimental apparatus is provided in Figure 2.

Investigation of the global ensemble-averaged vorticity field generated by simple harmonic spoiler oscillations has revealed that the separation zone is not merely a growing and shrinking "bubble" as previously thought (Ref 2), but is a dynamically evolving vortex-like structure bearing a strong resemblance to the one encountered in the dynamic stall flow field (Ref 3) (Figure 3). Iso-vorticity contour maps of the resultant field in the outer shear layer region show how the concentrated vortex which forms on the spoiler upstroke begins to convect and diffuse as the spoiler retracts. An example of this behavior is depicted in Figure 4 for several phase points under identical flow conditions. While the peak vorticity levels are observed to be primarily a function of the freestream Reynolds number, the development of the flow geometry, including a characteristic lag in the separated region's growth is primarily dependent on the dimensionless frequency, k. The integral effect of the variation of circulation with time (phase angle) over the entire region is useful in discussing temporal lag effects.

The behavior of the corresponding surface pressure coefficient values (Figure 5) indicates that the growth characteristics of a suction peak (which appears in the region downstream of the spoiler on its upstroke) correlate closely with those of the outer shear layer at least for low values of frequency. The earlier development of the negative pressure peak at dimensionless frequencies near and above unity is attributed to an energetic flow reversal near the surface which precedes the development of the outer vortex in these cases.

A simplification made by correlating the 'center of vorticity' of the distribution with the surface loading is also discussed. A simple discrete vortex model is presented to describe the effects of vortex entrapment and subsequent convection on the pressure distribution.

References

1. Keesee, J. E., Francis, M. S., and Lang, J. D., "A Technique for Vorticity Measurement in Unsteady Flow," AIAA paper no. 78-801, presented at AIAA 10th Aerodynamic Testing Conference, April 19-21, 1978.

2. Lang, J. D. and Francis, M. S., "Dynamic Loading on an Airfoil Due to a Growing Separated Region," Prediction of Aerodynamic Loading, AGARD Conference Proceedings No. 204, September 1976, pp. 26-1 - 26-12.

3. McAlister, K. W., Carr, L. W., and McCroskey, W. J., "Dynamic Stall Experiments on the NACA 0012 Airfoil," NASA Technical Paper 1100, January 1978.
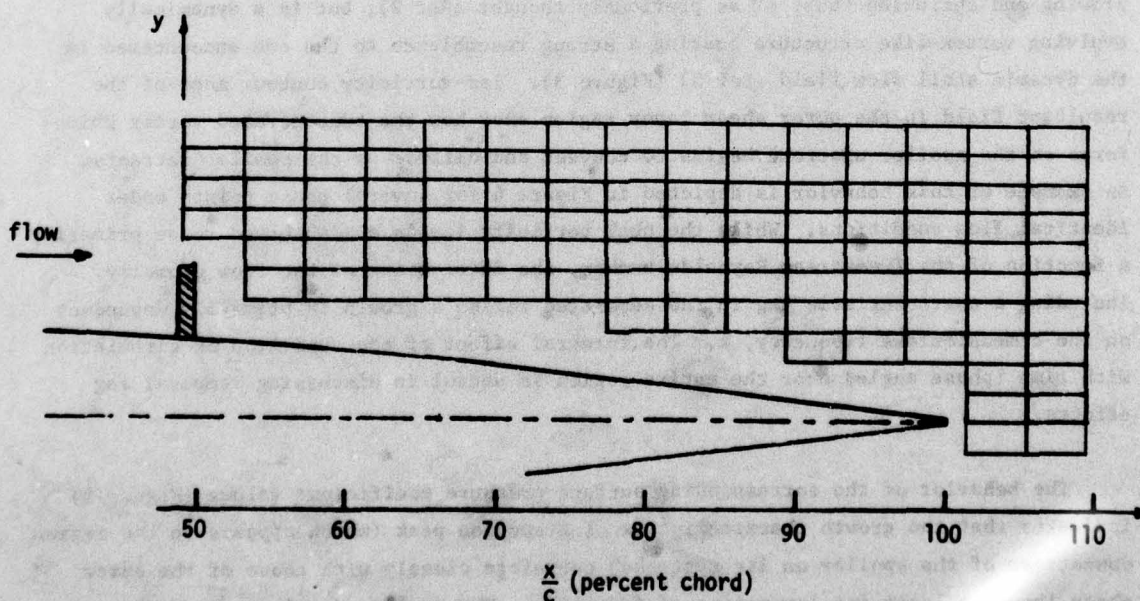
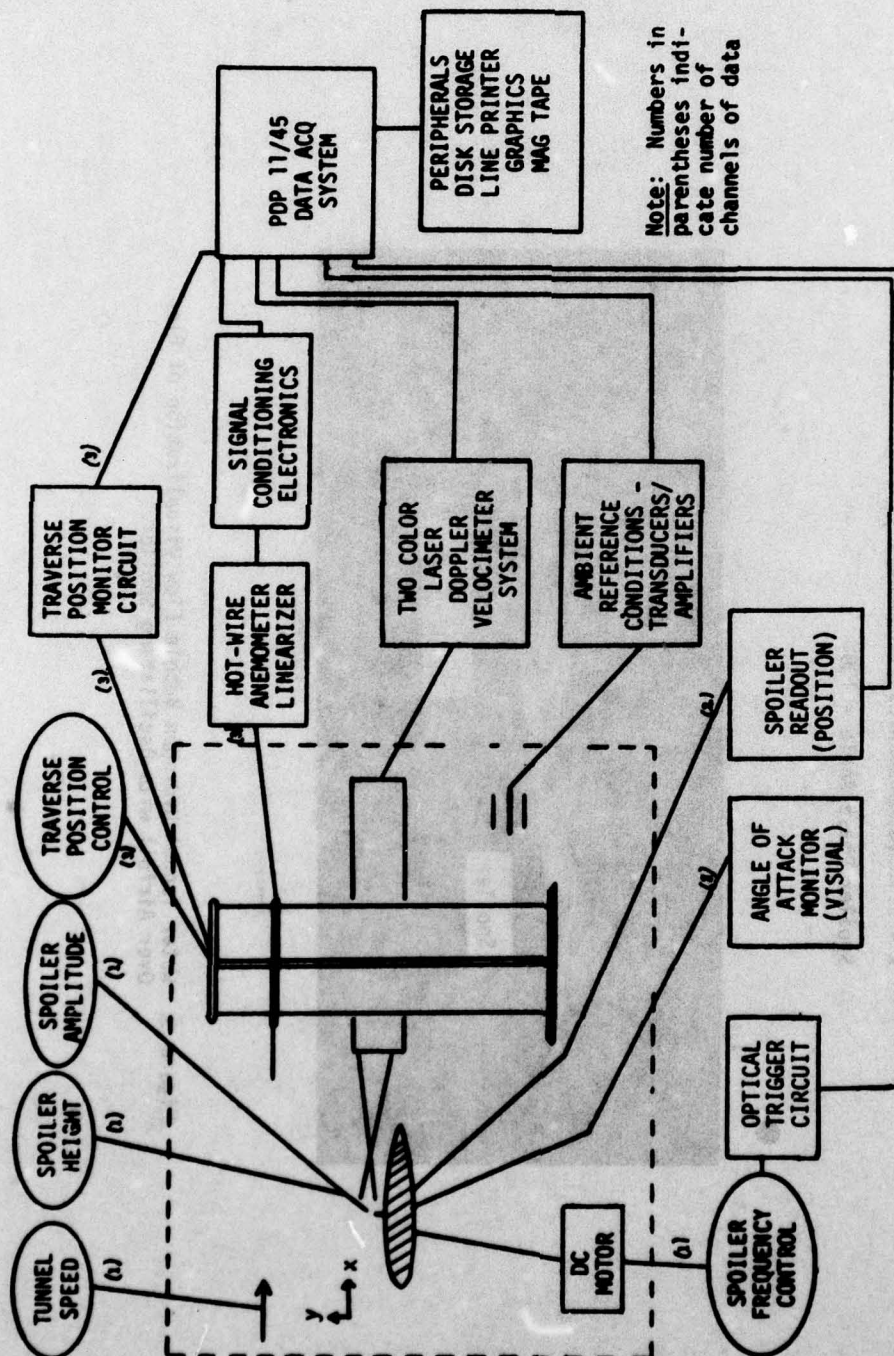Figure 1. Contour Array Geometry for the Outer Shear Layer

Figure 2. Schematic of Experimental Apparatus

Note: Numbers in parentheses indicate number of data channels of data

Low Reynolds Number (Re $\cong$ 10,000)

$k = 1.10$ (dimensionless frequency, $\frac{\omega c}{2U_\infty}$).
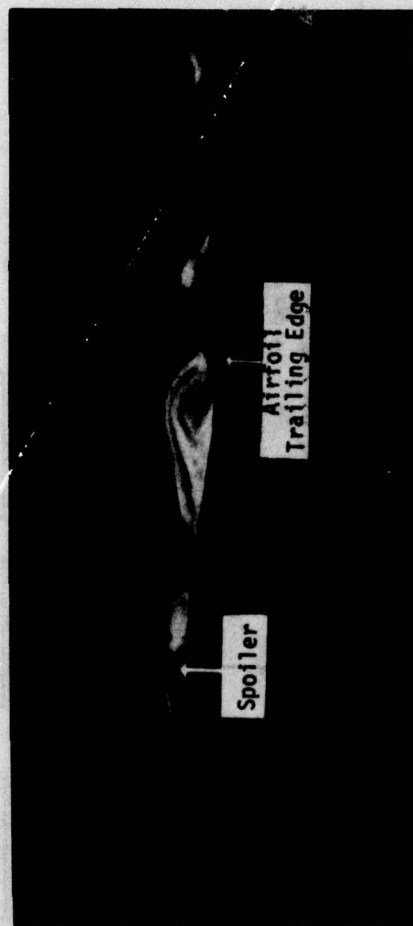
Spoiler Phase Angle = 136°

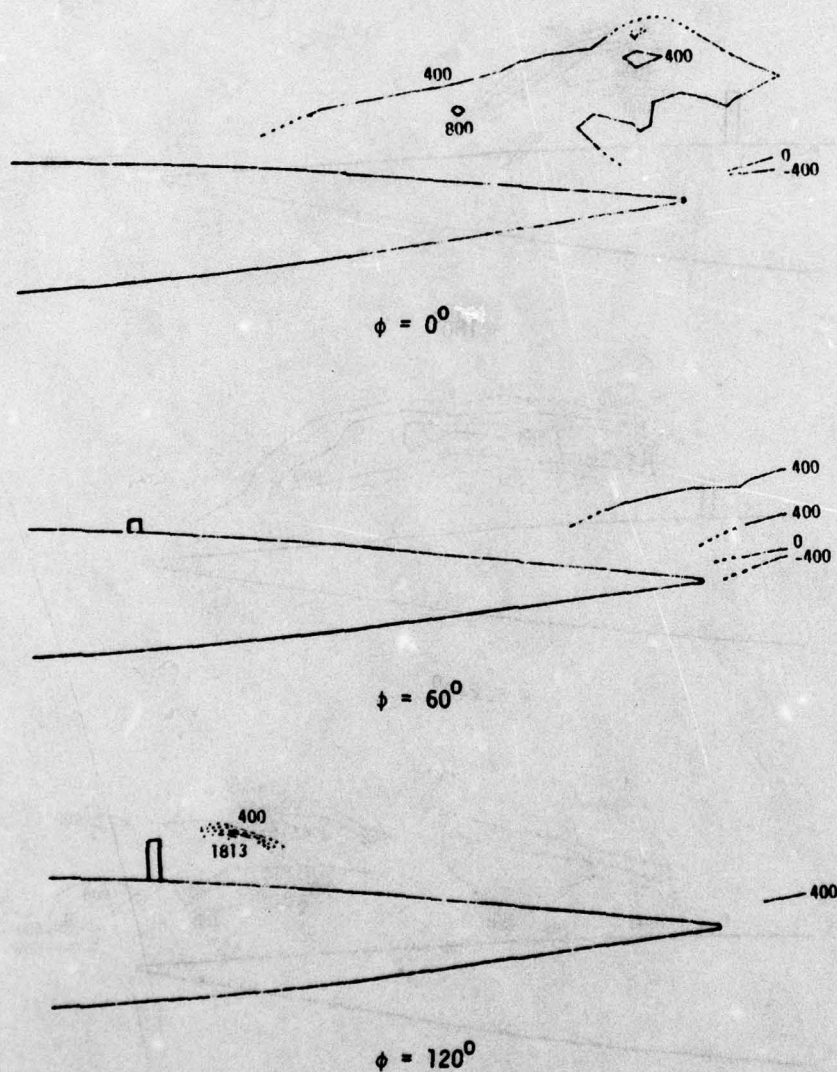Figure 3. Water Tunnel Hydrogen Bubble Flow Visualization of Flow Over Airfoil with Oscillating Spoiler.

Figure 4. Iso-Vorticity Contours in the Separated Region,
frequency = 19.85 Hz, U_∞ = 18.4 m/sec (distance
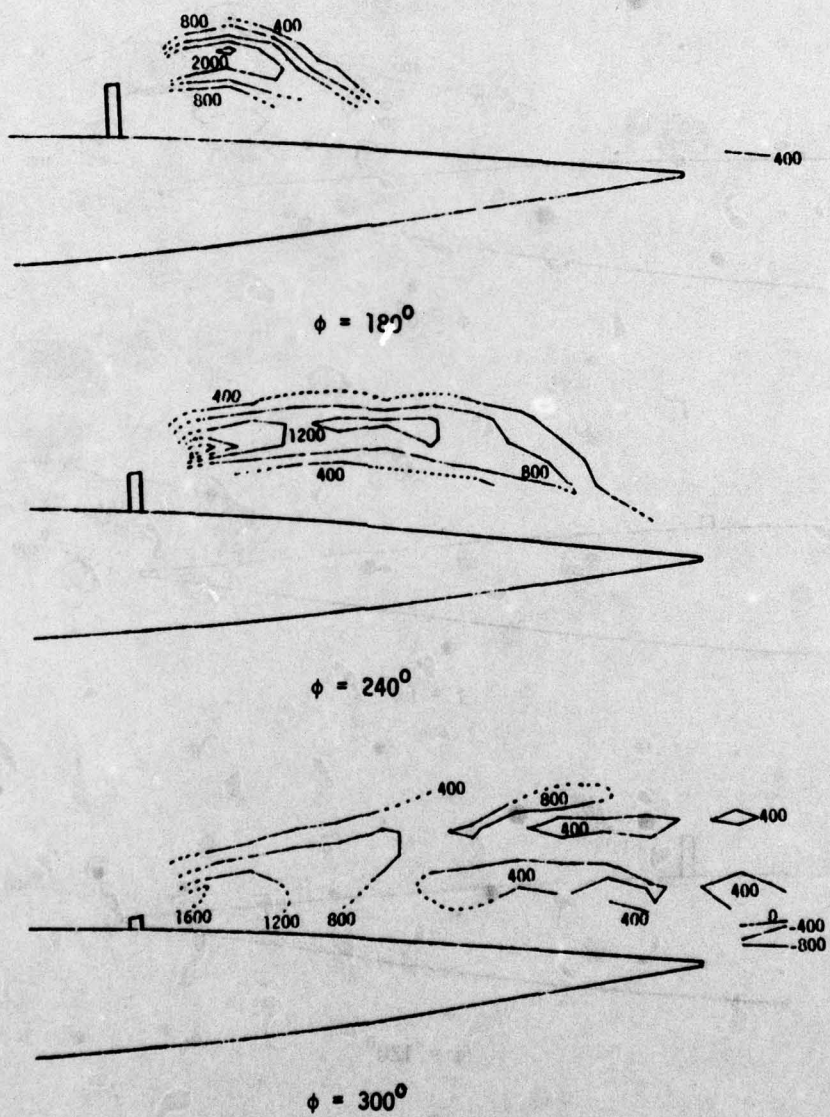between lines - 400 per sec, unless noted)

$\phi = 180^{\circ}$

$\phi = 240^{\circ}$

$\phi = 300^{\circ}$

Figure 4 (cont). Iso-Vorticity Contours in the Separated Region, frequency = 19.85 Hz, U_{∞} = 18.4 m/sec (distance between lines = 400 per sec, unless noted)

$\phi = 0^o$

$\phi = 60^o$

leading edge   percent chord
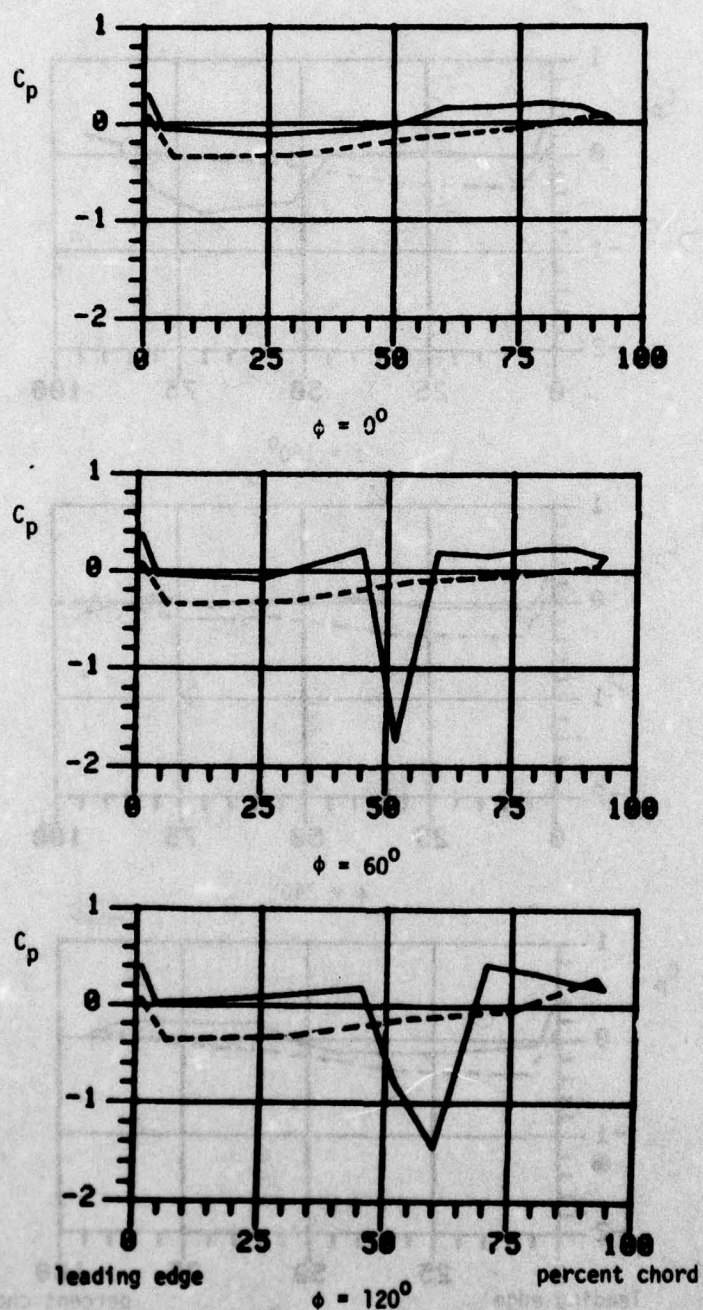
$\phi = 120^o$

Figure 5. Airfoil Pressure Coefficient Variation for Six Representative
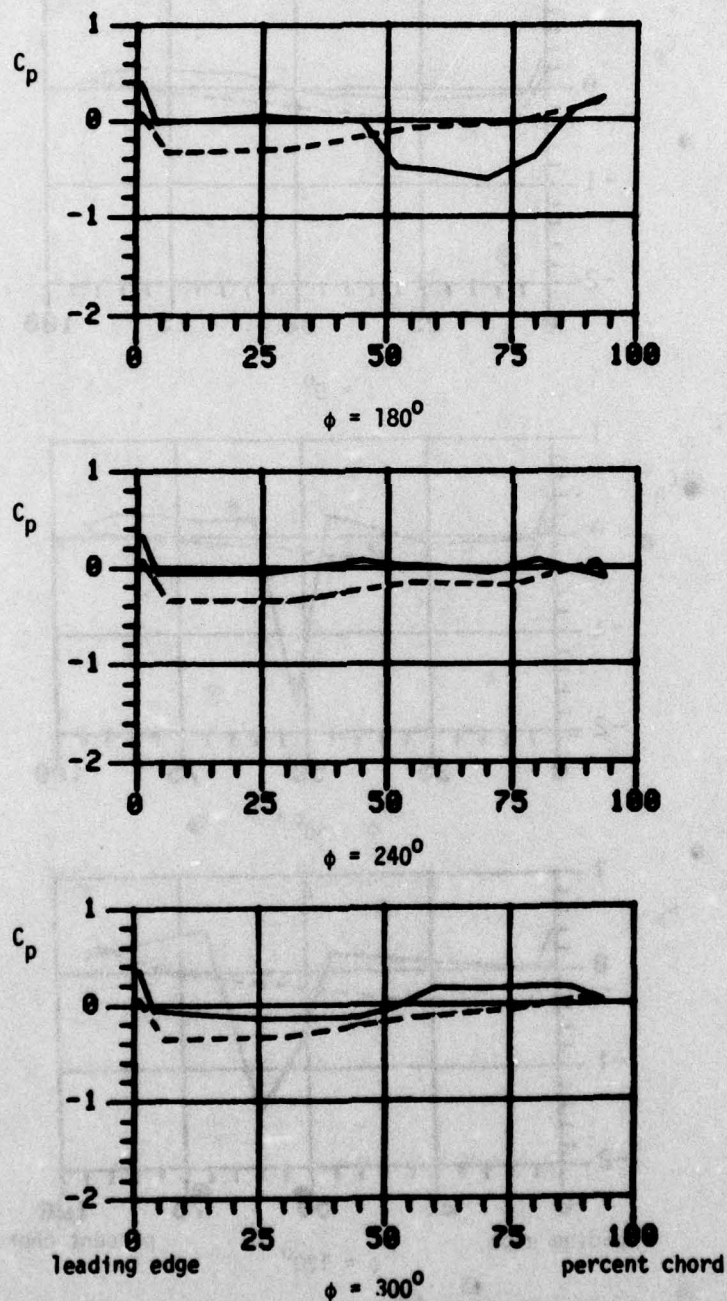Phase Points, frequency = 19.8 Hz, U_∞ = 18.4 m/sec

Figure 5 (cont). Airfoil Pressure Coefficient Variation for Six Representative Phase Points, frequency = 19.8 Hz, U_∞ = 18.4 m/sec